January 2015

An Investigation on the Band Gap and Band Edge of Semi-Conducting Lanthanum Transition Metal Perovskites for Photocatalytic Applications

Divya Suresh
University of South Florida, dibyyasuresh@gmail.com

An Investigation on the Band Gap and Band Edge of Semi-Conducting Lanthanum Transition Metal Perovskites for Photocatalytic Applications

by

Divya Suresh

A thesis submitted in partial fulfillment
of the requirements for the degree of
Master of Science in Materials Science and Engineering
Department of Chemical and Biomedical Engineering
College of Engineering
University of South Florida

Co-Major Professor: Venkat R. Bhethanabotla, Ph.D.
Co-Major Professor: John N. Kuhn, Ph.D.
Alberto A. Sagüés, Ph.D.

Date of Approval:
July 8, 2015

Keywords: Band Gap, Tauc Plot, Flat Band Potential, Mid Gap States, Photocatalyst Design

ACKNOWLEDGMENTS

I wish to express my deepest appreciation, thanks and indebted to my advisors Dr. Venkat R. Bhethanabotla and Dr. John N. Kuhn for their guidance, support, attention and continued encouragement.

I am thankful to Dr. Alberto A. Sagüés for his expertise, input and direction towards my band edge measurements that greatly assisted this research

My sincere thanks to Daniela Allbright for her contributions to the photodegradation study.

I take this opportunity to express my sense of gratitude to all of the department faculty, members and colleagues who directly and indirectly, have lent their support to this research.

TABLE OF CONTENTS

LIST OF TABLES

LIST OF FIGURES

ABSTRACT

For the past few decades, a frenzy of attention has been given towards the development of an assortment of photocatalysts as a solution for various environmental problems. TiO_2 is the most widely used photocatalyst. TiO_2 is biocompatible, chemically and thermally stable but TiO_2 and a vast majority other photocatalysts have large band gaps, and hence they find applicability only in the UV region of the solar spectrum. These large band gap photocatalysts suffer a severe limitation with regard to their overall process efficiency as the UV region contributes to about 3 to 4 % of the solar spectrum in terms of energy.

This thesis concentrates on the progress towards the generation of visible light active photocatalysts. Lanthanum transition metal perovskites were synthesized to incorporate B site doping in the following fashion; $LaCr_xFe_{1-x}O_3$, $LaMn_xFe_{1-x}O_3$ and $LaCr_xMn_{1-x}O_3$ (x= {1, 0.25, 0.5, 0.75}). These perovskites configurations were selected as $LaCrO_3$ has a conduction band edge suitable to activate most photocatalytic reactions, but $LaCrO_3$'s large band gap energetically hinders the photocatalysis. Doping $LaCrO_3$ with Fe and Mn allowed for tuning their band gaps and made various photocatalytic reactions feasible, namely CO_2 reduction and photoassisted dye degradation.

Validation of the perovskite's crystal structure was established through the study of their XRD patterns. The perovskite exhibited crystallinity throughout all doping concentrations. At some doping concentrations, due to low or high degree of tolerance factor, the presence of hexagonal and rhombohedral crystal phases was seen.

Analysis of the electronic structure of these perovskites was conducted through diffuse reflectance spectroscopy measurements and electrochemical impedance spectroscopy. Doping transition metals in B site of the perovskite led to the narrowing of band gap energy with the increase in the concentration of the higher atomic number transition metal. About 38% reduction in band gap was achieved in $LaCr_xFe_{1-x}O_3$. The band gap constituted of Mott- Hubbard gap and charge transfer gap.

For the species $LaCr_xFe_{1-x}O_3$, interband states exist with an energy gap as large as 1.3 eV for X=1 and 0.75. These states manifested as Urbach tails and are clearly documented in the absorption spectrum data. At x=0.5 and below, evidence of mixing is seen in $LaCr_xFe_{1-x}O_3$, leading to the diminution of these interband states, although not to full extent, their energy was reduced by about 0.5 eV. In $LaCr_xMn_{1-x}O_3$ and $LaMnxFe_{1-x}O_3$, the absence of Urbach tail and absorption edge is observed.

The band edge positions of most of these perovskites provided a large enough over potential to cause the reduction of CO_2. Future efforts on the photocatalytic activity study of these perovskites through dye degradation and CO_2 reduction are in progress. Preliminary results of photoassisted dye degradation are shared in this thesis.

CHAPTER 1 - INTRODUCTION AND BACKGROUND

1.1 Motivation

With the present environmental crisis, implementation of clean energy generation has become crucial. More and more resources are being allocated towards green energy harvesting and large-scale production of renewable fuels culminating in a fervent interest towards photocatalysts. Photocatalysis integrates solar energy with physical science thereby engendering panacea for our prevalent environmental problems.

Research and development efforts on a wide range of systems in the field of photocatalysis has seen a remarkable increase[1]. The multidisciplinary nature of this field has gained numerous industrial applications such as hydrogen production, reduction of carbon dioxide to hydrocarbon fuel systems [2, 3], water treatment[4, 5], air pollution diminution through removal of toxic sulphur and nitrogenous gases[6, 7]. This thesis is dedicated towards semiconductor type photocatalysts designed for CO_2 reduction through heterogeneous surface reactions.

The inclination towards semiconductor type photocatalyst is due their electronic structure that allows for light absorption. In this type of photocatalysis, the formation of the electron-hole pair is essential for the viability of the process. The generation of the electron-hole pair is achieved through the excitation of an electron from the valence band to the conduction band of the semiconductor. This excitation is made possible by the absorption of photons of appropriate energy.

Fujishima and Honda's[8] discovery of TiO_2's application in photocatalytic water splitting paved the path for rigorous investigations on TiO2- based systems. Other complex oxide systems also received unpretentious attention but failed to perform on par with TiO_2. The only drawback was the limited applicability of these photocatalysts in terms of their response to the solar spectrum.

The Sun bestows the Earth with 174,000 TW of energy [9]. However, 30% is partly reflected back by the Earth's stratosphere and the remaining absorbed by the hydrosphere and mountainous lithospheric terrains [9]. As a result, the solar spectrum on the Earth's surface consists of mainly visible region (λ= 400 to 700 nm), infra-red region (λ> 700nm) and small portion of UV region (λ<400 nm) [10]. In terms of energy, the visible region contributes to about 42-43 %, the infra-red region covers 52-55%, and the remaining comes from the UV region (refer to Fig 1.1) [11].

The above data suggests that the efficiency of semiconductor photocatalysis can be further improved by utilizing the visible region of the solar spectrum. Therefore tuning the band gap of certain semiconductor materials to enable the production of more efficient photocatalysts is the goal of our study.

1.2 Perovskites

Perovskites based semiconductor photocatalyst offer distinct physical and chemical advantages when compared to their counterparts. Perovskite metal oxides are commonly presented by ABO_3 nomenclature and have a distinct crystal structure. The A is larger cation while the B is the smaller one. Coordination of B cation with six oxygen atoms results in the formation of BO_6 octahedra. The A cation is coordinated to twelve oxygen atoms. The ABO_3 has a cubic crystal structure comprising of eight BO_6

octahedra connected to the corner while the A cation is located at the center. Tilting of the BO_6 octahedra can take place depending on the ionic radii and electronegativity difference between the A and B cations thus allowing the ABO_3 perovskite to exist in different crystal structures[12].

The ABO_3 perovskite can be modified to $AB_xB'_{1-x}O_3$ type by incorporating two different types of B cations. Depending on the charge and electronegativity of the participating B cations, the perovskite's inherit structure can be preserved through careful selection of B-type substituents. This permits the tunability of the perovskite's electrical and chemical properties, making these materials an ideal candidate for our study.

1.3 Mott Insulators and Charge Transfer Insulators

Transition metal oxides, like CoO, were thought of as metallic according to Electronic Band theory but when measured, exhibited insulator like behavior. The discovery of this deviation that manifested in certain transition metal oxides led to the birth of a new class of materials labeled as Mott insulators. De Boer and Verwey [13] studied the conductivity of 3d transition metal oxides; although conductivity of MnO, CoO, NiO, Fe_2O_3 was predicted to be metallic by band theory, data showed these metal oxides to possess conductivity in the range of 10^{-10} to 10^{-7} ($ohm^{-1}cm^{-1}$)[13, 14].

This complication was subsequently proved to arise because of the localized behavior of partially filled 3*d* orbitals. Arguments from Wilson and Peierls [15] for the nature 3*d* delocalization in Fe_3O_4 ($\rho=10^2$ $ohm^{-1}cm^{-1}$) led to the establishment that these 3d levels can behave either localized, partially localized or delocalized resulting in insulating or metallic behavior of the transition metal oxide, bringing into existence the

Hubbard model [16]. Hubbard postulated a Hamilton (1.1) that took into consideration the correlation energy between electrons, which band theory neglected. For transition metals that have strong correlating electrons, the degree of electron correlation energy governs the existence of their Mott insulator or metallic behavior. Following the Band theory of tight binding, with the decrease in the interatomic distance the bandwidth (B) increases as a consequence of better orbital overlap.

$$\mathrm{H} = t \sum_{<ij>_\sigma} (c_{j\sigma} + h.c) + U \sum_i n_{i\uparrow} n_{i\downarrow} \qquad 1.1$$

Then the level of electrical conductivity will depend on the kinetic energy *t* associated with the hopping of electrons from one atomic site to a neighboring site and the potential that arises due to Coulomb repulsion caused by duplex occupancy of opposite spin electrons in a single orbital. In other words, when an electron from one atomic site “hops” to the nearest occupied site, the two electrons in the single orbital will experience coulomb repulsive forces and the potential energy involved by this duplex occupancy is labelled as Hubbard energy U[16, 17]. For late transition metals, U is in the range of 7-10 eV[18]

According to the Hubbard Hamilton (1.1), in the absence of electron correlating forces U, the Hamilton describes Bloch states that make up the concept of electron band theory but with the company of U, the model contributed to the localization of electrons. Hubbard model effectuated the bifurcation of d-band into lower occupied and upper unoccupied Hubbard bands based on the degree of U and t. Thus the energy gap, Mott- Hubbard gap would be U-B and for small interatomic spacing, this gap will be governed by B leading to metallic behavior arising from the overlap of lower and upper

Hubbard bands and for large spacing, the ramifications of localized electrons result in insulating behavior.

Although the Hubbard model was unerring in predicting the electronic structure of late transition metal compounds, for compounds of Co, Ni and Cu, the electronegativity of the anion affected their energy gap, as in the case of insulating behavior of CoO and high electrical conductivity of CoS. This steered the postulation of another entity, the charge transfer energy Δ, which is the energy needed for the transfer of electrons to the upper unoccupied Hubbard band of transition metal from the valence band of the anion. Using the Anderson impurity Hamilton that incorporates both U and Δ, Zaanen. Sawatzky and Allen not only illustrated how the energy gap could be because of $d_i^n d_j^n \rightarrow d_i^{n+1} d_j^{n-1}$ fluctuation or charge transfer in nature based on the values of U and Δ but also the possibility of zero energy gap even when U was large [19].

The transition metal compound can be classified into a Mott insulator when Δ >U >B. In this case, the d-d electron transfer from the lower Hubbard band to the upper Hubbard band determines the energy gap.

When $\Delta < U$, the transition metal compound is classified as a charge transfer semiconductor. The overlap between the anion p band and the upper Hubbard band gives rise to a small energy gap even though U is considerably large. A metallic behavior is exhibited due to the overlapping of lower and upper Hubbard bands when U is lesser than B andΔ (refer to Fig 1.2)

1.4 Band Gap Tuning

Perovskites class of materials were chosen as they offered the opulence of doping with little or no change in crystallinity and crystal structure. Perovskite's thermal stability in the temperature range of our experiments also favored our inclination towards these materials.

The selection of $LaCrO_3$, $LaFeO_3$ and $LaMnO_3$ were based on their electronic structures. $LaCrO_3$ possesses a conduction band edge that favors photocatalysis of products we desire, but $LaCrO_3$'s large band gap of 3.08 eV poses energy restraints [55, 56]. In contrast, $LaFeO_3$ and $LaMnO_3$ have smaller band gaps but their band edge positions are not favorable for photocatalysis activation [55, 56].

The band structure of these perovskites depend on the transition metal present in their B site [55, 56], thus by doping with Fe or Mn using $LaCrO_3$ as templates an averaging of band gaps can occur. This band gap averaging was purely hypothetical, but the results from band gap and band edge measurements in chapter 2 offered substantial support to our hypothesis.

The primary focus of our investigation will be on obtaining beneficial band structures for photocatalysis, modification of the perovskite's surface and charge transport properties are developments that will materialize in our future work

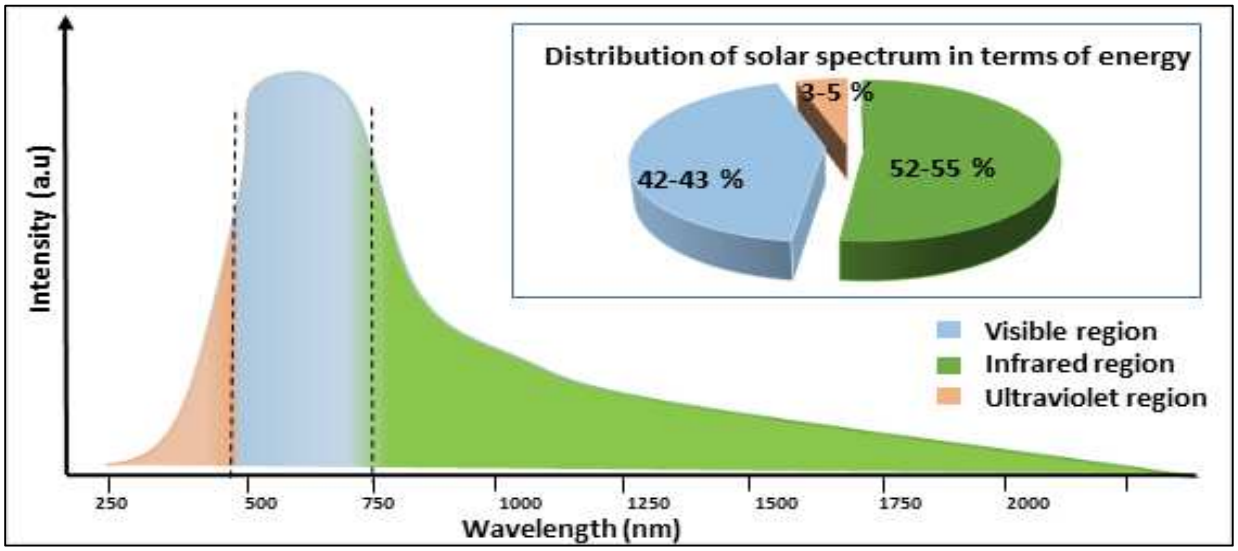

Figure 1.1 Distribution of solar spectrum (adapted from ASTM terrestrial reference spectra)

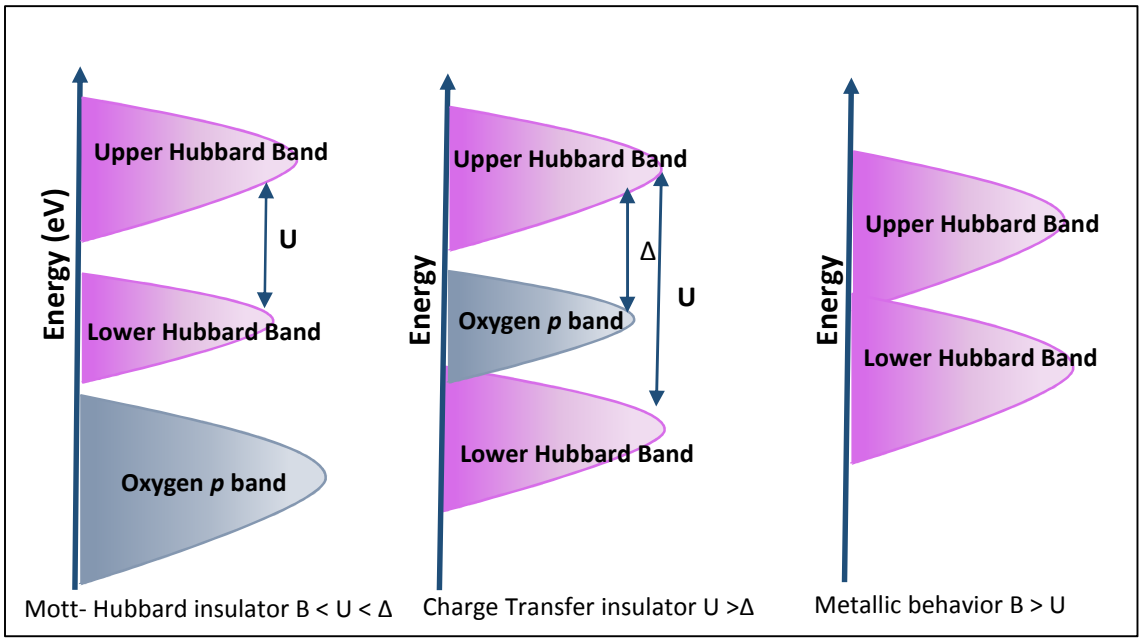

Figure 1.2 Classification of transition metal oxides (adapted from [20])

CHAPTER 2 - SYNTHESIS AND CHARACTERIZATION

2.1 Material Synthesis

The design of semiconducting $AB_xB'_{1-x}O_3$ perovskites for our investigation was based on the strategy of synergistic effects of B-site transition metals that determined its photocatalytic activity. $LaFe_xCr_{1-x}O_3$, $LaFe_xMn_{1-x}O_3$ and $LaMn_xCr_{1-x}O_3$ (x= {1, 0.25, 0.5, 0.75}) perovskites were synthesized under identical conditions through Pechini process[21].

Many methods have been researched for the synthesis of $AB_xB'_{1-x}O_3$ perovskites i.e microwave method, hydrothermal, solvothermal, pyrolysis [22-26]etc but this gel polyesterification method has been widely used in the synthesis of a variety of metal oxides as it offers several advantages such as precise and direct control over the stoichiometry of the product, achieve uniform distribution at a molecular scale, homogeneity and operation at ambient pressure[21]

The synthesis began with dissolving hydrous nitrates in an aqueous citric acid (Sigma-Aldrich, anhydrous, ≥99.5%) solution in the presence of a polyhydroxy alcohol. The citric acid acts as a chelating agent. Lanthanum–transition metal citrates were prepared by adding an aqueous solution of citric acid (CA) to a suspension of transition metal nitrate in $La(NO_3)_3$ aqueous solution.

The La-Transition Metal (M)-CA solution with La:M:CA =1:1:10 was continuously stirred with a magnetic stirrer on a hot plate to remove excess of water and to

accomplish the polyesterification reaction. The La-M-CA solution was heated up to ~60°C for 2 h after which Ethylene Glycol (EG) was added (CA: EG=1:4).

The perovskites were synthesized using laboratory grade reagents and distilled deionized water. $Fe(NO_3)_3.9H_2O$ (purity≥ 98%) procured from Sigma-Aldrich was used as a precursor for Fe. $La(NO_3)_3.XH_2O$(Sigma-Aldrich, 99% trace metals basis) as a La precursor. $Cr(NO_3)_3.9H_2O$ as Cr precursor and $Mn(CO_3)$ (Alfa Aesar, 99.9% (metals basis excluding Na)) as Mn precursor.

The solution temperature was raised to 90°C and maintained at this temperature under constant stirring for 7 h. A gummy gel-like mass was obtained as the end product. The thermal decomposition of the La–M precursors was achieved at 450°C for 2 h in air. The solid residue attained after thermal decomposition was calcined at 950°C for 6 h in air, then cooled down to room temperature.

2.2 Powder X-Ray Diffraction

The X-ray diffraction (XRD) patterns for the prepared perovskite powders were obtained with the aid of a Bruker X-Ray Diffractometer with CuKα radiation (λ = 0.154 nm). The scan range of 2θ was from 20° to 100° with a step size of 0.0102°. The experiment was conducted at normal room temperature and pressure.

The XRD profiles of the perovskites (refer to Fig 2.2-2.7) were similar and displayed diffraction peaks that complemented the standard diffraction patterns found in JCPDS for $LaFeO_3$, $LaCrO_3$ and $LaMnO_3$ perovskites.

The diffraction spectra exhibited an assortment of cubic, orthorhombic, rhombohedral and hexagonal crystals lattices with cubic being the major component. The diffraction peaks were refined and indexed. The diffraction lines related to the cubic

crystalline phase were (1 0 0), (1 1 0), (1 1 1), (2 0 0), (2 1 0), (2 1 1), (2 2 0), (3 0 0), (3 1 0), (2 2 2) and (3 2 1). The intensity and sharpness of the peaks indicated a good degree of crystallinity. The spectra did not confirm the presence of iron, chromium and manganese oxides or other impurities, thus crediting the phase purity of the prepared $LaM^1_xM^2_{1-x}O_3$ perovskites.. The lattice constant (a) for the cubic crystal phase was calculated through Bragg's Law.

$$n\lambda = 2d \sin\theta \tag{2.1}$$

where λ was the wavelength of radiation used, *n* = 1, d is the interplanar distance and θ is the scattering angle. The crystallite size was estimated through Scherrer analysis on peak (1 1 0), assuming instrumental peak broadening to be zero. The effect of B-site doping was evident from the shift of the highest intensity peak (1 1 0) (refer to Fig 2.3, 2.5 and 2.7).

For the case of $LaMn_xFe_{1-x}O_3$, with increasing Fe, the lattice constant a increases. This was because of substitution of a smaller ion ($r_{Mn^{+3}}$ = 72 pm) with a considerably larger ion ($r_{Fe^{+3}}$ = 78.5 pm). Table 2.2 shows that lattice constant (a) is highest for $LaFeO_3$ and decreases with the increase in the molar concentration of Mn.

The similar effect was visible for $LaCr_xMn_{1-x}O_3$ and $LaCr_xFe_{1-x}O_3$, as seen from the peak shift in their XRD patterns, the lattice constant *a* (refer to Fig 2.2, 2.6 and Table 2.1 and 2.3). The decrease in lattice constant *(a)* for $LaCr_xMn_{1-x}O_3$ is evident with the decrease in Cr^{+3} ion (r_{Cr+3} = 75.5 pm).

The Goldschmidt's tolerance factor *t* [27], defined by equation 2.2 was estimated for each of the perovskite species. For an ABO_3 perovskite, the tolerance factor was validated under the assumption the bonds are purely ionic.

$$t = \frac{(r_A + r_O)}{\sqrt[2]{2}(r_B + r_O)} \quad (2.2)$$

where r_A, r_B and r_O are the ionic radii of the A site, B site and oxygen ions respectively. For 0.89< t <1, the cubic crystal structure of the perovskite is stable. The orthorhombic crystal structure was more favorable when t <0.89 as the BO_6 octahedra tilts with the decrease in the symmetry of the lattice. Hexagonal crystal structure is also noticed in some of these perovskites.

The lower tolerance factor of $LaCrO_3$ and $LaFeO_3$ manifests in the stabilization of orthorhombic crystal structure that was apparent from the XRD patterns of the respective perovskites. The calculated tolerance factor for each of the synthesized perovskites is listed in Table 2.1- 2.3. The Lattice size was calculated for the cubic crystal structure species. As the peak shifts in the XRD patterns of the synthesized perovskites are symmetrical absence of stress and strain can be confirmed.

Table 2.1 Crystallite size and lattice constant of $LaCr_xMn_{1-x}O_3$ perovskites

Perovskite	**Crystallite size[a] (Å)**	**Lattice Constant[b] a (Å)**	**Tolerance factor**
$LaCrO_3$¤	446.7	3.894	0.897
$LaCr_{0.9}Mn_{0.1}O_3$	396.0	3.892	0.899
$LaCr_{0.75}Mn_{0.25}O_3$¤	309.3	3.903	0.901
$LaCr_{0.5}Mn_{0.5}O_3$¤	202.7	3.893	0.905
$LaCr_{0.25}Mn_{0.75}O_3$¤	210.5	3.889	0.909
$LaCr_{0.1}Mn_{0.9}O_3$	199.5	3.872	0.911
$LaMnO_3$	194.5	3.89	0.912

a: crystal size calculated by Scherrer analysis of peak (1 1 0), b: Lattice constant calculated for cubic phase, ¤: mixed crystal structures present

Table 2.2 Crystallite size and lattice constant of $LaMn_xFe_{1-x}O_3$ perovskites

Perovskite	Crystallite size[a] (Å)	Lattice Constant[b] a (Å)	Tolerance factor
$LaFeO_3$¤	324.1	3.92	0.883
$LaMn_{0.25}Fe_{0.75}O_3$	301.8	3.934	0.890
$LaMn_{0.5}Fe_{0.5}O_3$	239.1	3.923	0.897
$LaMn_{0.75}Fe_{0.25}O_3$¤	206.0	3.903	0.904
$LaMnO_3$	194.5	3.89	0.912

a: crystal size calculated by Scherrer analysis of peak (1 1 0), b: Lattice constant calculated for cubic phase, ¤: mixed crystal structures present

Table 2.3 Crystallite size and lattice constant of $LaCr_xFe_{1-x}O_3$ perovskites

Perovskite	Crystallite size[a] (Å)	Lattice Constant[b] a (Å)	Tolerance factor
$LaCrO_3$¤	446.7	3.894	0.897
$LaCr_{0.75}Fe_{0.25}O_3$	299.3	3.862	0.904
$LaCr_{0.5}Fe_{0.5}O_3$¤	391.9	3.911	0.912
$LaCr_{0.25}Fe_{0.75}O_3$¤	443.4	3.812	0.919
$LaFeO_3$¤	324.1	3.92	0.883

a: crystal size calculated by Scherrer analysis of peak (1 1 0), b: Lattice constant calculated for cubic phase, ¤: mixed crystal structures present

2.3 Diffuse Reflectance Spectroscopy

2.3.1 Introduction and Background Information

Condition for feasible photocatalytic reactions, necessitated the photocatalyst to generate electron-hole pairs through the absorption of photons from the incident radiation under the stipulation that the wavelength of the photons are less than the band gap wavelength of the photocatalyst. A large absorption coefficient will enable a positive environment for the photons to be absorbed on the surface of the photocatalyst

consequently reducing the diffusion length of the charge carriers thus delivering a more favorable outcome[28]. Appreciable output can be achieved when band gap energies are lesser than 2.7 eV as the photocatalyst can absorb a wider portion of the solar spectrum i.e. visible region. Reiterating, TiO_2, which seems to be an epitome with respect to a photocatalysis' process efficiency but due to its large band gap of 3.2 eV, it falls short in terms of a photocatalysis' efficiency for energy conversion.

Diffuse reflectance spectroscopy is a common approach employed to measure the band gap energy[29]. Obstruction created by a solid medium in the path of a light beam leads to dissemination of light throughout the depth of the medium and depending on the optical property of the material, a portion of light maybe be absorbed, transmitted and or reflected.

The reflected portion propagating in a path different from the one traced by the incident beam constitutes the diffuse reflectance spectrum of the material. The band gap energy value of a semiconductor can be extracted from its diffuse reflectance spectrum through Tauc plots[30, 31]. This method also allows for the approximate estimation of the absorption coefficient from the diffuse reflectance data.

Electronic transitions between the highest occupied valence band and the lowest unoccupied conduction band start at the absorption edge of the absorption spectrum. The energy differences between the said bands is given by the band gap energy. For large absorption values, an *n* order dependence of band gap energy with the materials absorption coefficient is observed, and their relationship is established through Tauc equation

$$\alpha h\nu = A(h\nu - E_g)^n \tag{2.3}$$

where α, v, A, and E_g are the absorption coefficient, incident light frequency, proportionality constant and band gap, respectively and n decides the characteristics of electron transition in a semiconductor, i.e. n = 1/2 for direct transition and n = 2 for indirect band transition[32, 33]. Here the perovskites display direct band transition. It should be noted that the Tauc equation holds physical meaning only for energies equal to or higher than the band gap energy.

For photons of energy less than the band gap energy, the absorption coefficient depends exponentially on the photon energy.

$$\alpha(h\nu) \sim e^{\left(\frac{h\nu}{E_u}\right)} \tag{2.4}$$

where E_u is the Urbach energy. E_u is the width of the band tails of localized states and related to the transitions from these localized states to extended states in the conduction band.. This exponential decay of localized states into the band gap is caused by deviations from ideal stoichiometry[34], structural[35] and thermal[36] induced disorders. The genesis of these localized tail states is spawned by different possibilities.

The emergence of these localized states maybe because of exciton-phonon coupling promoting the widening of the exciton line[37, 38]. The micro-electric fields due to phonon interaction can establish energy states in the band gap[39]. The reciprocal of the slope of linear low energy region of ln(α) vs. $h\nu$ curve gives the value of E_u. Errors in band gap energy calculations were minimized by obtaining the maxima- minima profiles of the Tauc curve to better judge the positions of electronic transitions.

The DRS can be mathematically expressed in terms of absorption coefficient through differential equations obtained from Kubelka-Munk theory[40, 41]. Under the constraints of this theory, for a homogenous distributed sheet of powder of significant thickness (1-3 mm) and particle size sufficiently greater than the wavelength of the incident radiation, the diffused reflectance (R_∞) of the powder sample is related to effective absorption coefficient k^* and scattering coefficient S of the powder. The effective absorption coefficient is proportional to the true absorption coefficient α of the powder.

$$F(R\infty) \equiv \frac{(1-R\infty)^2}{2R\infty} = \frac{\boldsymbol{k}^*}{s} \tag{2.5}$$

Substituting the Kubelka- Munk function ($F(R\infty)$) in the Tauc equation, the intercept of linear region of $F(R\infty) = A(h\nu - E_g)^n$ curve on the *x*-axis gives the value of the band gap energy of the sample.

2.3.2 Experiment Setup

The diffused reflectance spectrum (DRS) of the samples was measured using a Jasco V-670 UV-Vis-NIR spectrophotometer with a scan speed of 100 nm min^{-1} in a wavelength range of 360 nm to 800 nm for $LaCr_XFe_{1-X}O_3$ and 360 nm to 1800 nm for $LaCr_XMn_{1-X}O_3$/ $LaMn_XFe_{1-X}O_3$. The absorbance spectrum was measured from 360 nm to 800 nm for $LaCr_xFe_{1-x}O_3$ and $LaMn_xFe_{1-x}O_3$ specimens with a scan speed of 100 nm min^{-1}. All experiments were performed at room temperature and atmospheric pressure. The perovskite powders were fine ground using a mortar and pestle. The powders were tightly packed to prevent any voids and sandwiched between two microscopic glass slides. The thickness of this sample setup was 2 mm. Spectralon SRM-99 purchased

from Labsphere was used as reference standard for reflectance and absorbance measurements. The absorbance and reflectance spectra of the glass slides were analyzed to avoid experimental errors. The absorbance of glass slide remained almost constant (0.03 approx) within the range of the experiment and was removed from the absorbance measurement of perovskites through base line subtraction.

2.4 Mott Schottky Measurements

2.4.1 Introduction and Background Information

In order to better classify the prepared perovskites as a potentially potent photocatalyst for specific applications i.e., photodegradation of organic dyes/pollutant, photocatalytic water splitting, photocatalytic carbon dioxide reduction and so on; a knowledge of their band energy levels is essential. The band energy levels of the synthesized perovskites were investigated through the determination of their flat band potential (V_{fb}) by Mott-Schottky (M.S) plot.

Before evaluating the V_{fb} through M.S plot, it is crucial to understand the correlation between the energy levels of a semiconductor (S) and an electrolyte (E) in contact. At the semiconductor-electrolyte interface (SE), the equilibrium between these phases is established by equalizing their electrochemical potentials. The Fermi level of the semiconductor and the redox potential of the electrolyte determine their respective electrochemical potential. Fig 2.22 (a) represents the energy levels of a p-type semiconductor and a redox couple in an electrolyte.

The conduction and valence band edges are identified as CB and VB respectively. Both CB and VB are dependent on the semiconductor potential. In this case, as the Fermi level (E_f) is below the redox potential, to attain electrochemical

equilibrium between the two phases in contact, electrons must transfer from the electrolyte solution into the semiconductor. Any excess charge does not lie on the surface of the semiconductor but extends into the bulk up to a distance of 100-10,000 Å [42]. This region is called the space charge region.

In the above case, due to the charge transfer of electrons into the bulk of the semiconductor, a negative space charge region is created causing a downward bending of the band edges (refer Fig 2.22 (b)). The space charge region is counterbalanced by a sheet of positive charge from the electrolyte solution (Helmholtz layer). For an n- type semiconductor in contact with an electrolyte solution, as shown in Fig 2.23 (a), the Fermi level of the semiconductor is above the redox potential of the electrolyte. A transfer of electrons from the semiconductor to electrolyte occurs to establish electrochemical equilibrium thus causing the formation of a positive space charge region leading to the upward bending of the band edges (refer to Fig 2.23 (b)).

Separation between the redox and Fermi levels of the semiconductor and electrolyte respectively will vary by applying a potential using an external source like a potentiostat and hence the level of band bending will depend on this applied potential. At a certain potential, the level of band bending is negligible and this potential is called the flat band potential.

The potential difference over the SE interface (∂_{SE}) (refer to Fig 2.23 (c)) arises from the contribution of the space charge region (SC) and the Helmholtz layer (H)[43].

$$\partial_{SE} = \partial_{SC} + \partial_{H} \tag{2.5}$$

The interfacial capacitance $c_{sc} = \frac{dQ_{SC}}{d\partial_{sc}}$ deduced from the solution of the following Poisson's equation of charge density function $\sigma(x)$ [43].

$$\frac{d^2\partial(x)}{dx^2} = -\frac{\sigma(x)}{\varepsilon\varepsilon_o} \tag{2.6}$$

where $\sigma(x)$ a function of the donor density (N_d) is, ε is the dielectric constant, ε_o permittivity of free space, Q_{SC} is total space charge per unit surface area of SE. Given that all potential changes occur over the interfacial region, then $\partial_{SC} = V - V_f$

$$\frac{1}{C_{sc}{}^2} = \frac{2}{e\varepsilon\varepsilon_o N_d A}\left(V - V_{fb} - \frac{k\,T}{e}\right) \tag{2.7}$$

where *e is* the charge of an electron, *V* is applied potential, and A is the surface area. The capacitance of the space charge region (C_{sc}) and V_{fb} for an n-type semiconductor are related through the Mott- Schottky equation. V_{fb} can be obtained by extrapolation of ${}^1/_{C_{SC}{}^2}$ = 0 [1]. The slope of the M.S plot yields the donor density.

The band edges were calculated from the V_{fb} and the band gap (E_g) obtained from DRS analysis. The conduction band edge (E_{CB}) of an n-type semiconductor is almost equal to V_{fb} and the valence band edge (E_{VB}) for a p-type semiconductor is approximated to be equal to its V_{fb} [44]. The E_{VB} and E_{CB} of n-type and p-type semiconductors respectively can be estimated from their E_g.

2.4.2 Validity of Mott Schottky (M.S) Capacitance Behavior

The interfacial capacitance derivation is based on the following assumptions [45]. The bulk semiconductor offers zero resistivity, and capacitances of the Helmholtz layer,

[1] $\frac{k\,T}{e}$ is negligible (approx. 0.025)

electrode/ electrolyte, and electrode/semiconductor are negligible. Surface states are absent. The dielectric coefficient ε is independent of the test frequency. Donor species are restricted to only a single type. The interface has two-dimensional planar characteristics and has homogeneous defects distributed in a spatial fashion.

2.4.3 Sample Preparation

The semiconducting perovskites powders were fashioned into thin films that strongly adhered to pure titanium metal foils of thickness 0.25 mm. These films were made by mixing 0.12 g of the powder with appropriate amount of deionized water needed to form a slurry that was smeared evenly on Titanium foils.

Adherence between the powders and the metal foil was obtained by sintering the prepared films for 6 h at 600°C. To hold the electrolyte solution in contact with perovskite films, an inert polyethylene tube with internal area 0.636 cm^2 and volume of 0.9 ml was fashioned on top of the prepared films using epoxy.

The electrolyte solution used for the M.S experiment was 0.1 M Na_2SO_4. The electrolyte was prepared from laboratory grade reagent and distilled deionized water. Two test samples of each perovskite powder were made and named as $LaM_xM'_{1-x}O_3$ sample I and $LaM_xM'_{1-x}O_3$ sample II. It is assumed that there is a good electronic contact between the perovskite powder and the titanium foil, and that the electrolyte does not come in direct contact with the titanium foil. This assumption needs to be studied in future work by comparing V_{fb} measurements of perovskites on Ti foil vs. the measurements of V_{fb} obtained by perovskites film on platinum foil.

2.4.4 Experiment Setup

The electrochemical setup consisted of a three-electrode configuration: the reference (R), the counter/ counter sense (C/CS) and the working/ working sense (W/WS) electrode (refer to Fig 2.24). The control of potential and measurement of current takes place at the working electrode. Here the working electrode is the perovskite film coated on Ti foil. The reference electrode measured the potential of the working.

The reference electrode used here was activated Ti wire. The counter electrode completes the cell circuit. The current that enters electrolyte through the working electrode leaves the cell through the counter electrode. Chemically inert metals were used as counter electrodes. Here we used activated Ti wire as the counter electrode. The working sense was connected to the working sample, thus introducing two independent systems: the W and C/CS and WS and R. The current flows through the working and counter electrodes and the potential was measured through the working sense and reference electrode path.

All voltages recorded were calibrated against saturated standard calomel electrode (refer to Fig A.2 and appendix A.2). For the M.S measurements, the samples were tested after carefully rinsing with deionized water and then with the electrolyte. The samples along with the contacts were allowed to sit for a period of half hour in the 0.1 M Na_2SO_4 electrolytic solution before the measurements were started.

A hold period of 7 minutes in between each test has followed to achieve more accurate results. The experiments were carried out in the dark using Gamry Potentiostat Reference 600 (Gamry Instruments, Warminster, PA, USA). The numerical fitting

program Gamry Echem Analyst (Gamry Instruments, Warminster, PA, USA) was used for the estimation of electrochemical parameters. The V_{fb} measurements were performed at frequencies of 100 Hz and 50 Hz from -1.5 V to -0 V with a step size of 10 mV. Test frequency of 10 and 1000 Hz were also employed to test the sensitivity of the sample

Table 2.4 (a) Flat band potential and donor density of $LaCr_xMn_{1-x}O_3$

Perovskite	Flat Band Potential V vs NHE		ε Nd ($x10^{20}$ cm^{-3})			
	50 Hz	100 Hz	50 Hz		100 Hz	
			region 1	region 2	region 1	region 2
$LaCrO_3$	-0.892±0.00	-0.883±0.01	0.8	1.8	0.88	1.79
$LaCr_{0.75}Mn_{0.25}O_3$	-0.942±0.06	-0.944±0.06	0.64	1.62	0.61	1.56
$LaCr_{0.5}Mn_{0.5}O_3$	-0.899±0.06	-0.929±0.07	0.71	1.42	0.7	1.38
$LaCr_{0.25}Mn_{0.75}O_3$	-0.779±0.03	-0.757±0.04	0.99	1.58	0.86	1.47
$LaMnO_3$	-0.547±0.01	-0.687±0.14	2.77	5.54	3.57	5.97

Table 2.4 (b) Flat band potential and donor density of $LaCr_xFe_{1-x}O_3$

Perovskite	Flat Band Potential V vs NHE		ε Nd ($x10^{20}$ cm^{-3})			
	50 Hz	100 Hz	50 Hz		100 Hz	
			region 1	region 2	region 1	region 2
$LaCrO_3$	-0.892±0.00	-0.883±0.01	0.8	1.8	0.88	1.79
$LaCr_{0.75}Fe_{0.25}O_3$	-0.855±0.01	-0.867±0.00	0.07	0.16	0.06	0.14
$LaCr_{0.5}Fe_{0.5}O_3$	-0.537	-0.604	1.73	-	1.02	-
$LaFeO_3$	-0.384±0.01	-0.393±0.00	2.38	3.92	2.06	3.69

Table 2.4 (c) Flat band potential and donor density of $LaMn_xFe_{1-x}O_3$

Perovskite	Flat Band Potential V vs NHE		ε Nd ($x10^{20}$ cm^{-3})			
	50 Hz	100 Hz	50 Hz		100 Hz	
			region 1	region 2	region 1	region 2
$LaMnO_3$	-0.547±0.01	-0.687±0.14	2.77	5.54	3.57	5.97
$LaMn_{0.75}Fe_{0.25}O_3$	-0.836±0.02	-0.901±0.00	2.06	6.13	2.53	6
$LaMn_{0.5}Fe_{0.5}O_3$	-0.945±0.00	-1.02±0.03	0.2	0.3	0.25	0.39
$LaMn_{0.25}Fe_{0.75}O_3$	-0.619	-0.622	1.85	3.67	1.22	2.82
$LaFeO_3$	-0.384±0.01	-0.393±0.00	2.38	3.92	2.06	3.69

2.5 Energy Level Predictions Based on Electronegativity Values

The concept of "*electronegativity*" was first introduced by Berzelius, who developed a scale based on his electronegativity values to explain enthalpies of reaction[46]. Berzelius electronegativity values were based on bulk properties of the element and led to the confliction of his theory with the laws of electrostatics[47]. Subsequently, Pauling's thermochemical investigation resulted in the famous Pauling's electronegativity scale that was a development of Berzelius theory on an atomic level[48]. Pauling's electronegativity was defined as an atom's ability to attract electrons. His calculations were based on the difference between hetero and homoatomic bond enthalpies of two different elemental species[48, 49]. Although his theory established significant improvements in the field, the Pauling's scale had its limitations as it assigned a single value to the same element irrespective of its bonding nature (i.e hybridization) with respect to different electronic arrangements[50].

Mulliken's electronegativity scale proved to be a more precise form electronegativity representation. Mulliken's electronegativity for univalent species is given by the arithmetic mean of its first ionization (ε_{IP}) and electron affinity (ε_{EA}) energies[51]. Later density function calculations[52] based on the valence state of the atom gave precision to the concept of electronegativity and helps validate Mulliken's electronegativity theory.

Closed shell Hartee-Fock theory based Koopman's theorem allowed for the estimation of the energy of the highest occupied molecular orbital energy (εHOMO) of a compound. This theorem affirms that εHOMO equals -ε_{IP} of the compound[53]. and the assumption that the energy of the lowest unoccupied molecular orbital (εLUMO) equals –ε_{AP}. Thus, the Fermi level of an undoped elemental semiconductor can be related to its Mulliken's electronegativity. Creating interest in predicting the electronic structure of a species through theoretical calculations involving electronegativity values, group electronegativity concepts for binary compounds were established[54].

$$x_{AB} = \left(x_A^a x_B^b\right)^{1/(a+b)} \tag{2.6}$$

where x_{AB} is the electronegativity of A_aB_b compound, x_A and x_B the Mulliken's electronegativity of elements A and B, a and b are the stoichiometric coefficients. Coupling the results of Nethercot [57], equation 2.7 was estimated to predict the conduction band energy (on NHE scale) of a bulk semiconductor with band gap energy of E_g eV and Mulliken's electronegativity x.

$$E_C = x - 4.5 - 0.5E_g \tag{2.7}$$

2.6 Results and Discussion

The Tauc plots for the synthesized perovskites can be seen in Fig 2.8 to 2.21. The $LaCr_xMn_{1-x}O_3$ and $LaMn_xFe_{1-x}O_3$ species exhibit a linear Tauc plot with no tailing near the lower energy region while $LaCr_xFe_{1-x}O_3$ show a presence of Urbach tail at the lower energy section of the plots. For the $LaCr_xFe_{1-x}O_3$ species, approximately 38% reduction in the band gap energy is observed with the increase in Fe. Multiple band gap energies can be seen in these perovskites. $LaCrO_3$ showed two band gap energies, one of them was the charge transfer gap (C T) due to the electronic transition from O *2p* band state to upper Cr 3*d* band and the other was due to Cr *3d-d* interaction, named the Mott gap. In Fig 2.12, the C T gap for $LaCrO_3$ was estimated to be about 3.09 eV and Mott gap had a value of 2.3 eV. $LaFeO_3$ (refer to Fig 2.8) had a Mott gap of 2.1 eV and C T gap of 1.75 eV. Both the band gaps correlated with literature [55, 56].

A narrowing in band gap energy was visible with the increase in Fe (refer to Fig 2.36). For X= 0.75, 0.5 and 0.25 apart from presence C T gap due to O *2p* –Fe *3d*, a band gap of 1.9 eV (approx.) was observed. Its origin can be attributed to new energy states created due to the interaction of Fe with $LaCrO_3$ lattice. The Urbach energy of $LaCr_xFe_{1-x}O_3$ was higher than the critical values. From Goldschmidt tolerance factor[27] calculated (refer to Table 2.3), deviation from unity indicates distortion in the perovskite structure. Surface segregation can also be a potential source for unique results. As the degree of peak broadening in XRD patterns of these powders were not profound, the large values of Urbach energy can be explained by charge transfer excitons formed by the electrons in the conduction band of Fe/Cr 3*d* states and the holes in valence band of

O 2*p* states[57-59] The MO_6 octahedra network in the perovskite favors the localization of these excitons through phonon coupling at room temperatures[59].

With the increase in higher atomic number transition element, the $LaMn_xFe_{1-x}O_3$ species exhibited similar trends as $LaCr_xFe_{1-x}O_3$, but they possessed no significant Urbach energies in the visible region, which was evident from the absence of tailing in their Tauc plots. With X=0.5 and 0.75 in $LaCr_xFe_{1-x}O_3$, the new energy states in the band gap region were formed due to interaction of Fe in the $LaMnO_3$ lattice and gave rise to a band gap energy of 0.6 eV and 1.05 eV in X =0.5 and 0.75 respectively. For X= 0.25, the electronic structure was dominated by C T transitions between O 2p and Fe/Mn 3d states. The C T gap of $LaMnO_3$ was in good correlation with literature [56].

The trend in band gap energy for $LaCr_xMn_{1-x}O_3$ can be seen in Fig. 2.38. Narrowing of band gap energy with the increase in Mn was noticed. Along with the presence of Mott gap and C T gap, interband states transitions were also visible leading to narrowing of band gap energy in X= 0.5 and 0.25.

The flat band potentials of perovskites measured were fairly consistent at 50 Hz and 100 Hz. The results showed replicability. Apart from $LaCr_{0.5}Fe_{0.5}O_3$, the M.S plots showed two linear regions of different slopes. Region 1 and Region 2 denote the part of the plot closer and farther away from V_{fb} respectively. The non-linear character of M.S plot contributed to the presence of deep and surface states[60, 61].

The surface states become ionized when Fermi level passes through the surface state level, leading to an addition of charge. Thus, an additional capacitance was added in parallel to the space charge capacitance in the equivalent circuit. The phenomenon manifested in the following entities [39] [45, 62]

$$C_{SS} = \frac{e^2 N_{SS} f_{SS}(1-f_{SS})}{kT} \quad (2.9)$$

$$R_{ss} \propto (\frac{kT}{e^2 N_{SS}}) \left(\exp\left(-\frac{E_{SS}}{kT}\right) f_{ss}\right)^{-1} \quad (2.10)$$

where $C_{ss}, R_{SS}, F_{SS}\ and\ N_{SS}$ are the capacitance, resistance, fermi occupation factor, the density of surface states and E_{SS} is energy difference conduction band edge at the surface and the surface state levels.

The position of the Fermi level plays a crucial role. When the Fermi level is close to the surface state level, contribution of the surface state capacitance is significant, but at Fermi level positions below and above the surface state level, the surface state capacitance is negligible [39], hence the M.S plot shows two linear sectors at above and below Fermi level. The Urbach energy calculated for $LaCr_{0.5}Fe_{0.5}O_3$ was lesser compared to its family offered supportive evidence of the contribution of surface states to the electronic structure of these perovskites.

The conduction and valence band edges were deduced from the respective flat band potential of perovskites (refer to Table 2.4). These results were compared with calculations made with electronegativity values (refer appendix A.3). Fig 2.39-41 depicts the trend of CB and VB obtained from flat band potential measurements and electronegativity calculations. For $LaCr_xFe_{1-x}O_3$, there is fairly a reasonable agreement ($\pm 0.3\ V$) with the data obtained from M.S plots and electronegativity calculations, but for the perovskites with Mn, there is a disagreement of the order of $\pm 1\ V$. To address this discrepancy, we need to go back to Mulliken's electronegativity derivations.

The valence states in the electronegativity assessment is ignored when determining CB using the process stated in Chapter 2.5. Mulliken's had established his

scale based on IP and EA through Vleck valence states relating to the species electronic distribution [63].

Arguments could be raised based on the difference between the electronegativity of the ground state isolated atoms and that of in a molecule [64]. As Nethercot [54] derived group electronegativity based on bond lengths for binary stoichiometric compounds, the presence of defects and different crystal phases might give misleading results as these alter the bond lengths of compounds.. For example, CB values of anatase and rutile phase of TiO_2 are different. Hence, it is important here to take into consideration that the perovskites are a mixture of different crystal phase structures. The presence of mixed crystal phases is supported by the similar shifts in diffraction lines observed for similar compositional change thus following Vegard's law and excluding the presence of stress or strain in the lattice. Also, the half-filled electronic configuration of Mn will pose considerable deviations from theoretical electronegativity CB computation. Therefore, the hybridization of the species should be considered in electronegativity calculations.

Though the value of dielectric constant (ε) of the perovskites may vary, from the results of ε Nd we can draw some conjecture, especially for x=0.5 species. As there are two types of donors (Cr^{+3} & Fe^{+3}: $LaCr_xFe_{1-x}O_3$, Mn^{+3} & Fe^{+3}: $LaMn_xFe_{1-x}O_3$, Mn+3 & Cr+3: $LaCr_xMn_{1-x}O_3$), deep states can created. M.S plots have to be frequency independent and linear in nature.

When Vfb measurements were conducted at 1000, 100, 50 and 10 Hz, the MS plots were frequency independent but the presence of two donor deep lying states made them non-linear. At this point, we are left with two options, one being N_d and N'_d

both ionized at flat band potential and the other being either N_d/N'_d ionized or not ionized at flat band potential. Due to the complex nature of the obtained M.S plots the later option needs to be taken into consideration. This results in $\sigma(x)$ being potentially dependent, and the interfacial capacitance expression becomes [43, 60]

$$C_{SC} = \left(\frac{\varepsilon\varepsilon_o}{2}\right)^{0.5} \frac{\emptyset(\Delta\partial_{SC})}{\left[\int_0^{\Delta\partial SC} \emptyset(\Delta\partial) d\Delta\partial\right]^{0.5}} \quad (2.11)$$

$\Delta\partial$ is the potential difference between bulk and SC, $\emptyset\Delta\partial$ is $\sigma(x)$ at $x = \Delta\partial$. For a semiconductor of n- type with M discrete donor levels [43, 60] $\emptyset\Delta\partial$ is given as below

$$\emptyset\Delta\partial = q\left\{\sum_{i=1}^{M} N_{d_i}\left[1 + exp\left(\frac{E_F - E_{d_i} - q\Delta\partial}{kT}\right)\right]^{-1} - N_c exp\left(\frac{E_F - E_c - q\Delta\partial}{kT}\right)\right\} \quad (2.12)$$

where N_C is the effective density of states at E_C and N_{d_i} is the density of donor states in the i[th] level with E_{d_i} energy.

For a semiconductor of n- type with localized states given by density states functions [60]

$$\emptyset\Delta\partial = q\int_{-\infty}^{+\infty} D(E)\left\{\left[1 + exp\left(\frac{E - E_F}{kT}\right)\right]^{-1} - \left[1 + \exp\left(\frac{E - E_F + q\Delta\partial}{kT}\right)\right]^{-1}\right\} dE \quad (2.13)$$

Comparison of curves based on above both conditions suggested tailing localized states below the conduction band level. The slopes of these curves increase with an increase in applied potential. The capacity at higher potentials was nearly potential independent indicating the constant nature of these localized states.

The results of absorbance spectrum correlated well with the prediction of localized states. Chemical intuition from the band gap energy suggested a sandwiching of the two participating transition metals d bands. The energy level calculations of these

localized states though possible through the solution of the above equations are out of the scope of this discussion.

Table 2.5 gives the approximate band energy levels of the perovskites. Within the assumptions of our V_{fb} measurement the error in band edge determination is not more than $\pm$ 0.1 V vs SCE. The band gap energy determined through DRS measurements were used in the calculation of valence band edge.

Table 2.5 (a) Conduction and valence band edges of $LaCr_xMn_{1-x}O_3$

Perovskite	**Conduction Band** V vs NHE	**Valence Band** V vs NHE		
		Cr d-d	**o2p-Mn3d**	**forbidden**
$LaCrO_3$	-0.887±0.01	1.408±0.00	-	2.203±0.01
$LaCr_{0.75}Mn_{0.25}O_3$	-0.943±0.03	1.257±0.03	0.157±0.03	0.357±0.03
$LaCr_{0.5}Mn_{0.5}O_3$	-0.903±0.02	-	-	-0.003±0.02
$LaCr_{0.25}Mn_{0.75}O_3$	-0.768±0.02	-	-	0.082±0.02
$LaMnO_3$	-0.624±0.06	0.376±0.06	0.376±0.06	-

Table 2.5 (b) Conduction and valence band edges of $LaCr_xFe_{1-x}O_3$

Perovskite	**Conduction Band** V vs NHE	**Valence Band** V vs NHE		
		Cr d-d	**o2p-Fe3d**	**Forbidden**
$LaCrO_3$	-0.887±0.01	1.408±0.00	-	2.203±0.01
$LaCr_{0.75}Fe_{0.25}O_3$	-0.861±0.01	-	0.989±0.01	1.079±0.01
$LaCr_{0.5}Fe_{0.5}O_3$	-0.565	-	1.185	1.335
$LaFeO_3$	-0.388±0.01	-	1.362±0.01	1.712±0.01

Table 2.5 (c) Conduction and valence band edges of $LaMn_xFe_{1-x}O_3$

Perovskite	Conduction Band	Valence Band V vs NHE	
	V vs NHE	**o2p-Fe3d**	**forbidden**
$LaMnO_3$	-0.624±0.06		0.376±0.06
$LaMn_{0.75}Fe_{0.25}O_3$	-0.865±0.02	0.635±0.02	-0.065±0.02
$LaMn_{0.5}Fe_{0.5}O_3$	-0.9825±0.03		-0.3825±0.03
$LaMn_{0.25}Fe_{0.75}O_3$	-0.6205	0.8795±0.02	0.4295±0.02
LaFeO3	-0.388±0.01	1.362±0.01	1.712±0.01

2.7 Conclusions

A significant amount of reduction in band gap energy has been achieved in the synthesized perovskites to a point in the near infra-red and visible region of the solar spectrum. The sandwiching effect of participating transition metals d bands with O 2p band results in localized state transitions that enabled the utilization of varied levels of solar energy for photocatalysis (refer to Section 3.1). The conduction band edge and valence band edge alignments for specific perovskites allow for CO_2 reduction, water splitting and dye degradation (refer to Table 3.1). Although we were able to tune the band structure of these perovskites, limitations in terms of their electron-hole recombination rates, adsorption properties, and chemical stability still needs to be studied and modified to obtain better rates of photocatalysis.

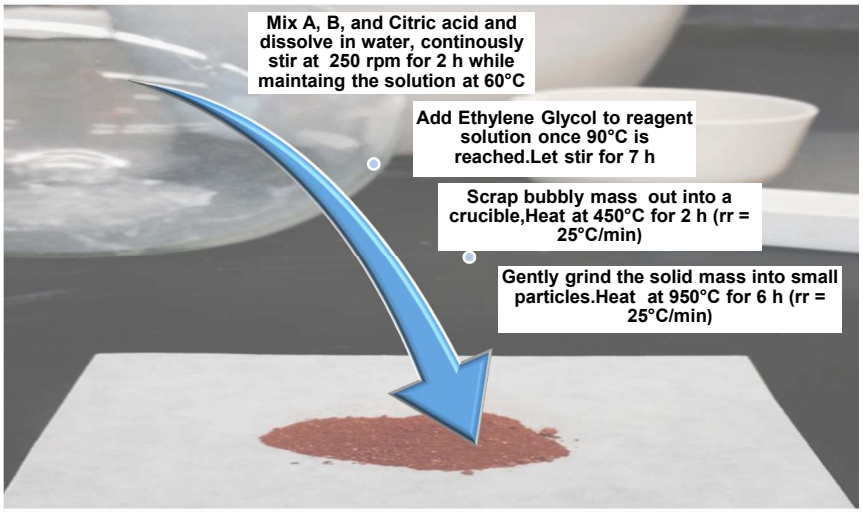

Figure 2.1 Synthesis scheme

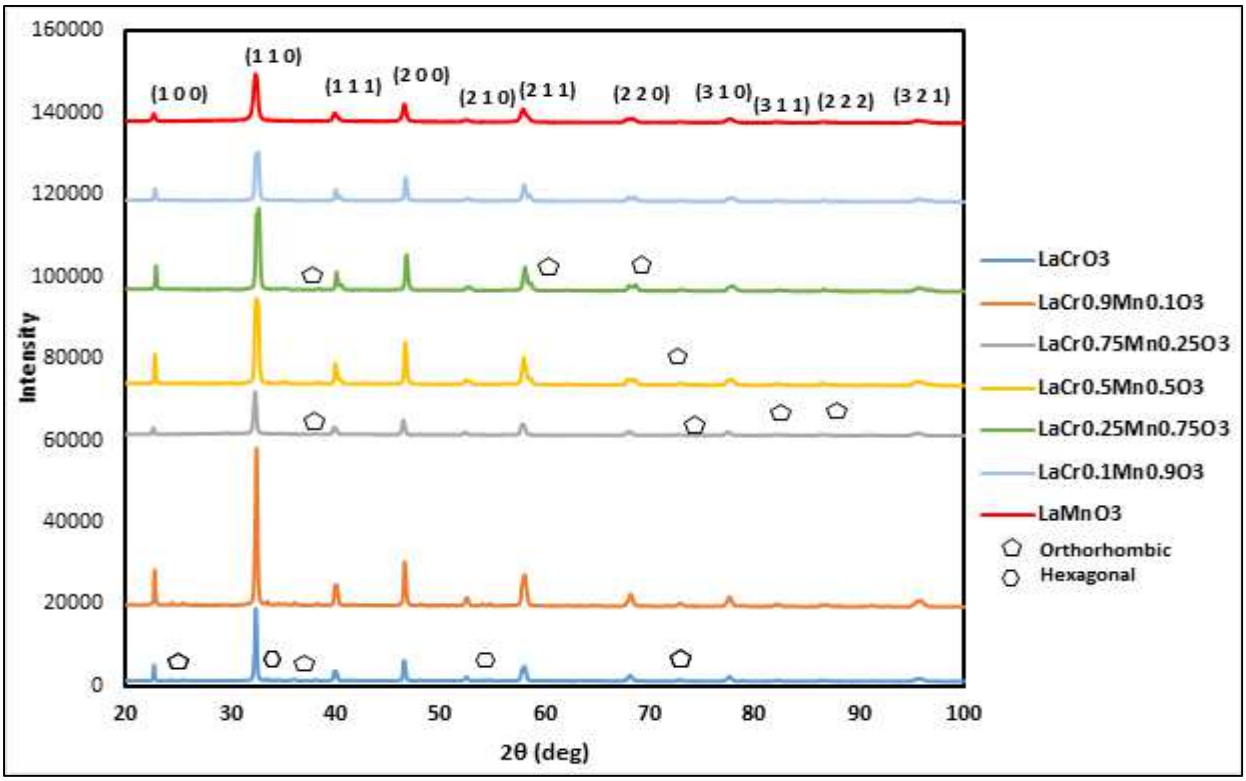

Figure 2.2 XRD patterns for $LaCr_xMn_{1-x}O_3$

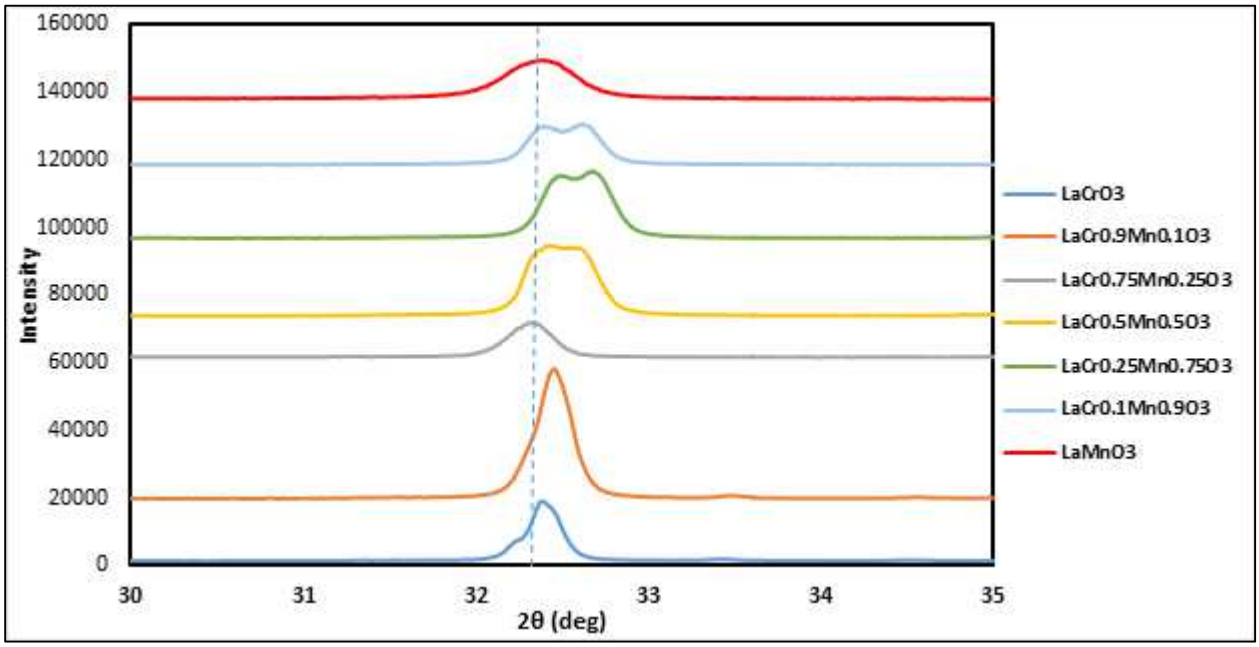

Figure 2.3 (1 1 0) XRD shifts for $LaCr_xMn_{1-x}O_3$

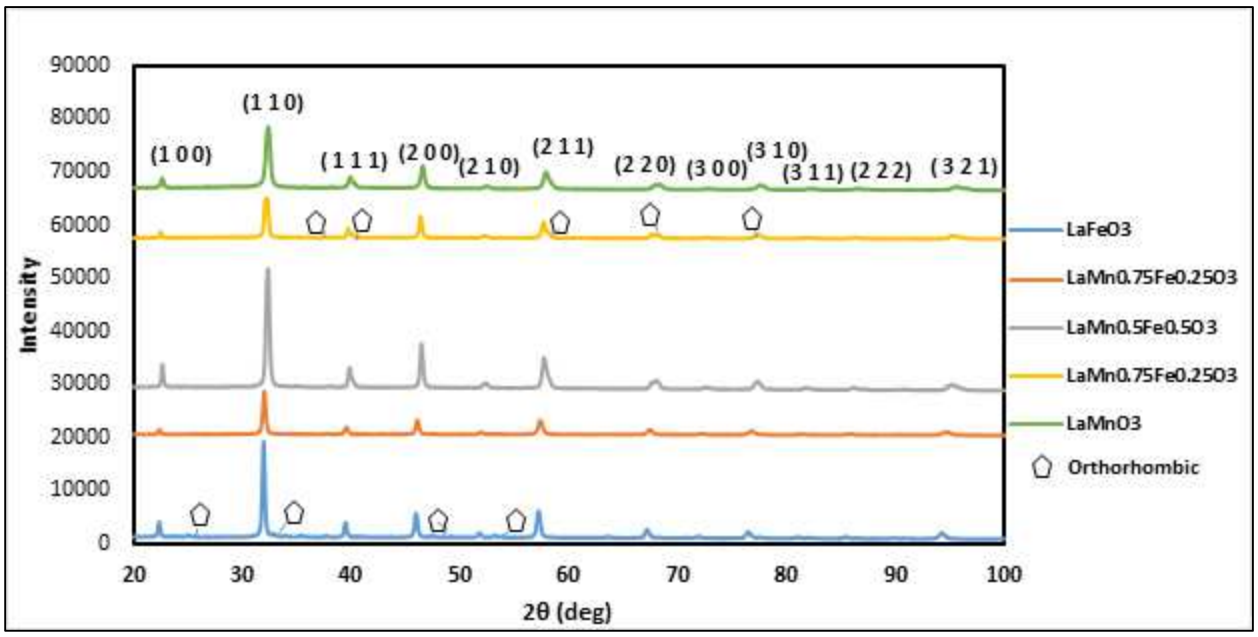

Figure 2.4 XRD patterns for $LaMn_xFe_{1-x}O_3$

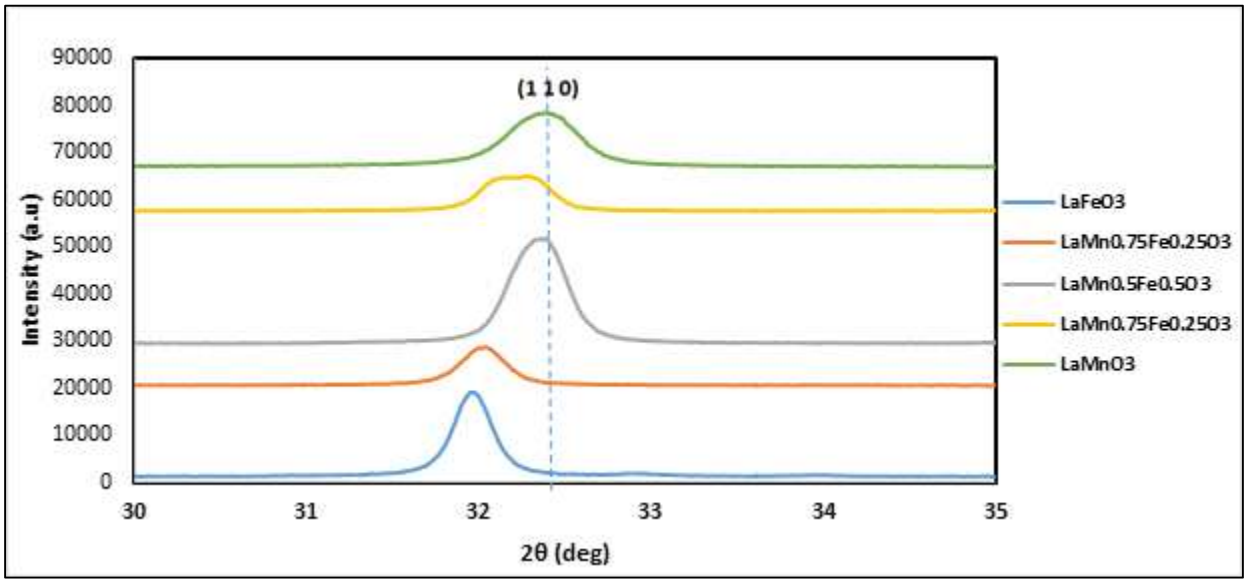

Figure 2.5 (1 1 0) XRD shifts for $LaMn_xFe_{1-x}O_3$

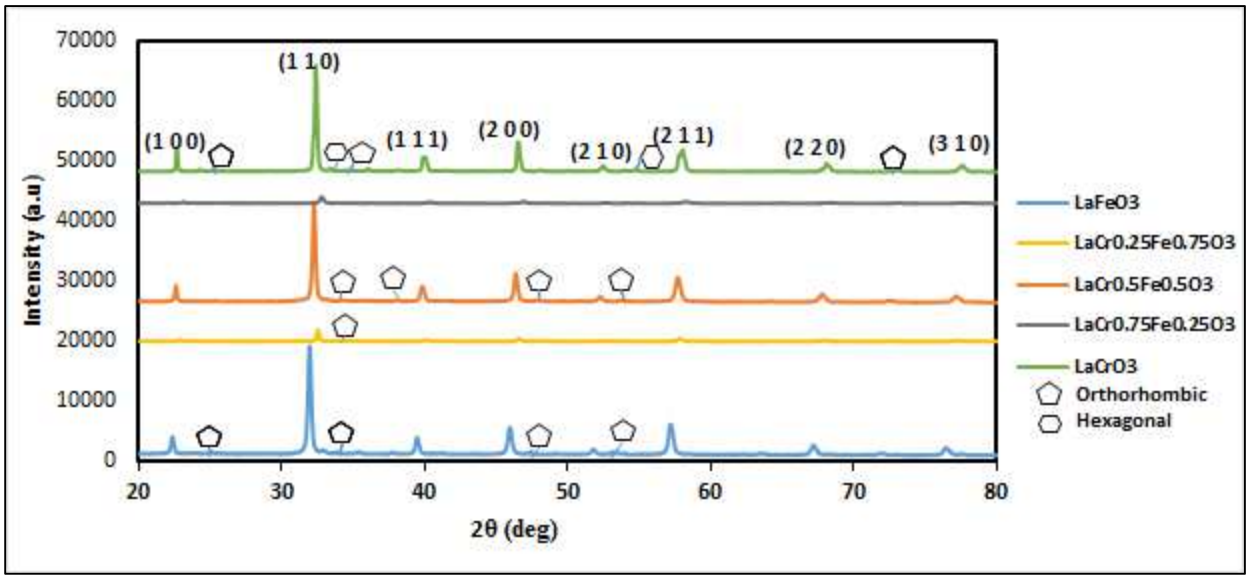

Figure 2.6 XRD patterns for $LaCr_xFe_{1-x}O_3$

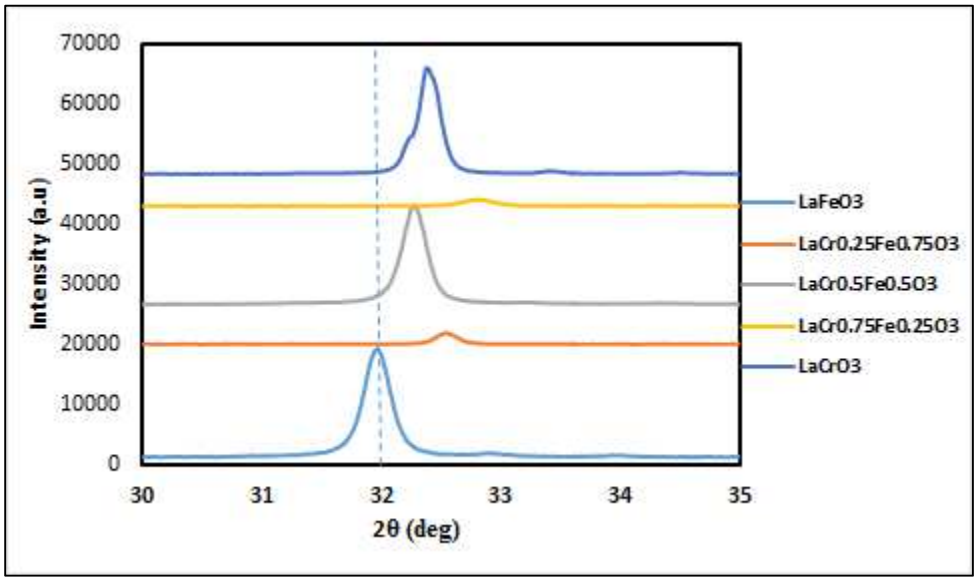

Figure 2.7 (1 1 0) XRD shifts for $LaCr_xFe_{1-x}O_3$

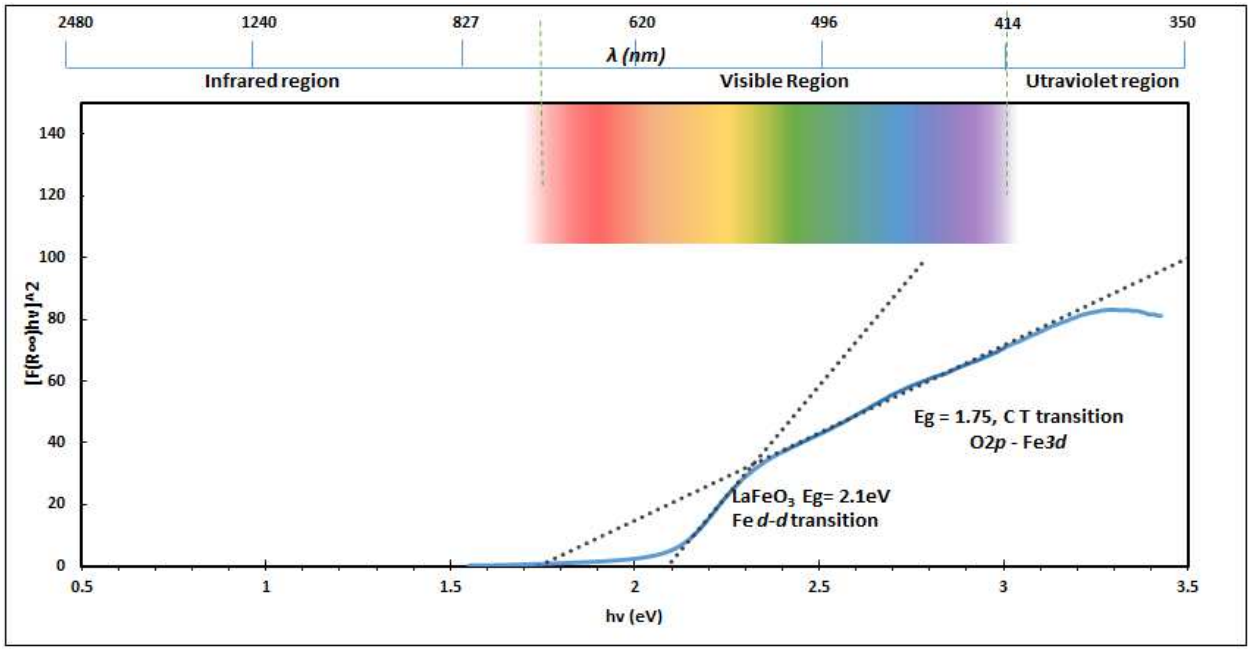

Figure 2.8 (a) Tauc plot for $LaFeO_3$

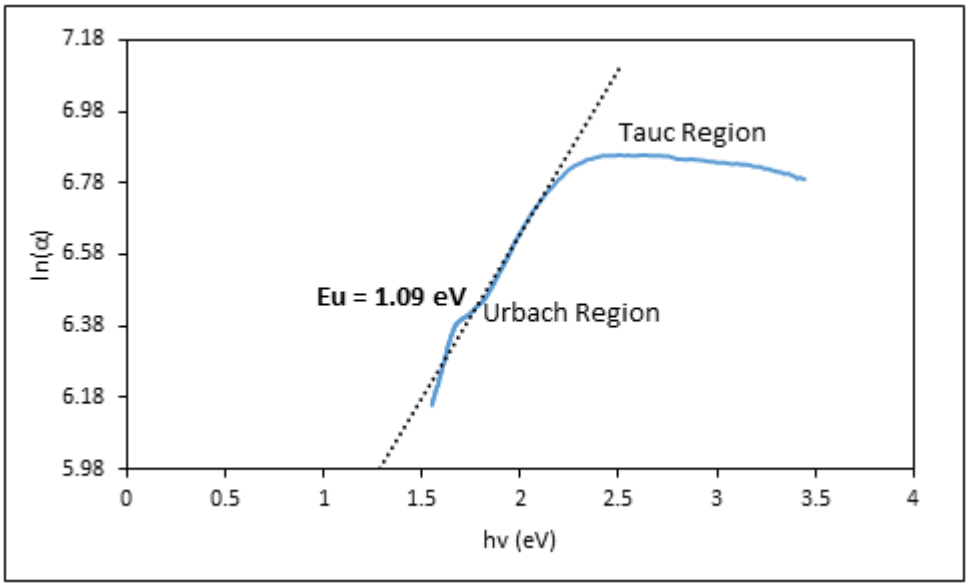

Figure 2.8 (b) Urbach energy plot for $LaFeO_3$

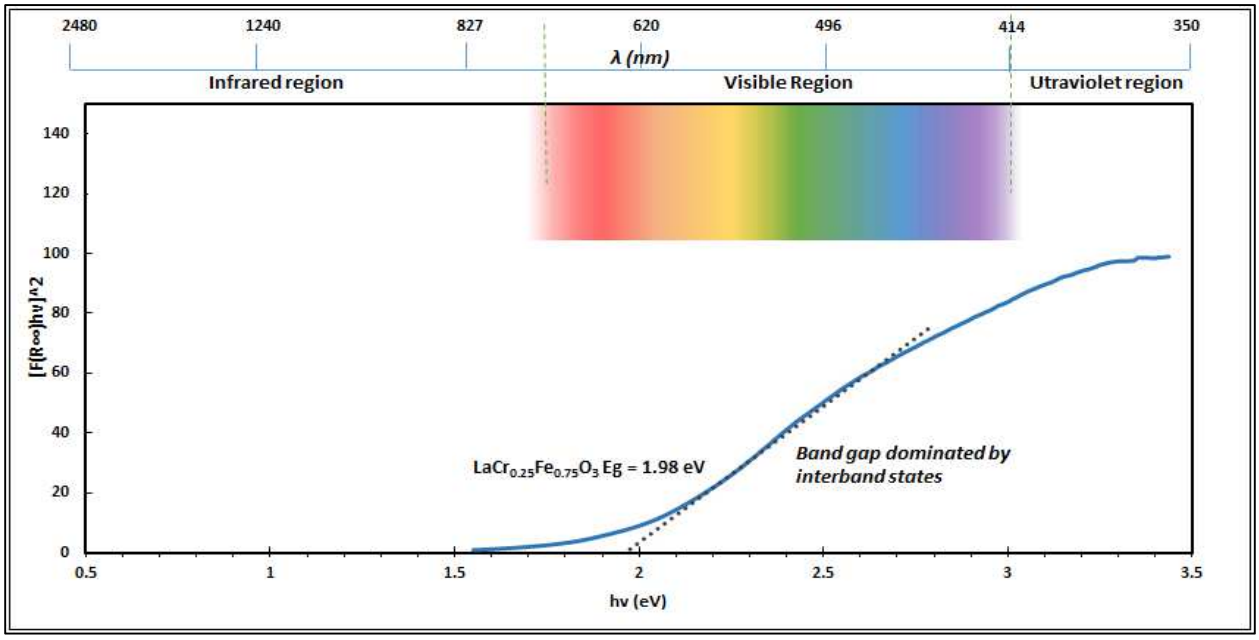

Figure 2.9 (a) Tauc plot for $LaCr_{0.25}Fe_{0.75}O_3$

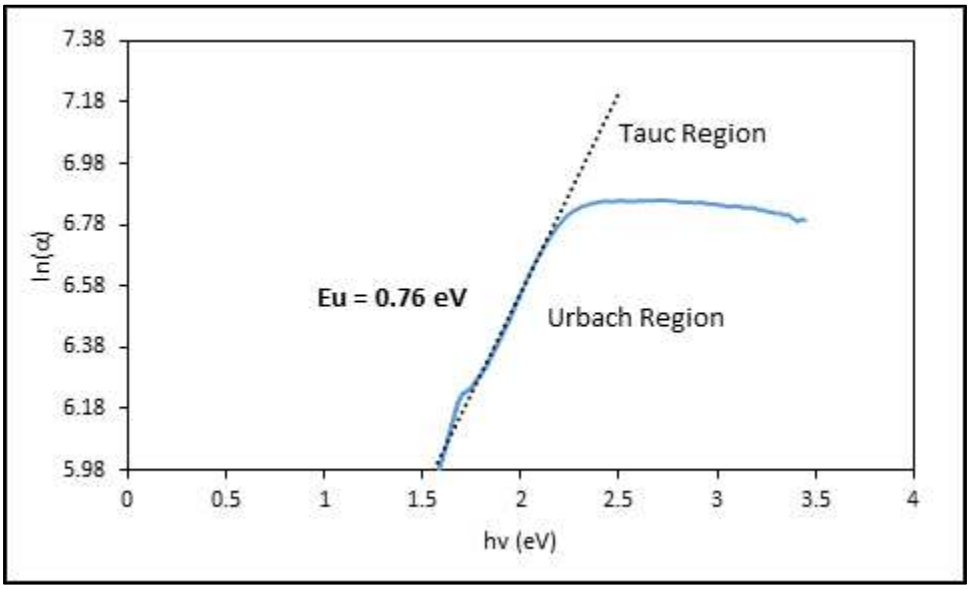

Figure 2.9 (b) Urbach energy plot for $LaCr_{0.25}Fe_{0.75}O_3$

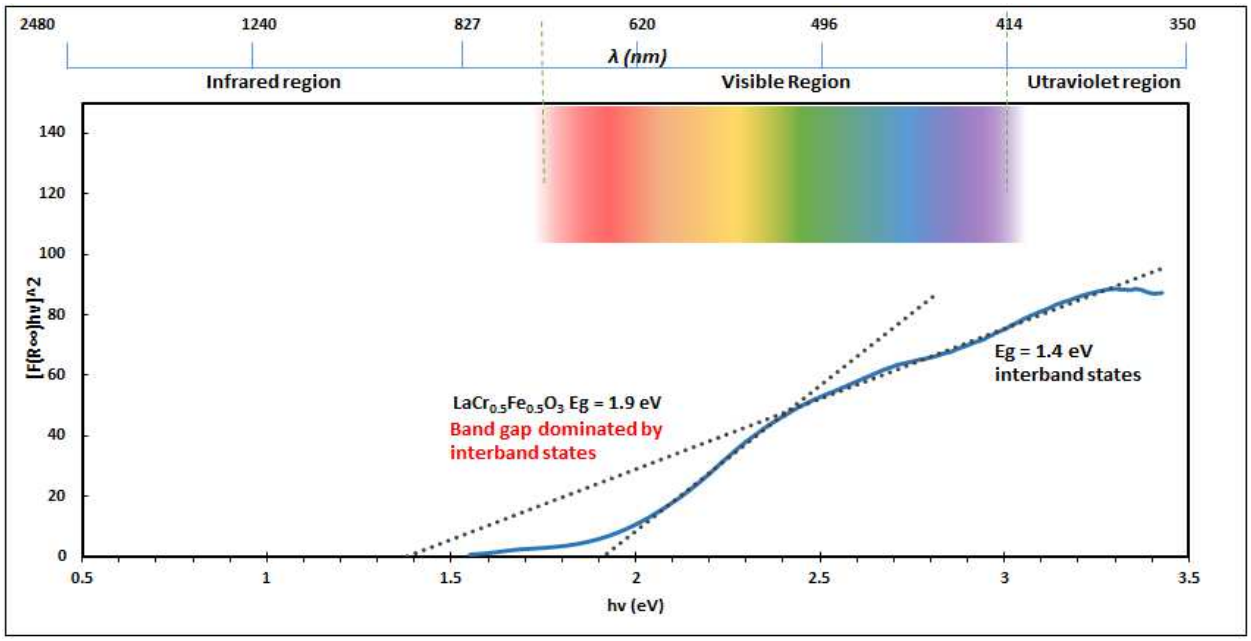

Figure 2.10 (a) Tauc plot for $LaCr_{0.5}Fe_{0.5}O_3$

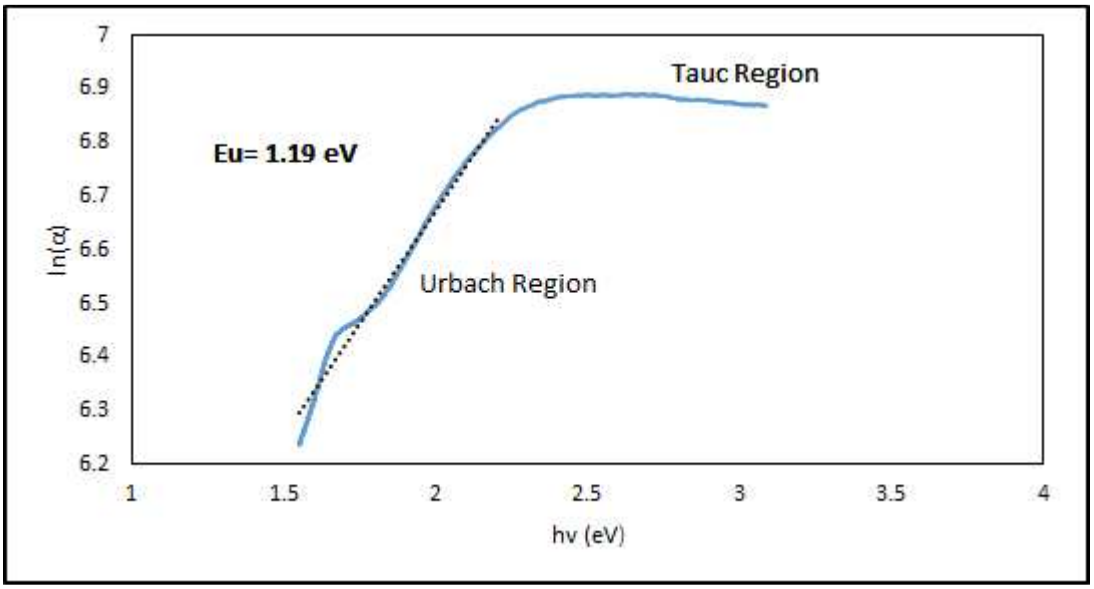

Figure 2.10 (b) Urbach energy plot for $LaCr_{0.5}Fe_{0.5}O_3$

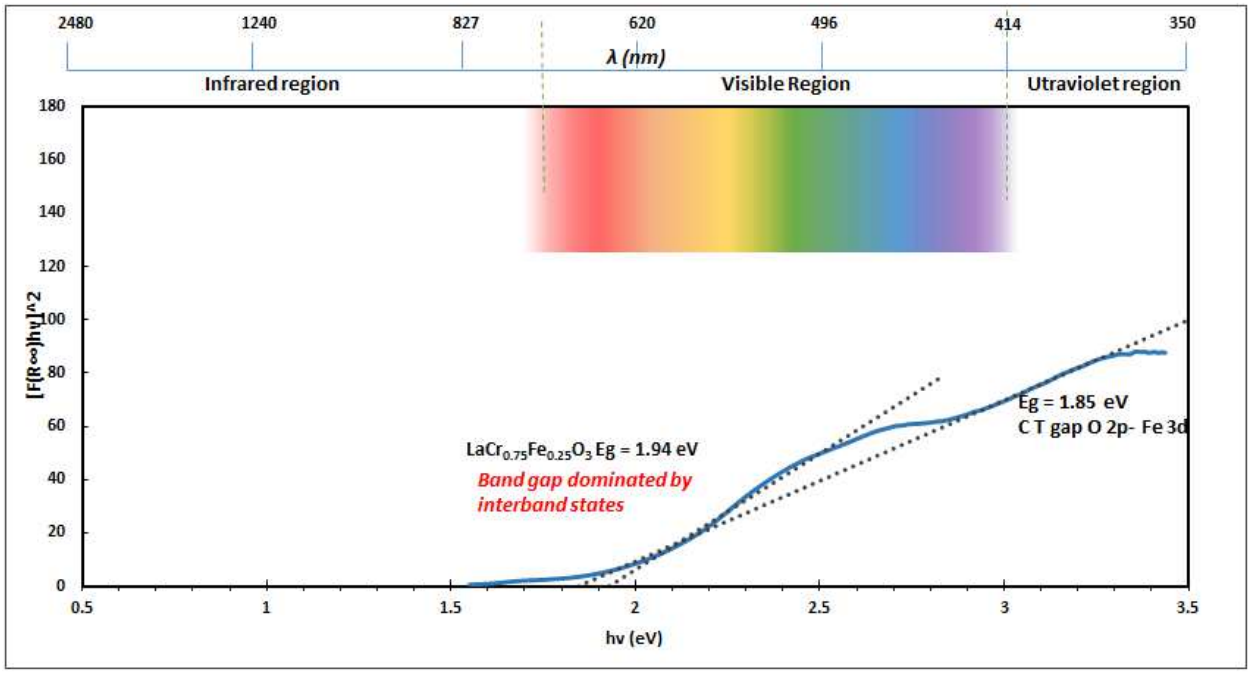

Figure 2.11 (a) Tauc plot for $LaCr_{0.75}Fe_{0.25}O_3$

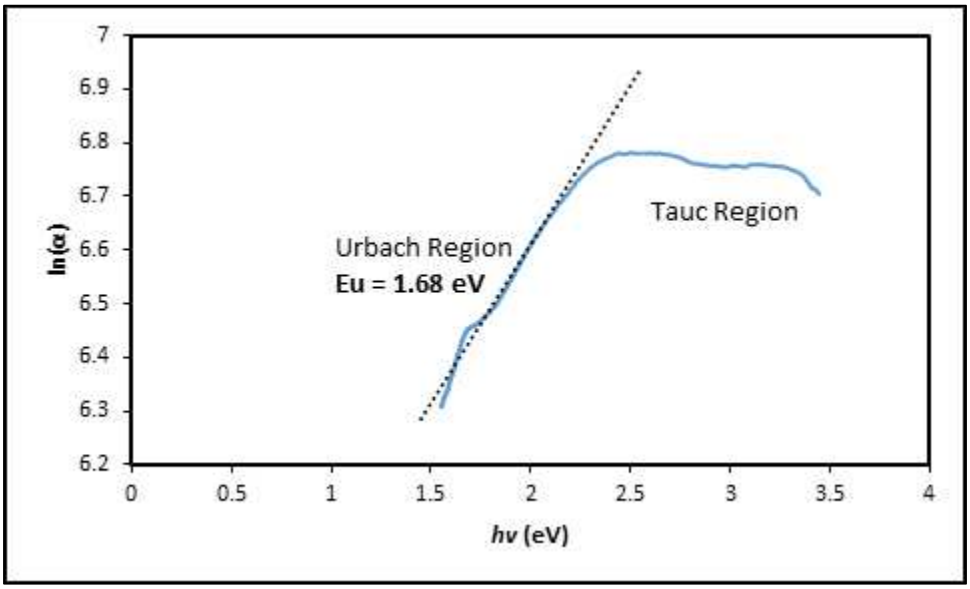

Figure 2.11 (b) Urbach energy plot for $LaCr_{0.75}Fe_{0.25}O_3$

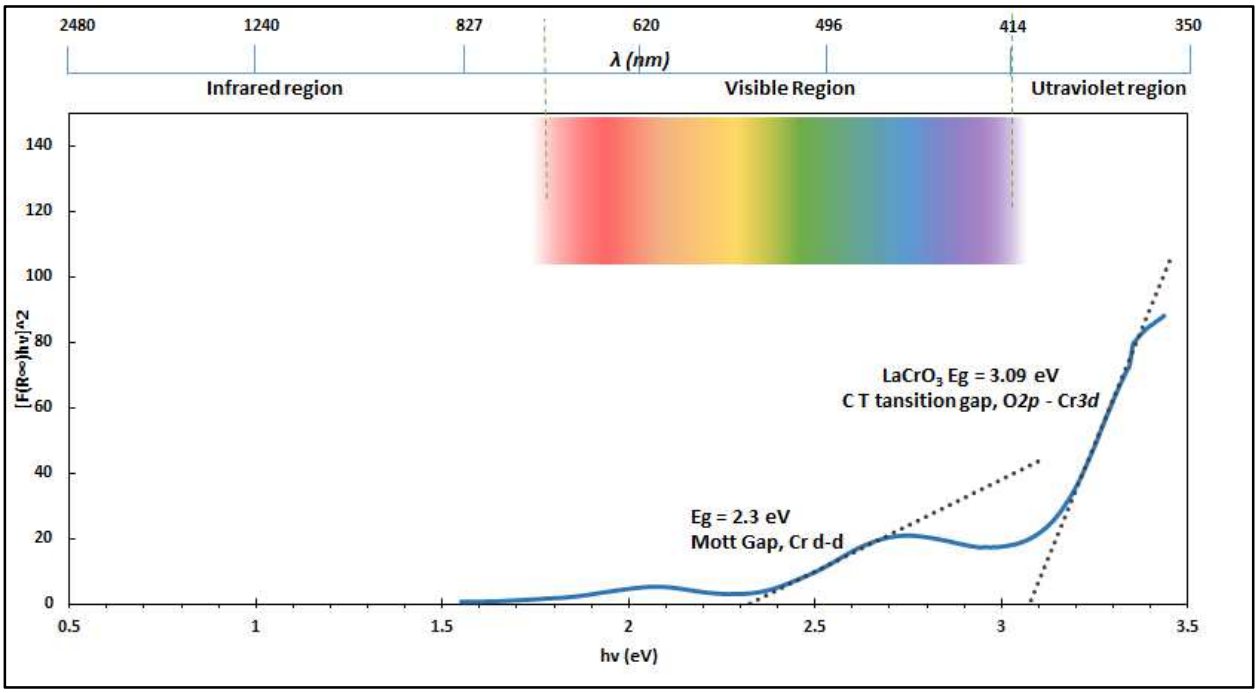

Figure 2.12 (a) Tauc plot for $LaCrO_3$

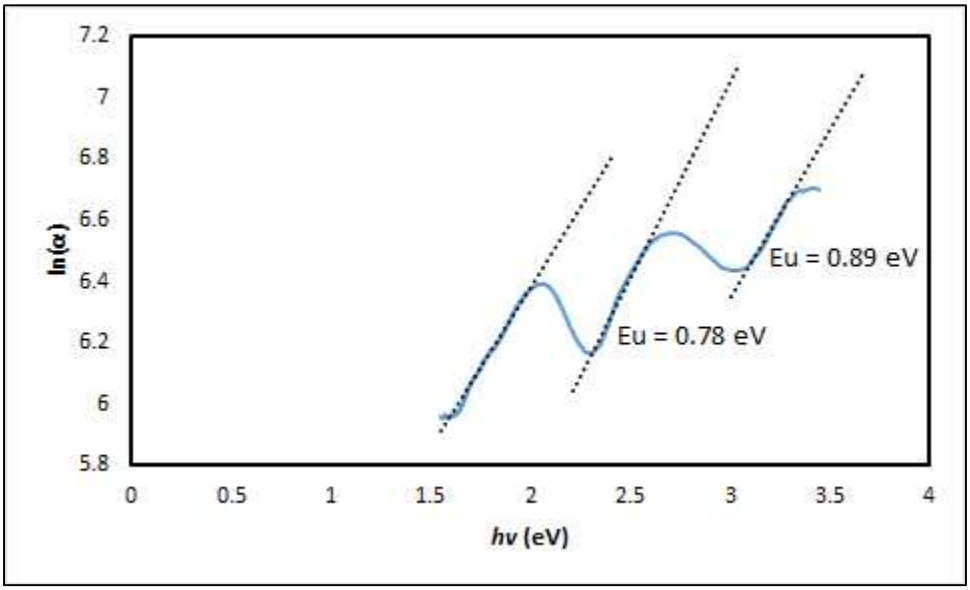

Figure 2.12 (b) Urbach energy plot for $LaCrO_3$

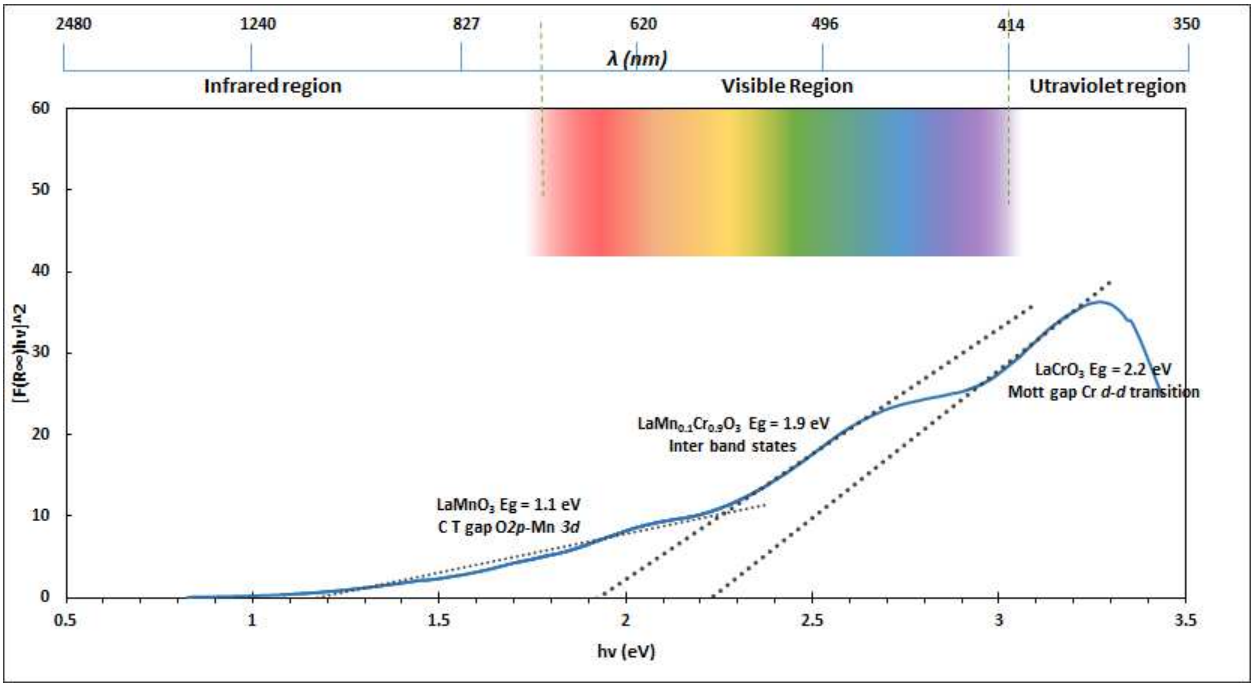

Figure 2.13 Tauc plot $LaCr_{0.9}Mn_{0.1}O_3$

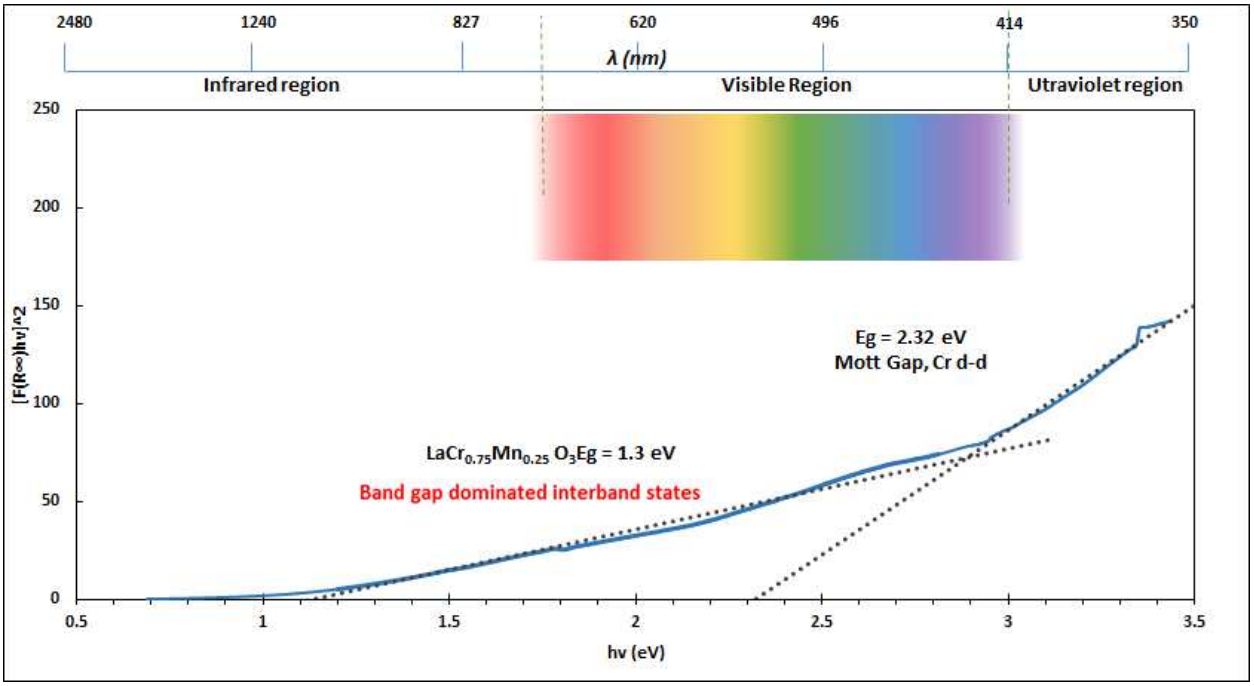

Figure 2.14 Tauc plot $LaCr_{0.75}Mn_{0.25}O_3$

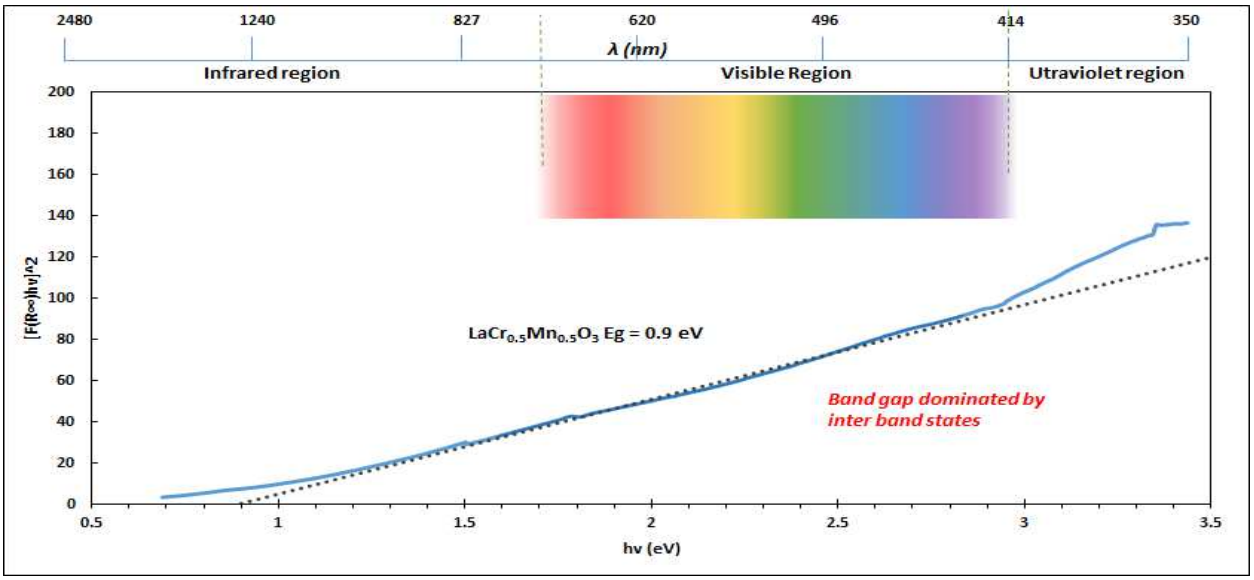

Figure 2.15 Tauc plot $LaCr_{0.5}Mn_{0.5}O_3$

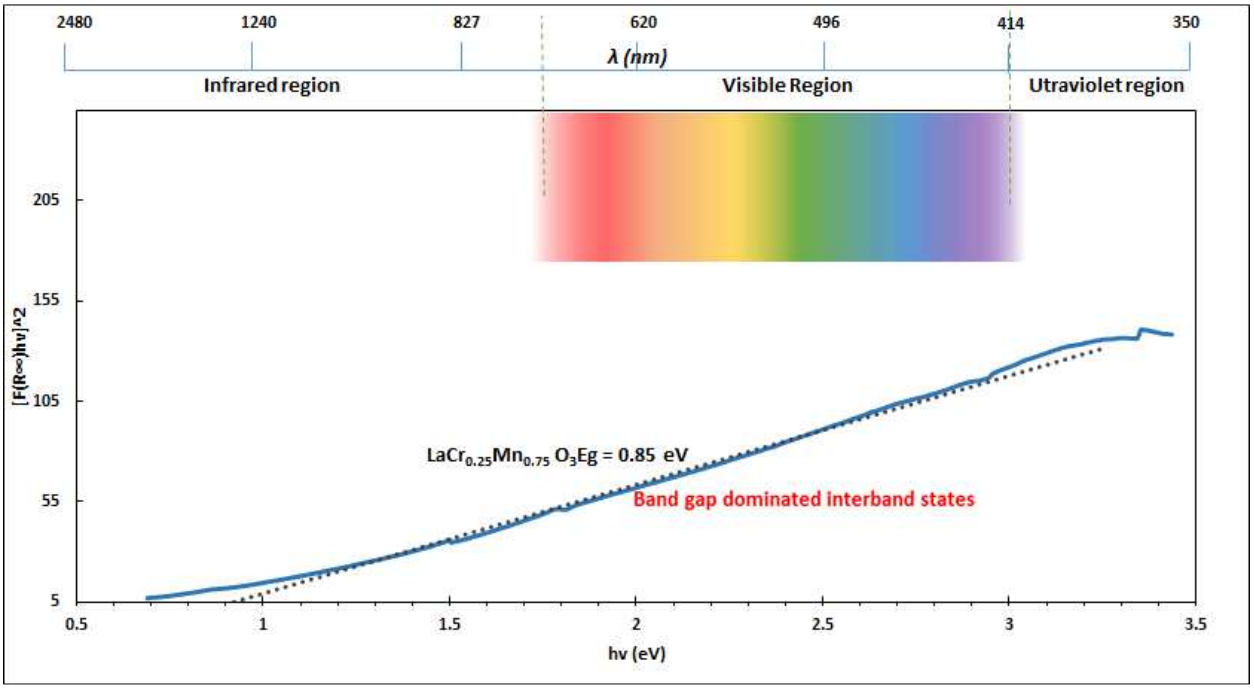

Figure 2.16 Tauc plot $LaCr_{0.25}Mn_{0.75}O_3$

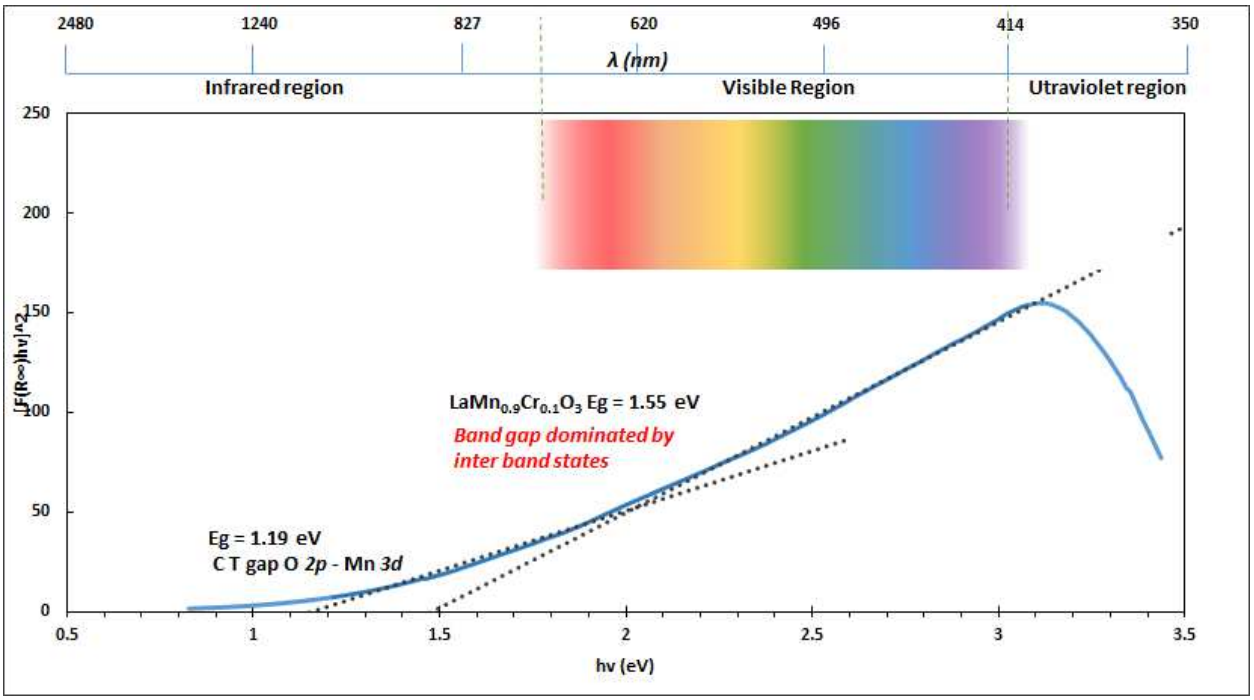

Figure 2.17 Tauc plot $LaCr_{0.1}Mn_{0.9}O_3$

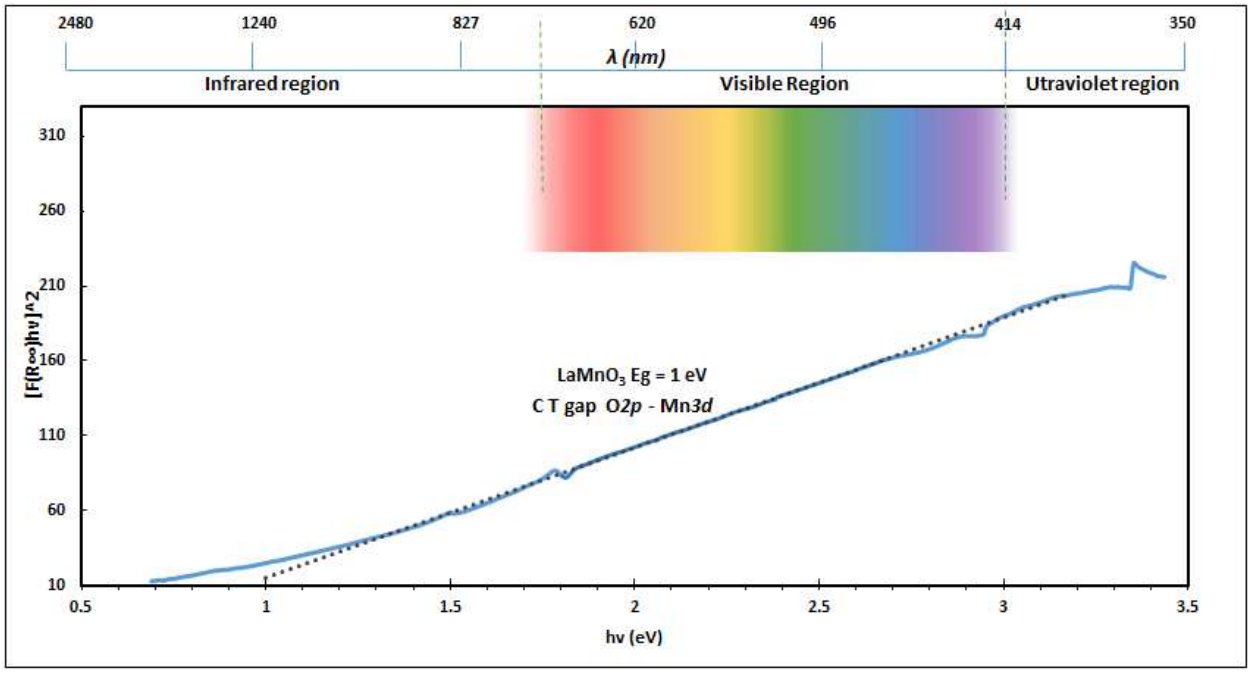

Figure 2.18 (a) Tauc plot for $LaMnO_3$

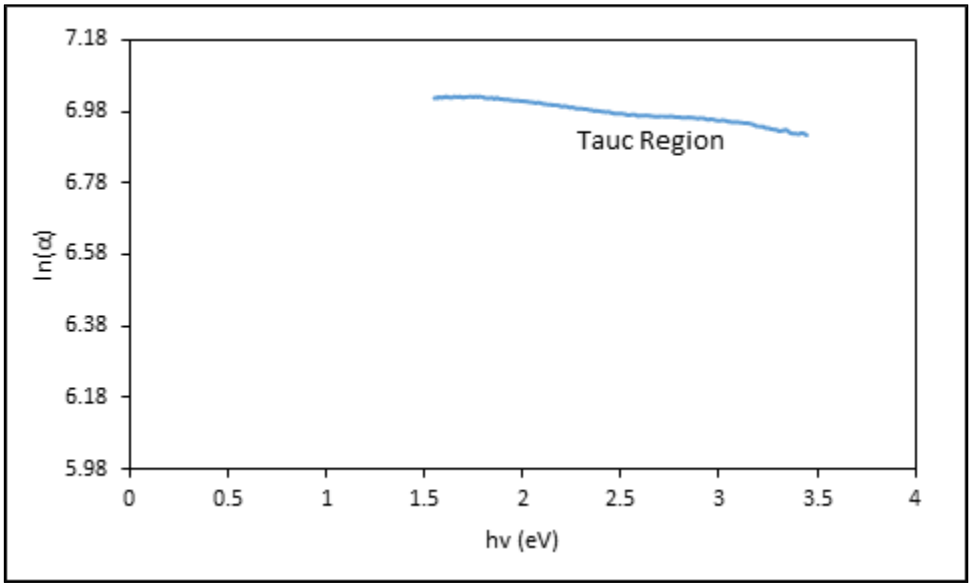

Figure 2.18 (b) Urbach energy plot $LaMnO_3$

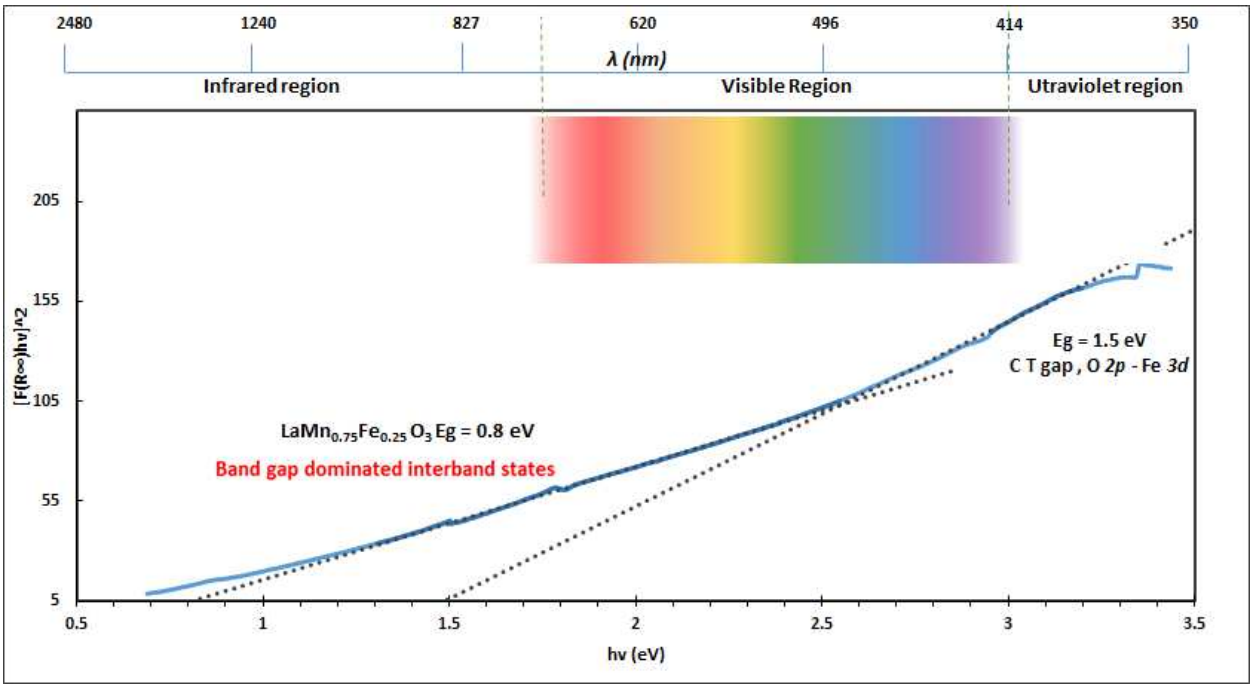

Figure 2.19 (a) Tauc plot $LaMn_{0.75}Fe_{0.25}O_3$

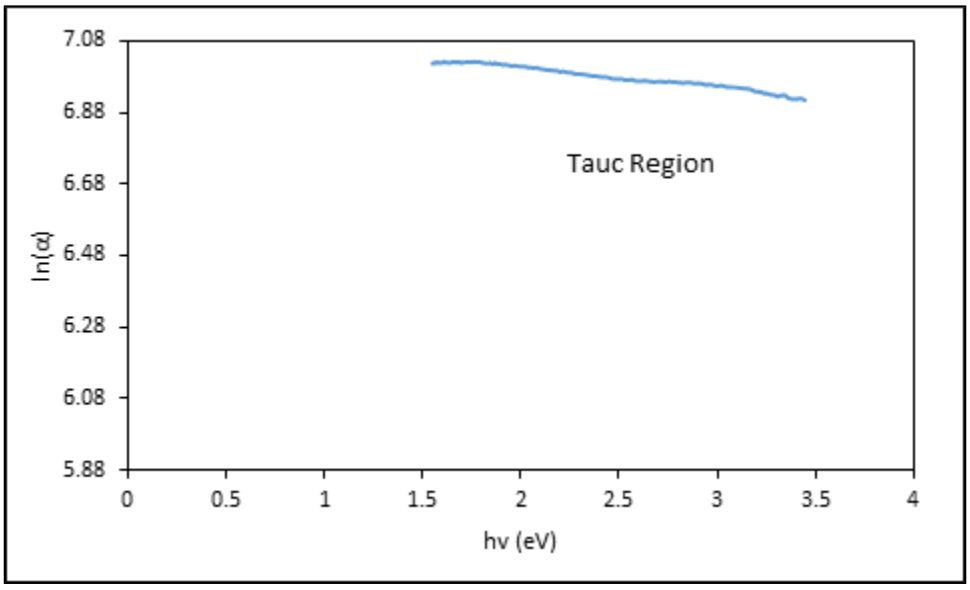

Figure 2.19 (b) Urbach energy plot $LaMn_{0.75}Fe_{0.25}O_3$

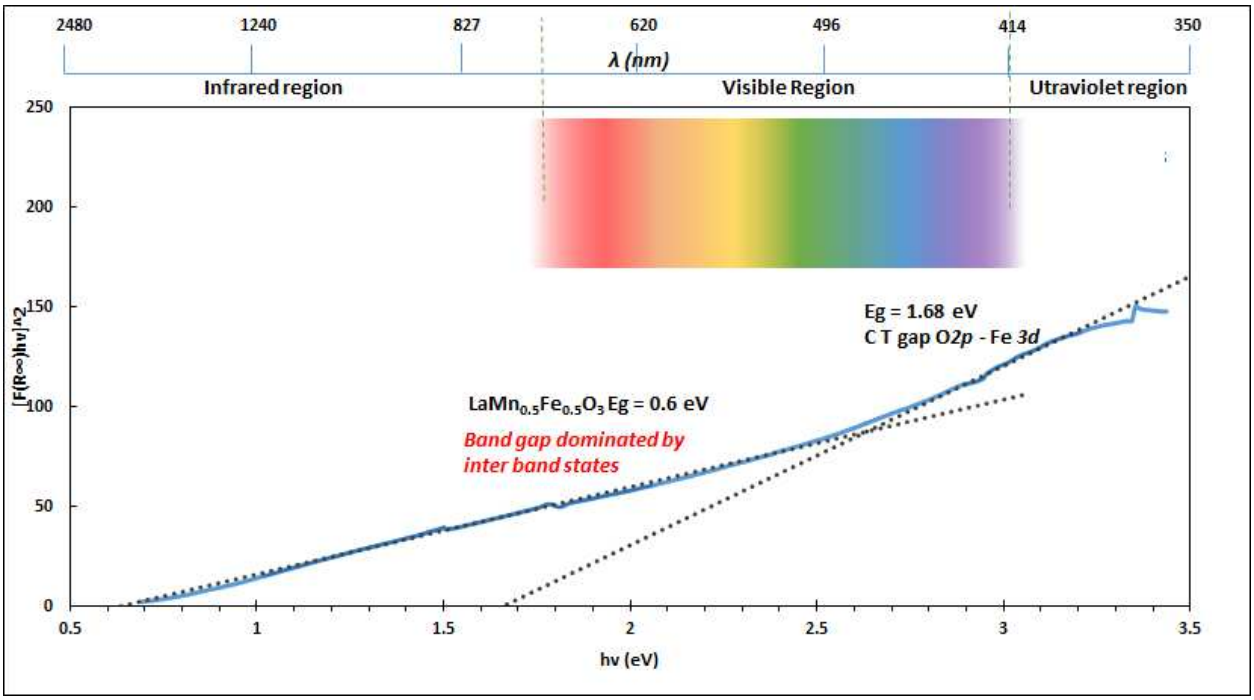

Figure 2.20 (a) Tauc plot $LaMn_{0.5}Fe_{0.5}O_3$

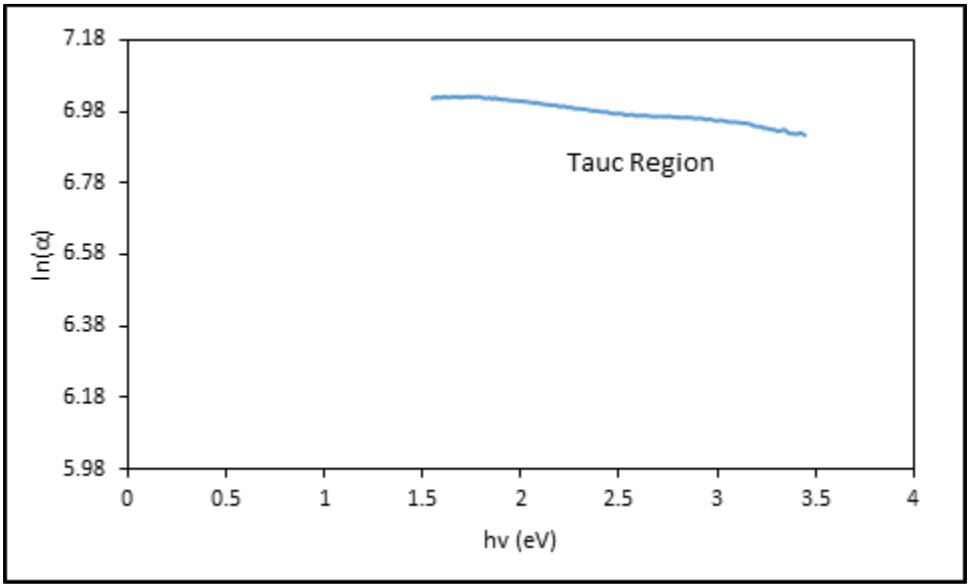

Figure 2.20 (b) Urbach energy plot $LaMn_{0.5}Fe_{0.5}O_3$

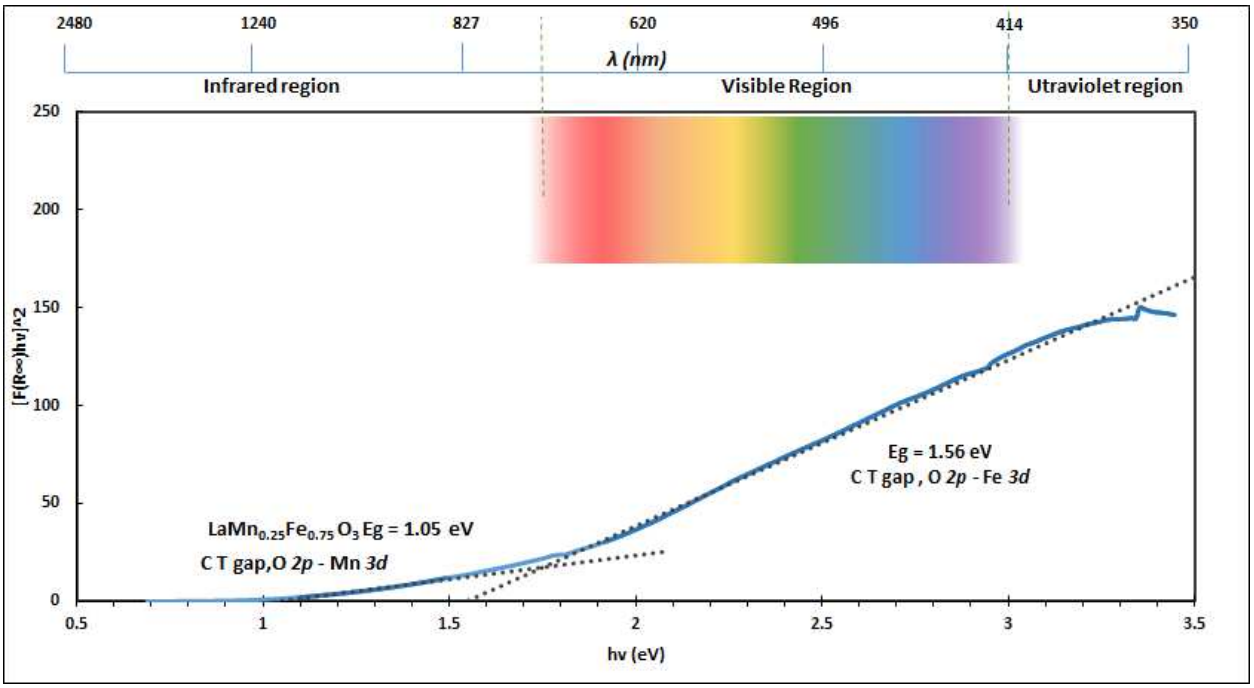

Figure 2.21 (a) Tauc plot $LaMn_{0.25}Fe_{0.75}O_3$

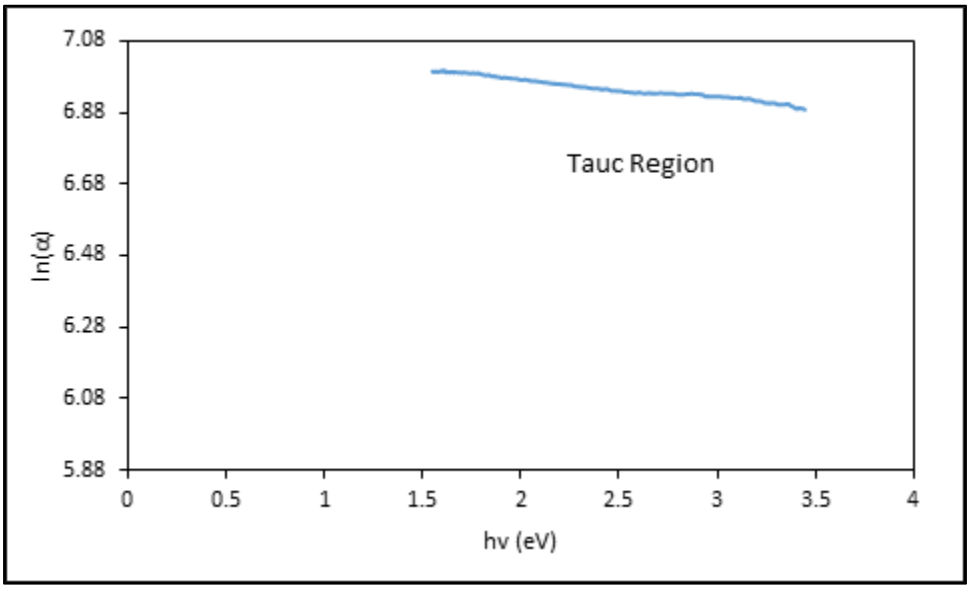

Figure 2.21 (b) Urbach energy plot $LaMn_{0.25}Fe_{0.75}O_3$

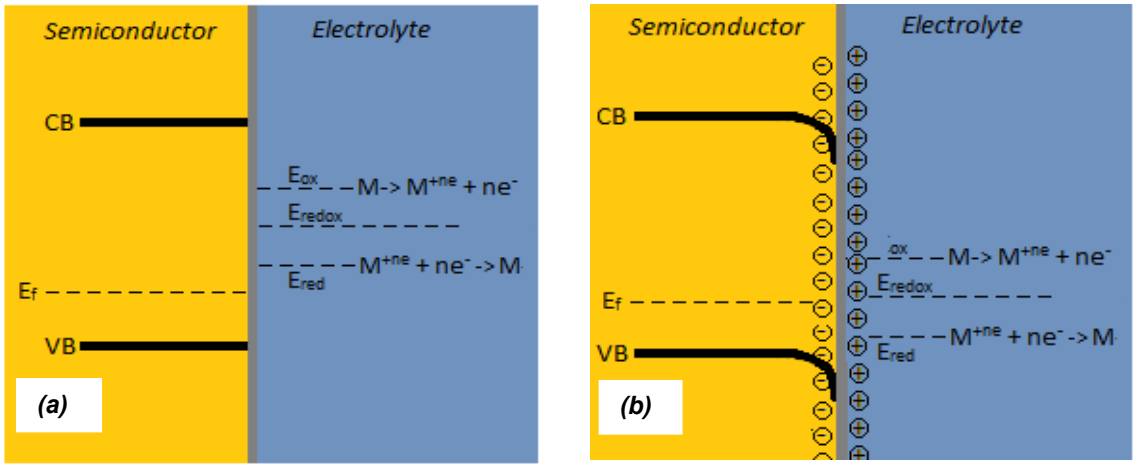

Figure 2.22 (a) Energy levels of p- type semiconductor in contact with an electrolyte, **(b)** Band bending for a p-type semiconductor

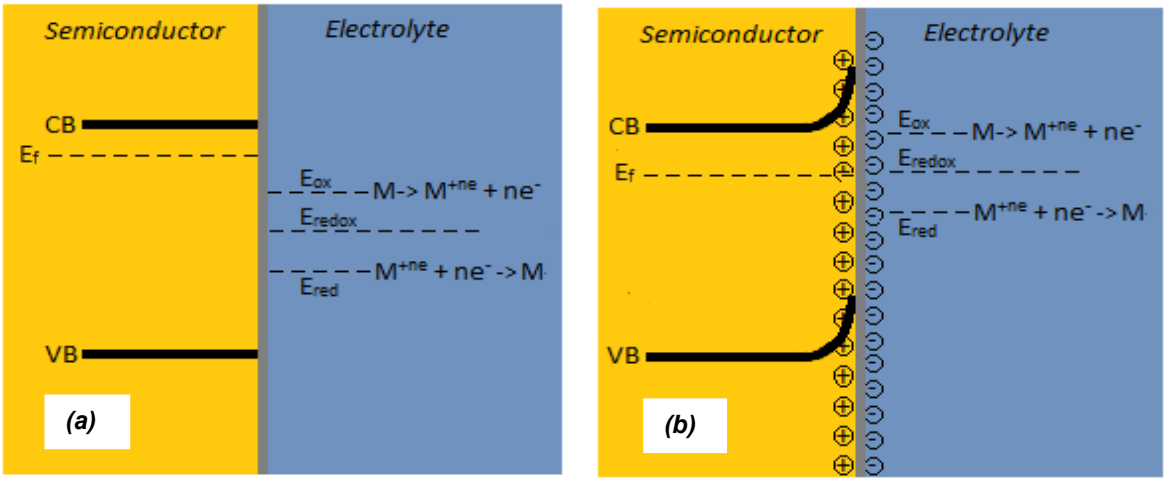

Figure 2.23 (a) Energy levels of n- type semiconductor in contact with an electrolyte, **(b)** Band bending for a n-type semiconductor

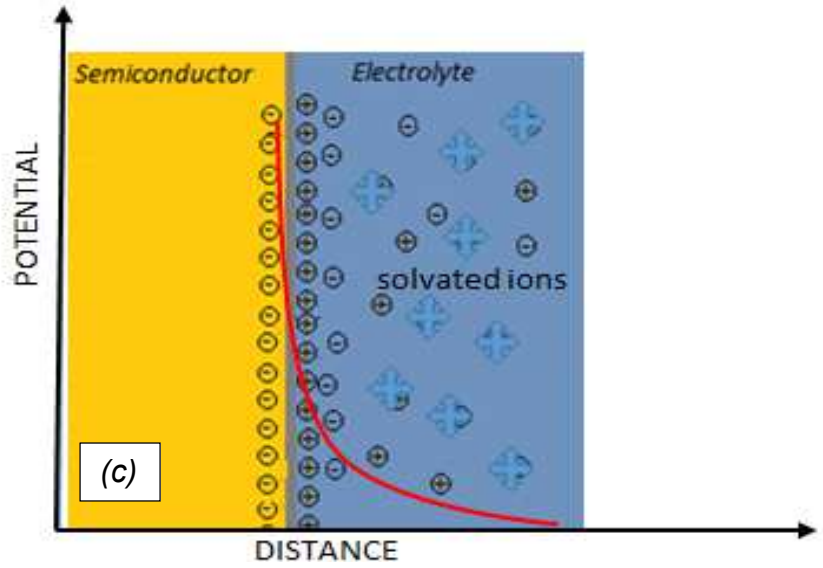

Figure 2.23 (c) Potential profile over the semiconductor-electrolyte regions

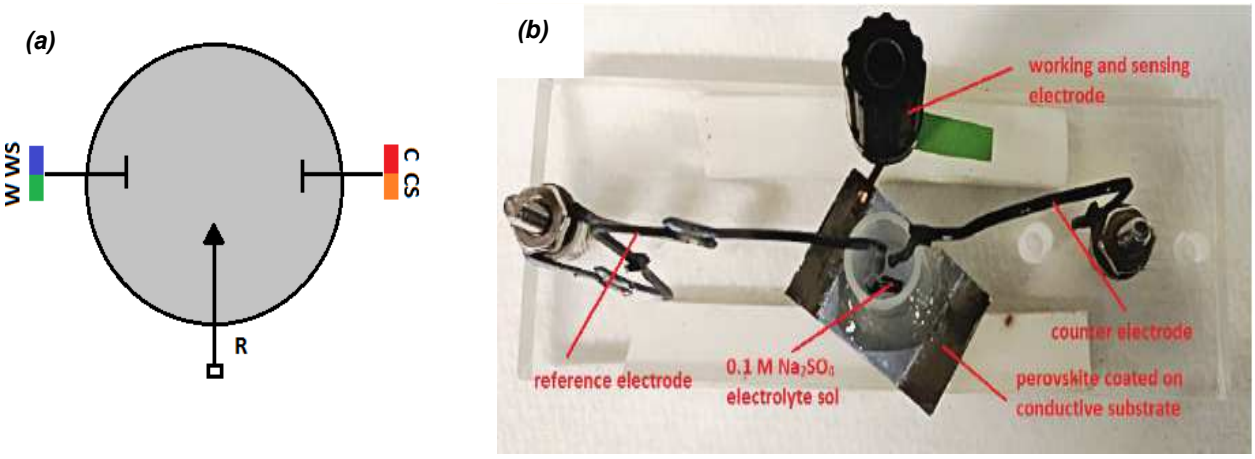

Figure 2.24 (a) M.S electrode setup; **(b)** M.S sample setup

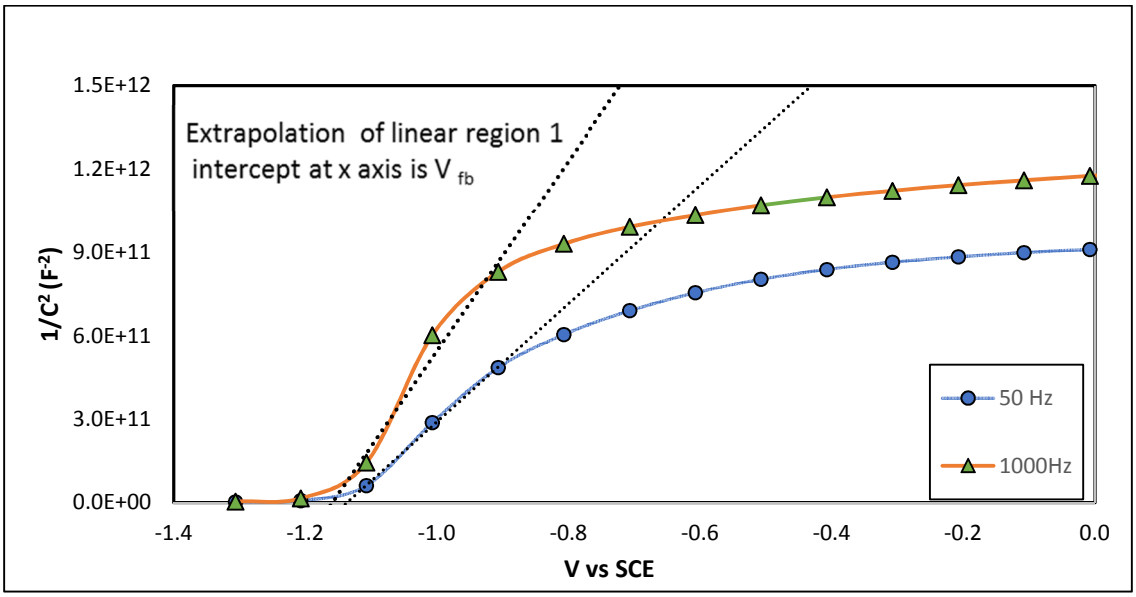

Figure 2.25 (a) Mott Schottky plot for $LaCrO_3$ sample I

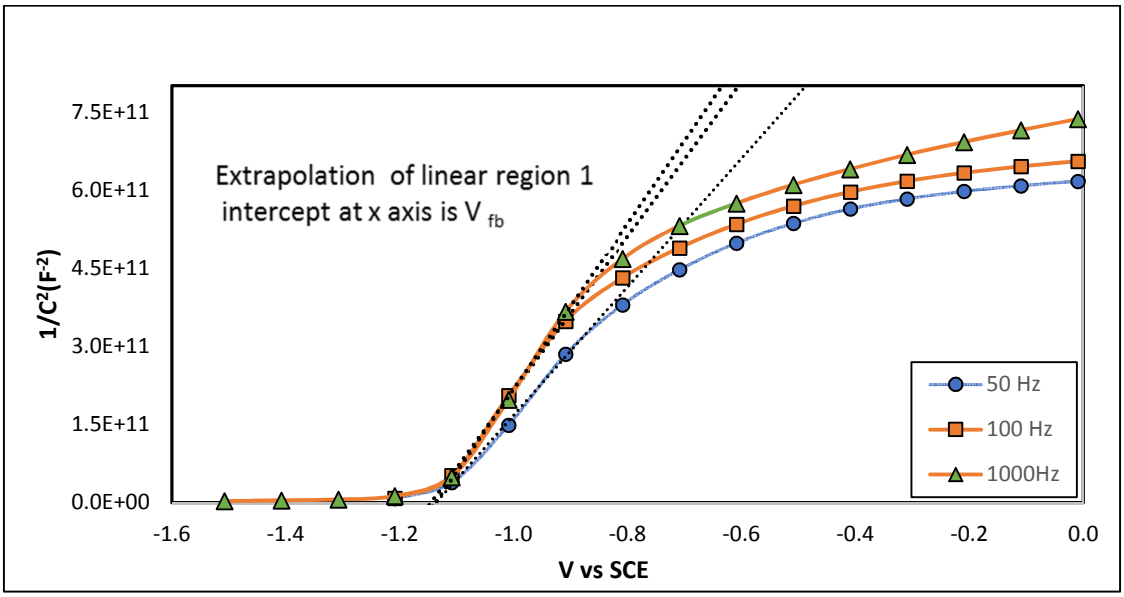

Figure 2.25 (b) Mott Schottky plot for $LaCrO_3$ sample II

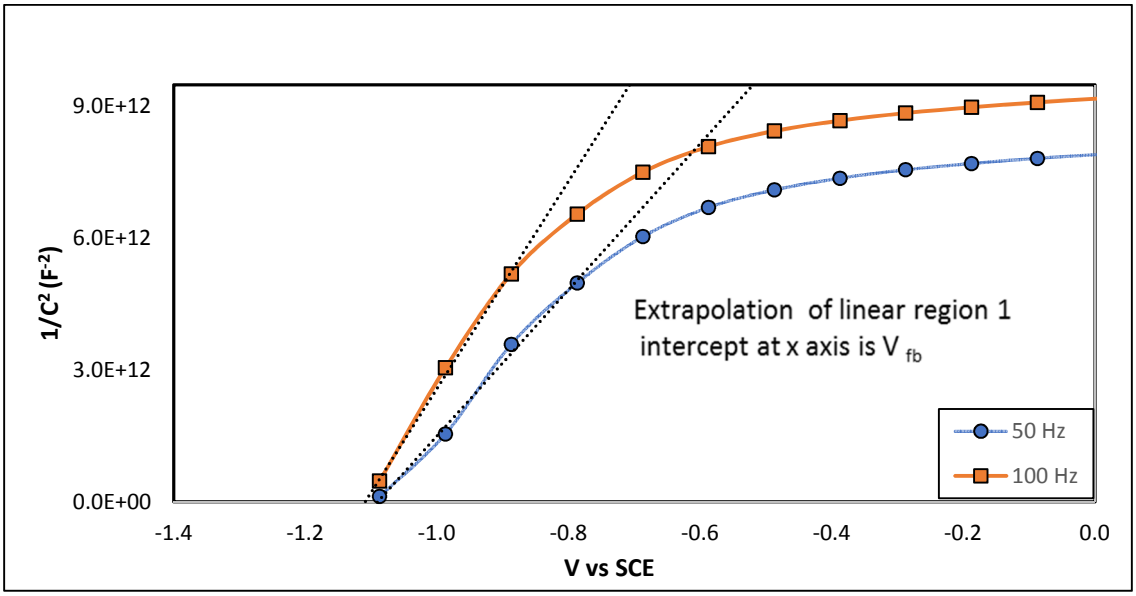

Figure 2.26 (a) Mott Schottky plot for $LaCr_{0.75}Fe_{0.25}O_3$ sample I

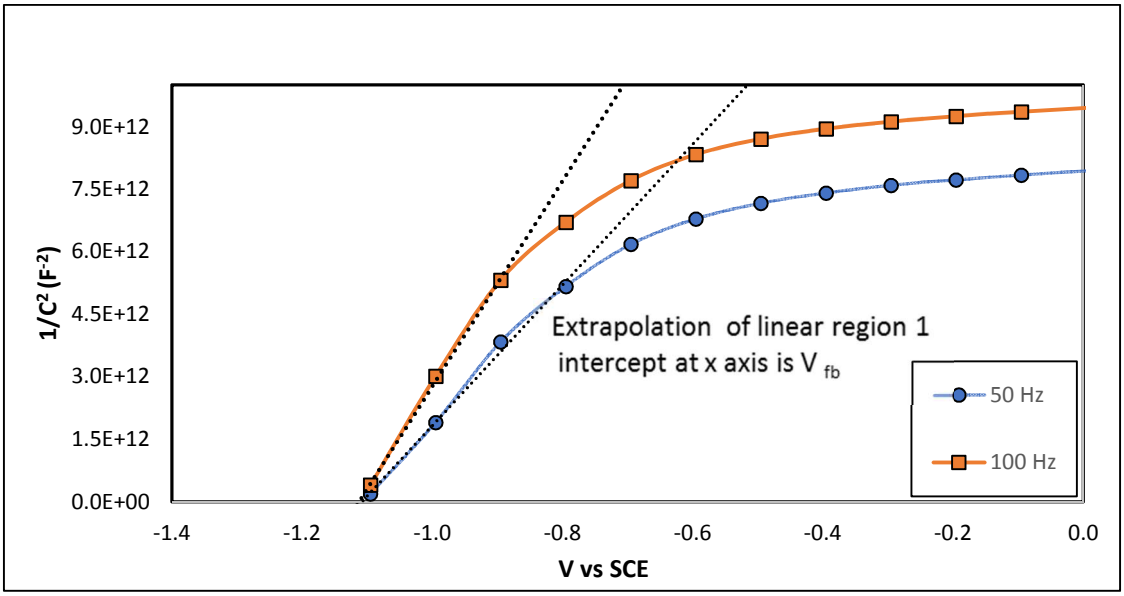

Figure 2.26 (b) Mott Schottky plot for $LaCr_{0.75}Fe_{0.25}O_3$ sample II

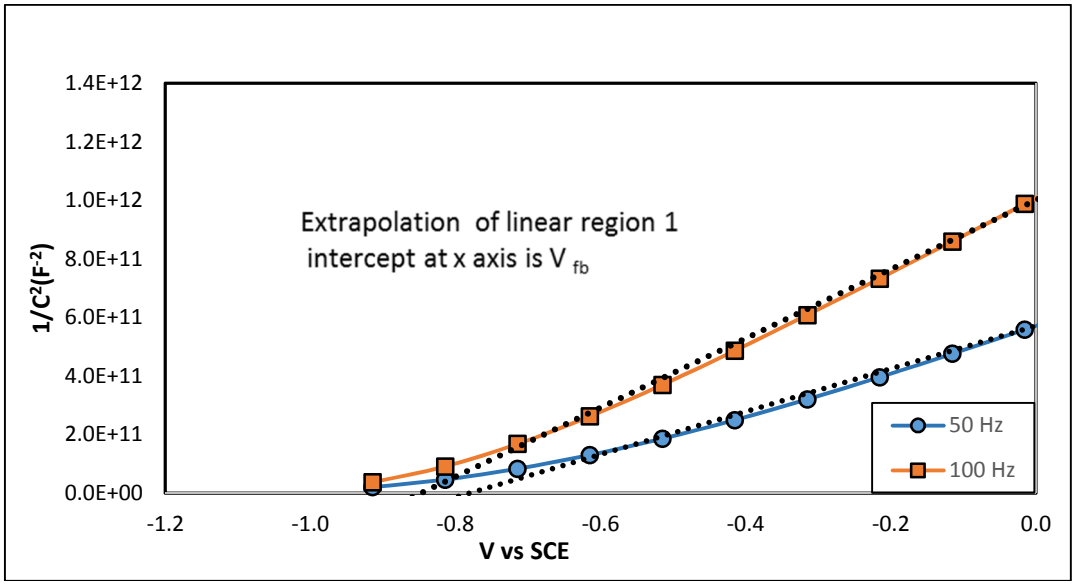

Figure 2.27 Mott Schottky plot for $LaCr_{0.5}Fe_{0.5}O_3$ sample I

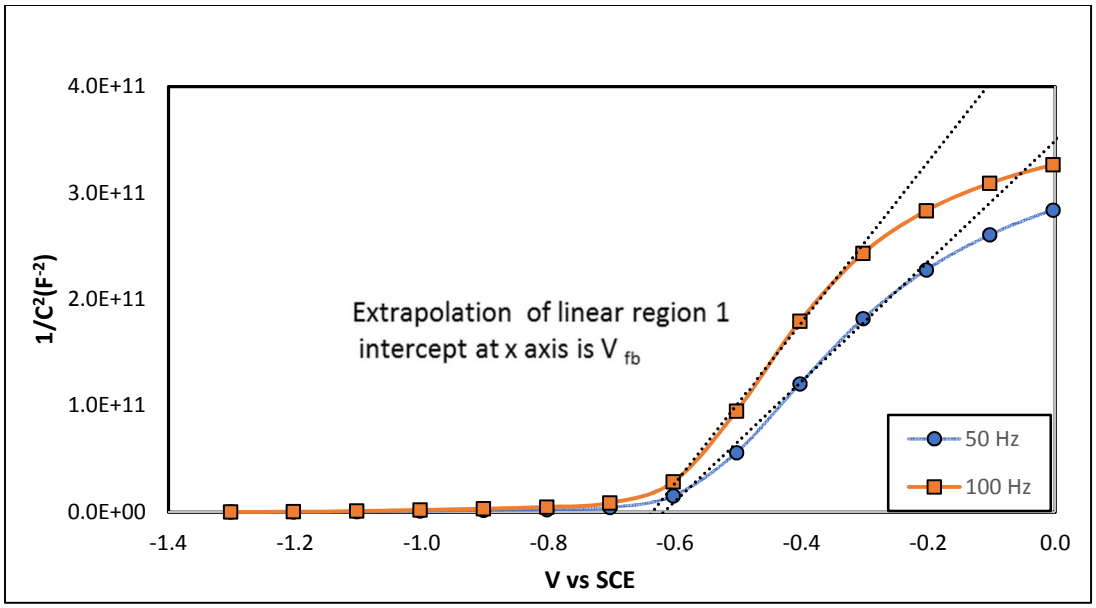

Figure 2.28 (a) Mott Schottky plot for $LaFeO_3$ sample I

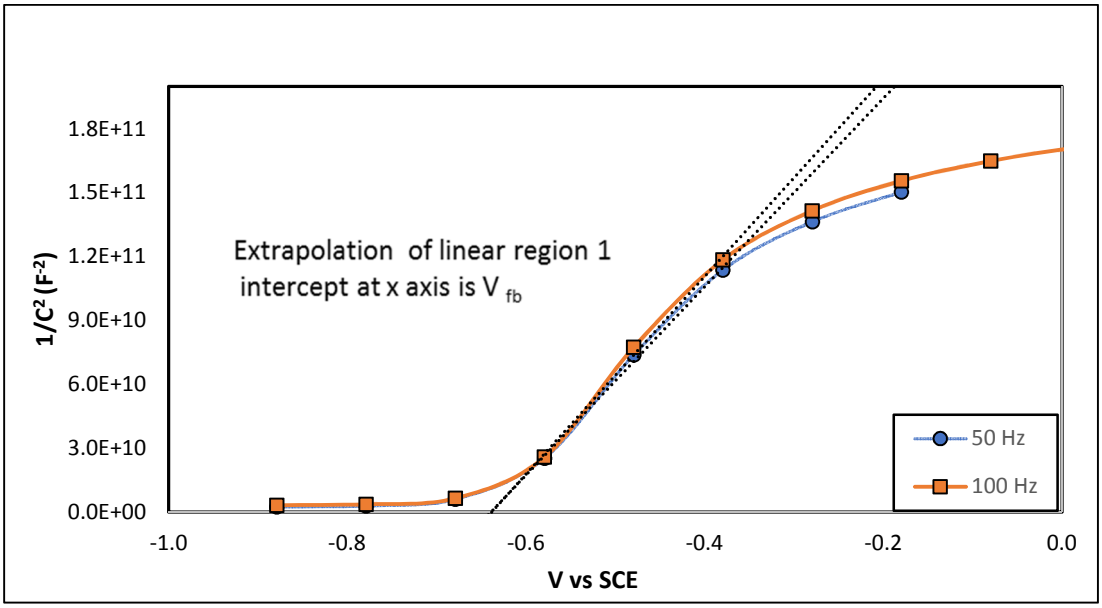

Figure 2.28 (b) Mott Schottky plot for $LaFeO_3$ sample II

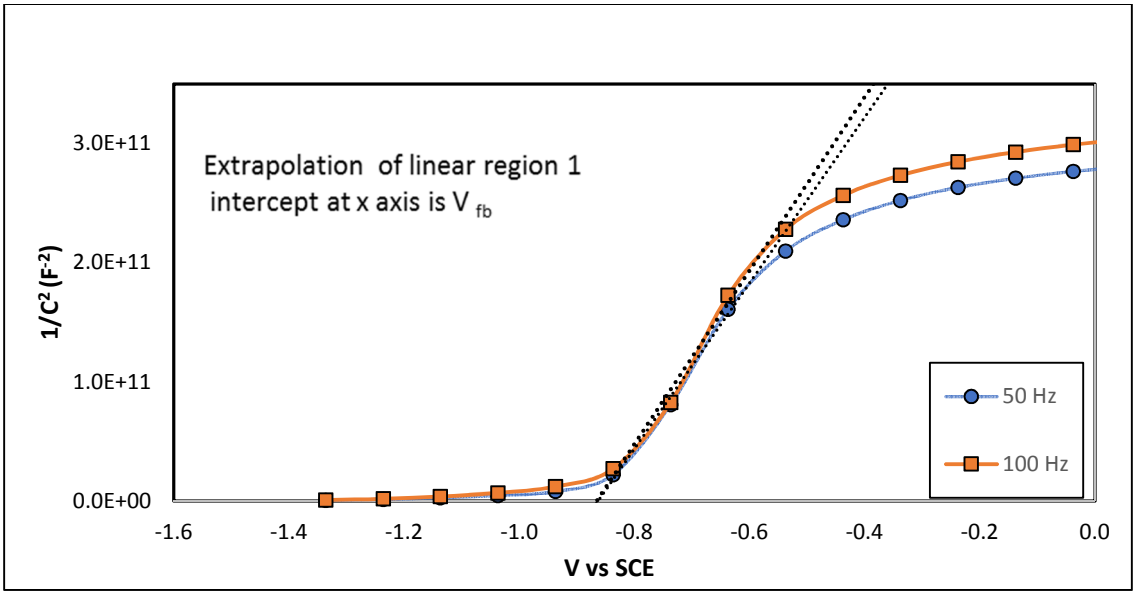

Figure 2.29 Mott Schottky plot for $LaMn_{0.25}Fe_{0.75}O_3$ sample I

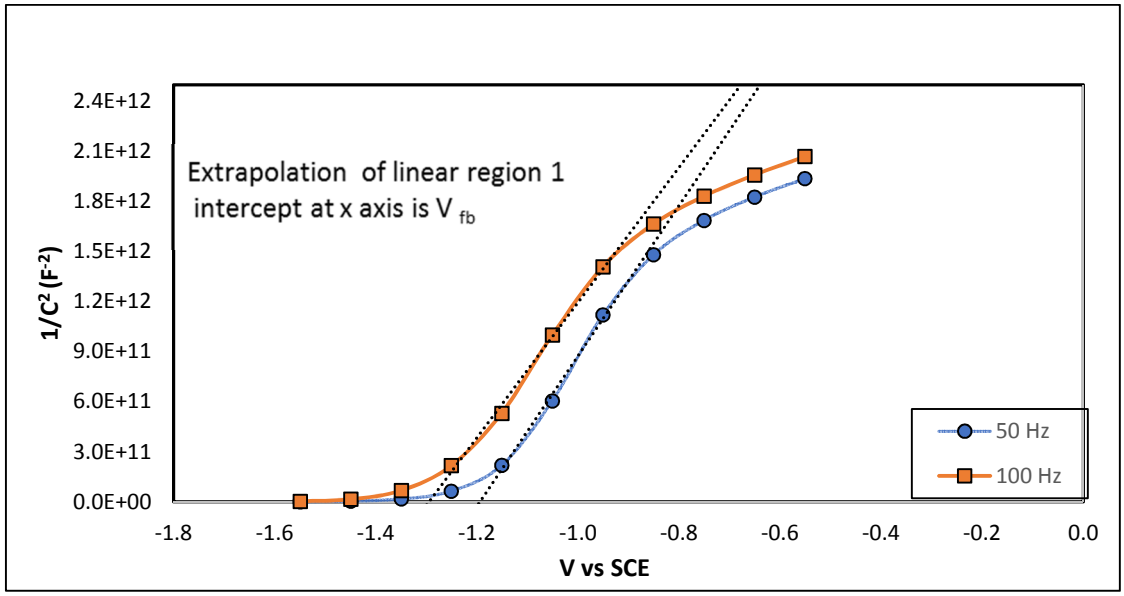

Figure 2.30 (a) Mott Schottky plot for $LaMn_{0.5}Fe_{0.5}O_3$ sample I

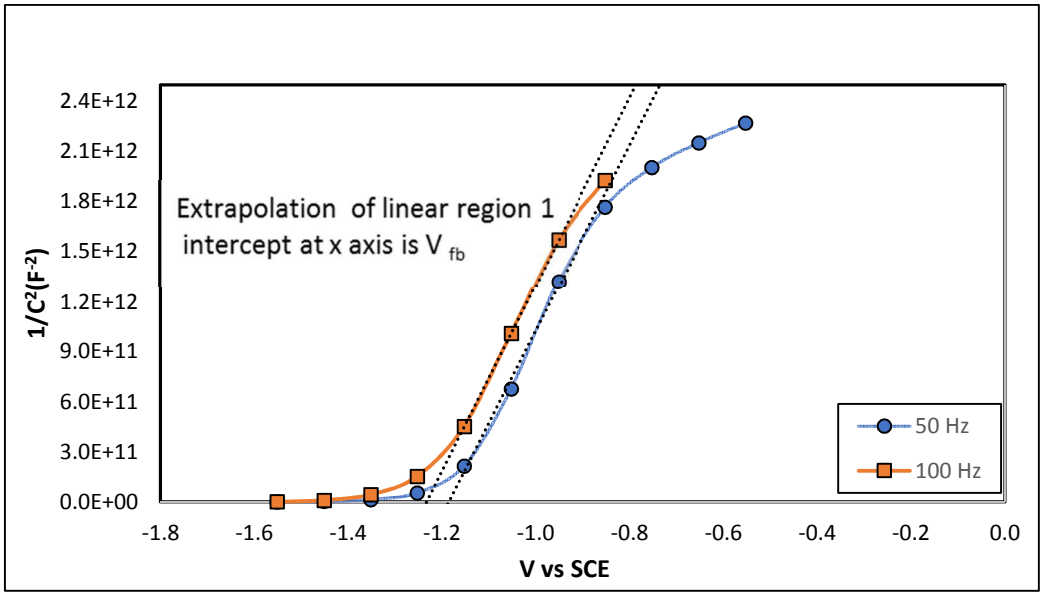

Figure 2.30 (b) Mott Schottky plot for $LaMn_{0.5}Fe_{0.5}O_3$ sample II

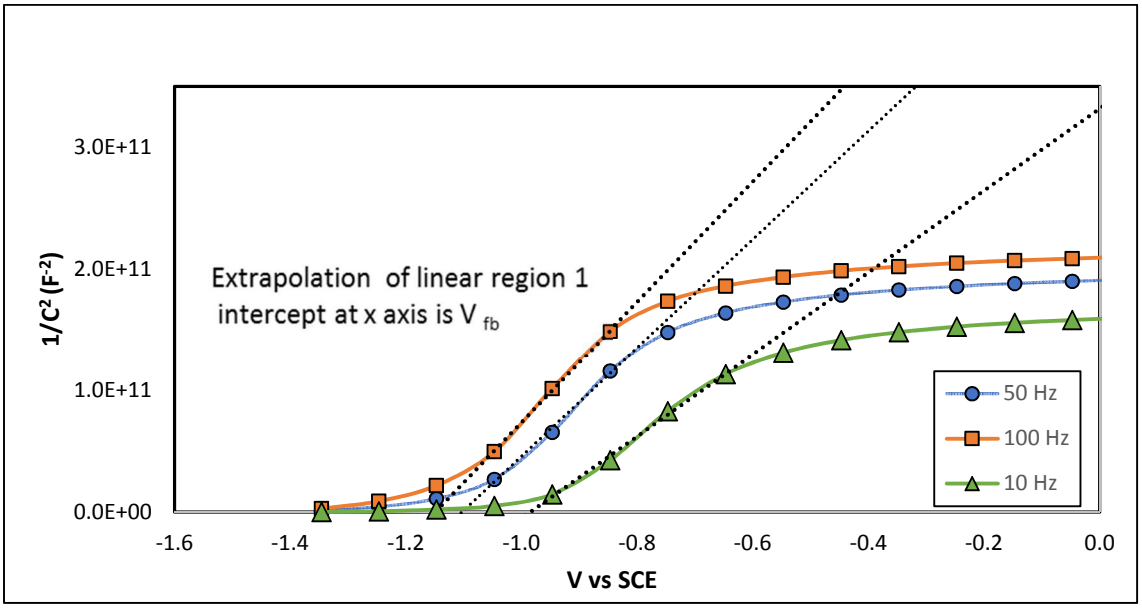

Figure 2.31 (a) Mott Schottky plot for $LaMn_{0.75}Fe_{0.25}O_3$ sample I

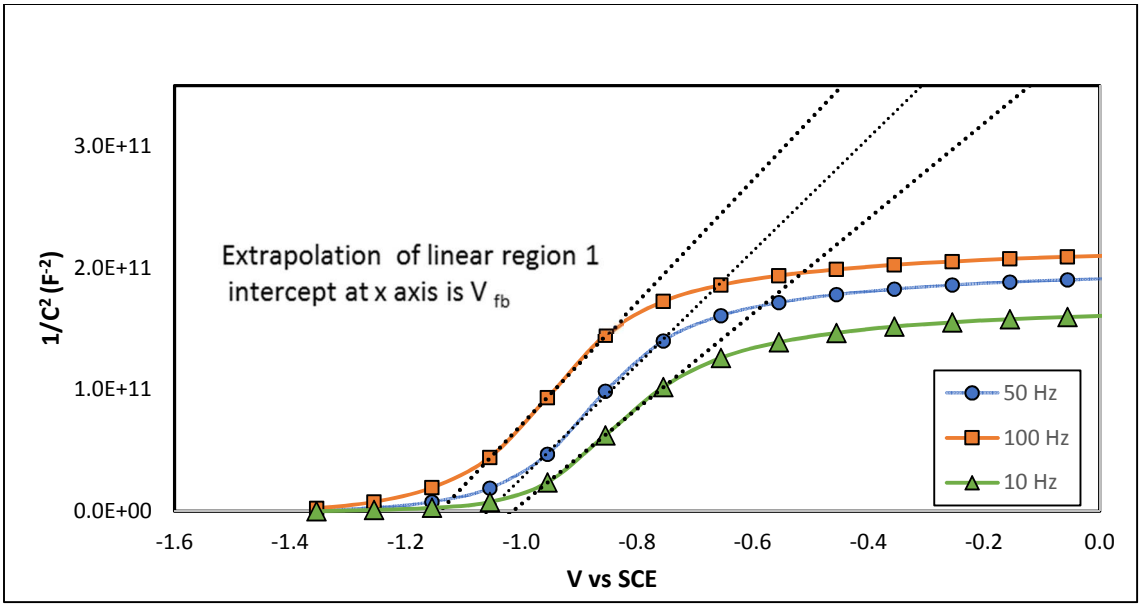

Figure 2.31 (b) Mott Schottky plot for $LaMn_{0.75}Fe_{0.25}O_3$ sample II

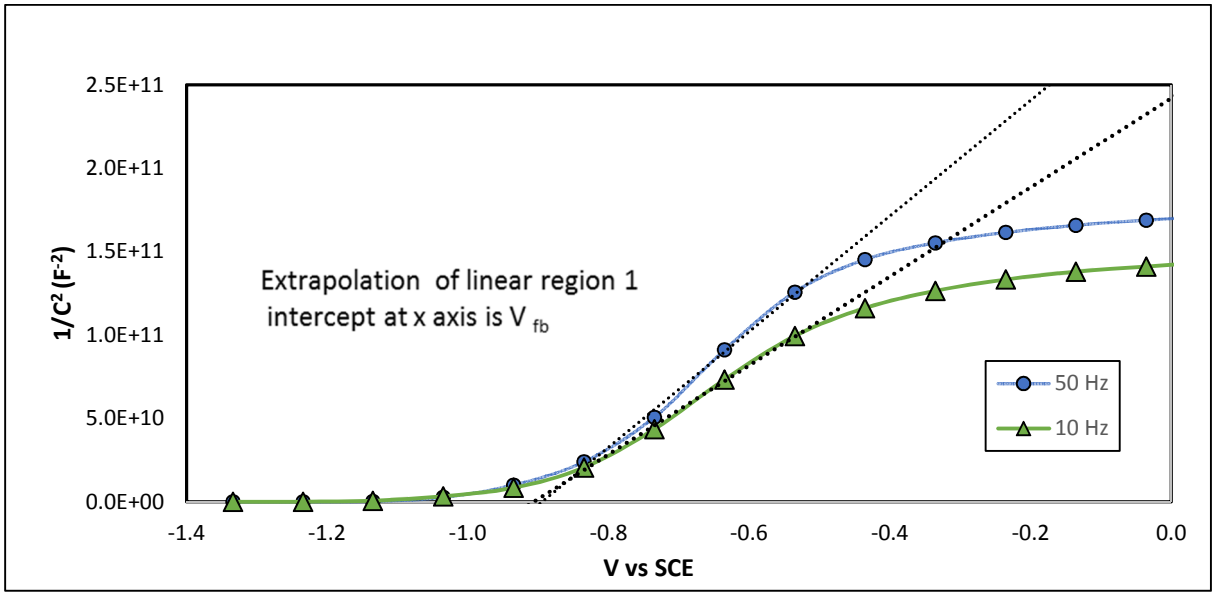

Figure 2.32 (a) Mott Schottky plot for $LaMnO_3$ sample I

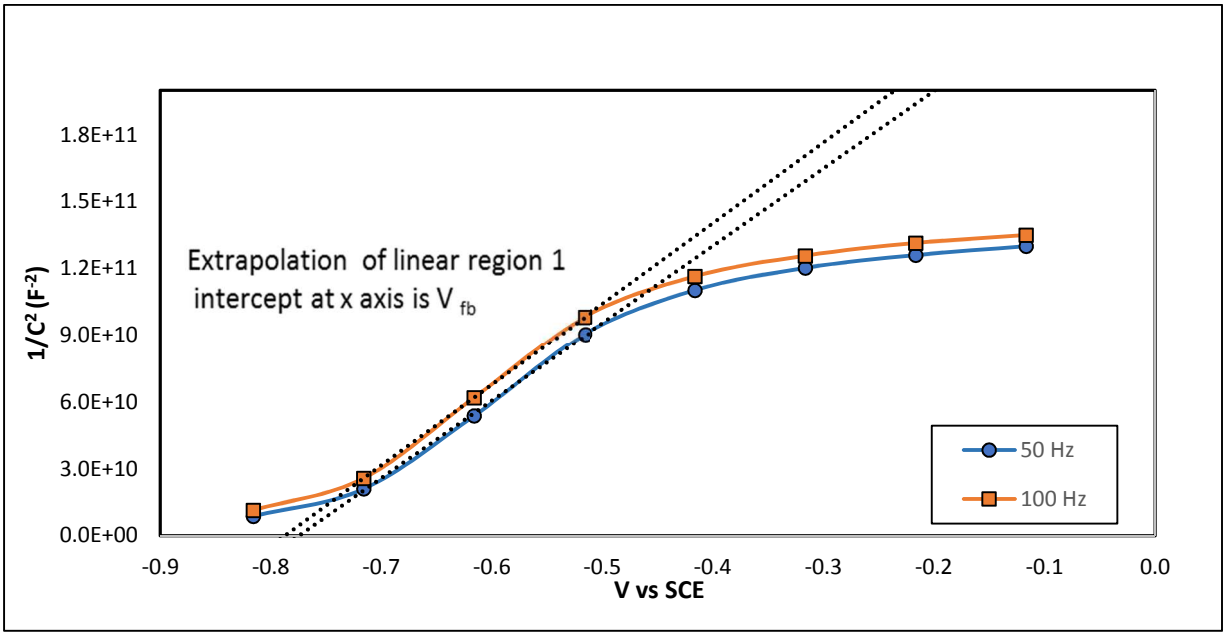

Figure 2.32 (b) Mott Schottky plot for $LaMnO_3$ sample II

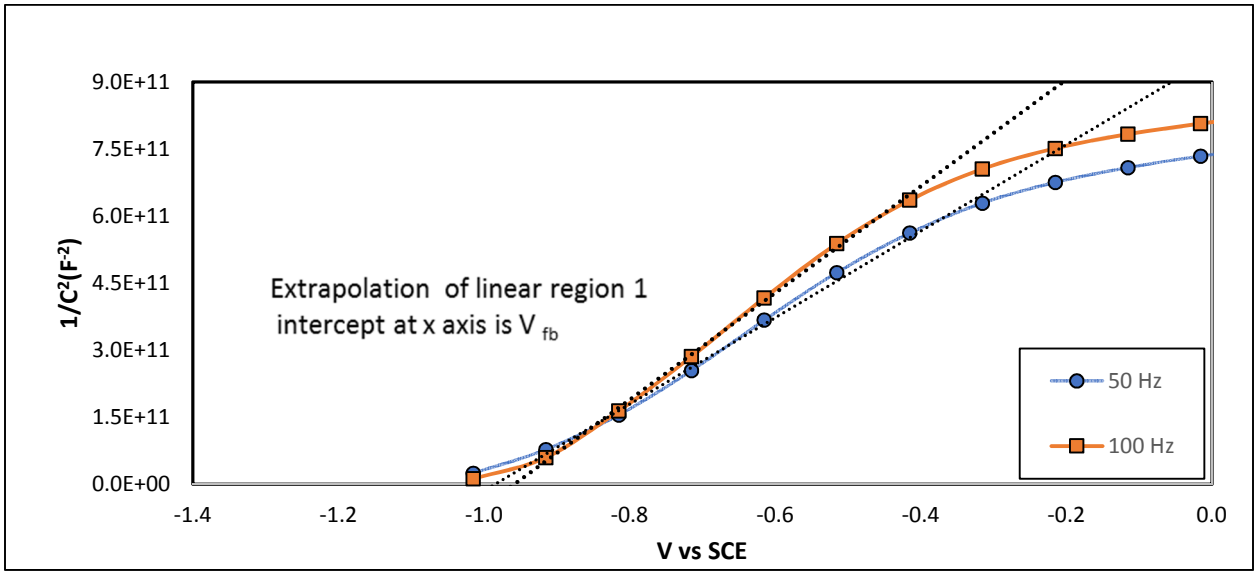

Figure 2.33 (a) Mott Schottky plot for $LaMn_{0.75}Cr_{0.25}O_3$ sample I

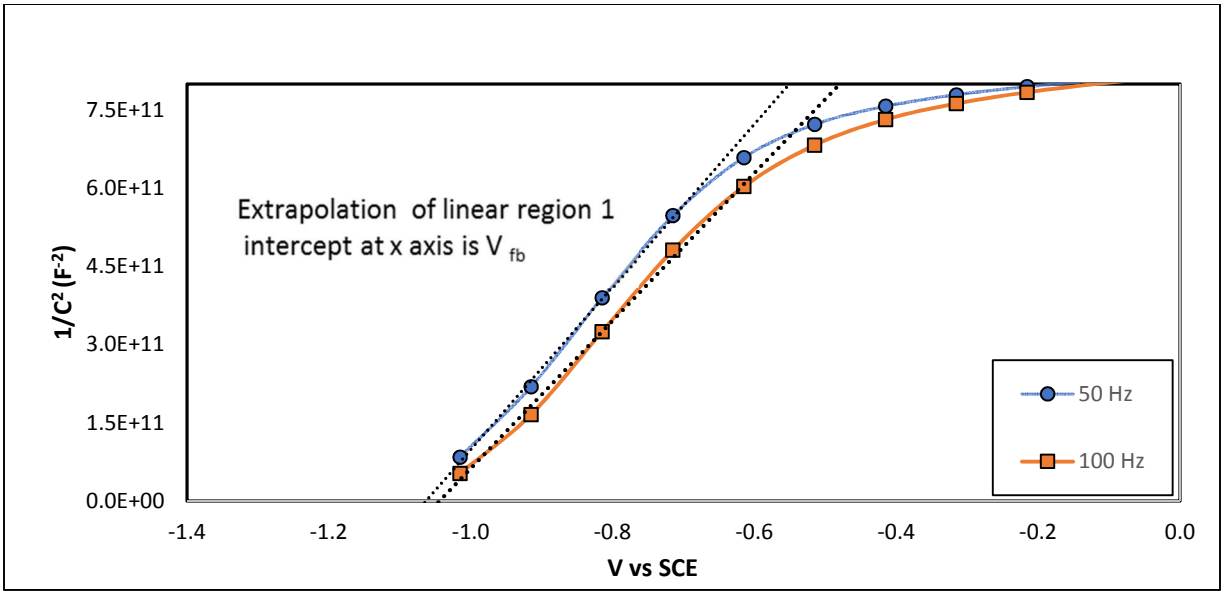

Figure 2.33 (b) Mott Schottky plot for $LaMn_{0.75}Cr_{0.25}O_3$ sample II

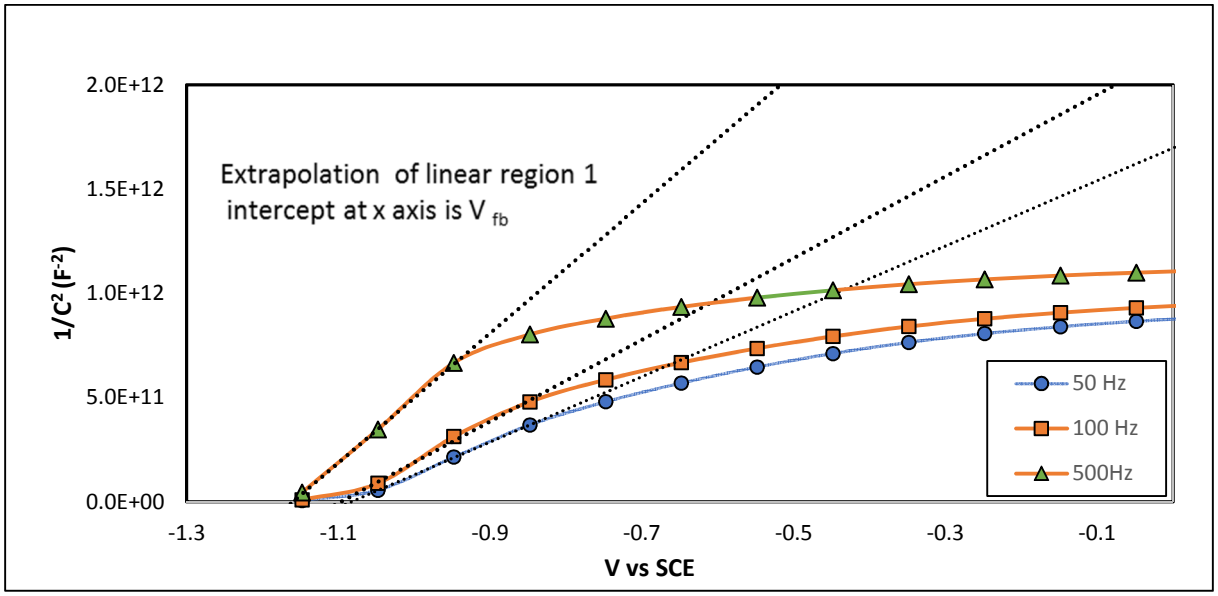

Figure 2.34 (a) Mott Schottky plot for $LaMn_{0.5}Cr_{0.5}O_3$ sample I

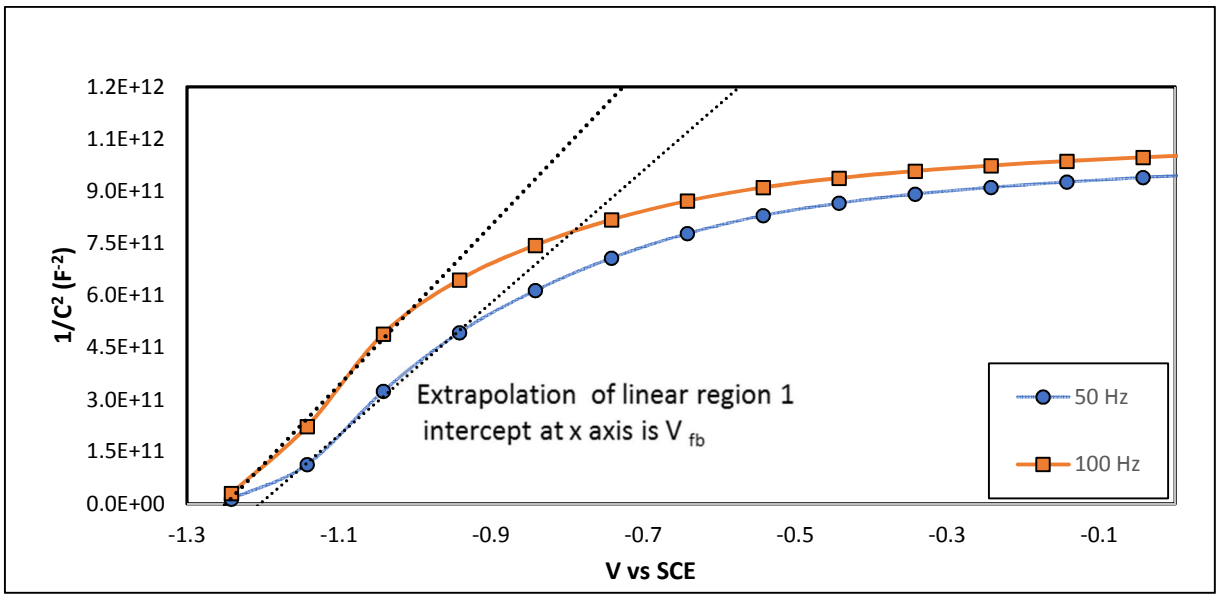

Figure 2.34 (b) Mott Schottky plot for $LaMn_{0.5}Cr_{0.5}O_3$ sample II

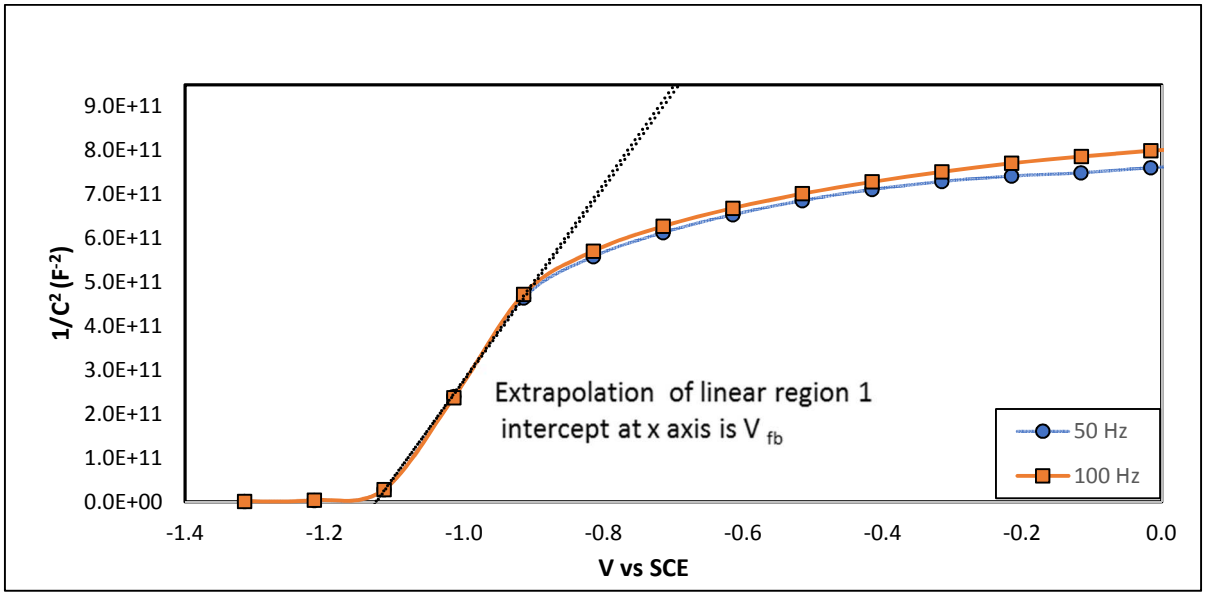

Figure 2.35 (a) Mott Schottky plot for $LaMn_{0.25}Cr_{0.75}O_3$ sample I

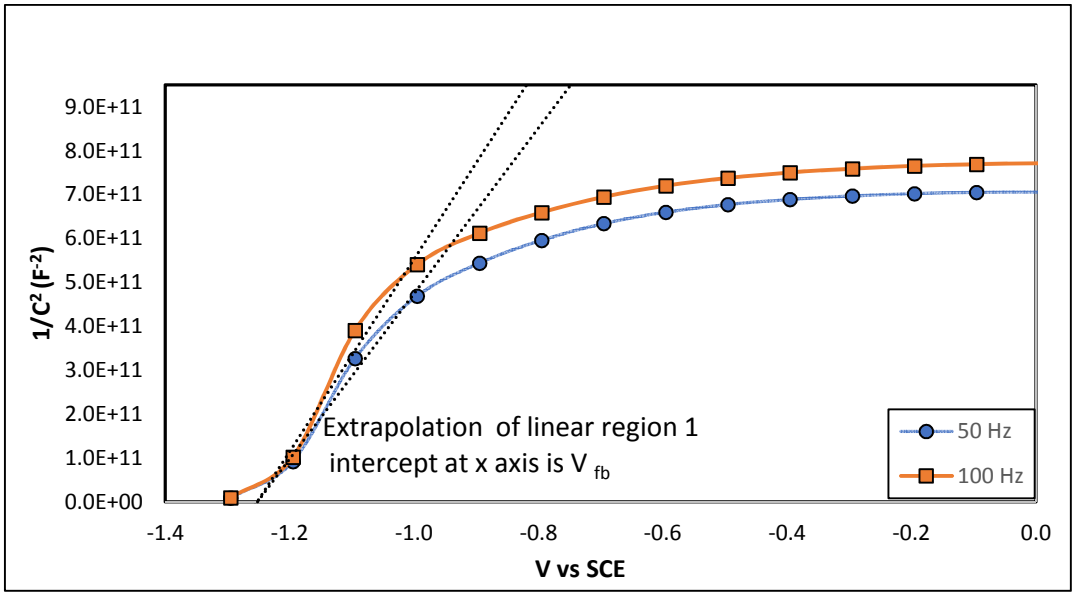

Figure 2.35 (b) Mott Schottky plot for $LaMn_{0.25}Cr_{0.75}O_3$ sample II

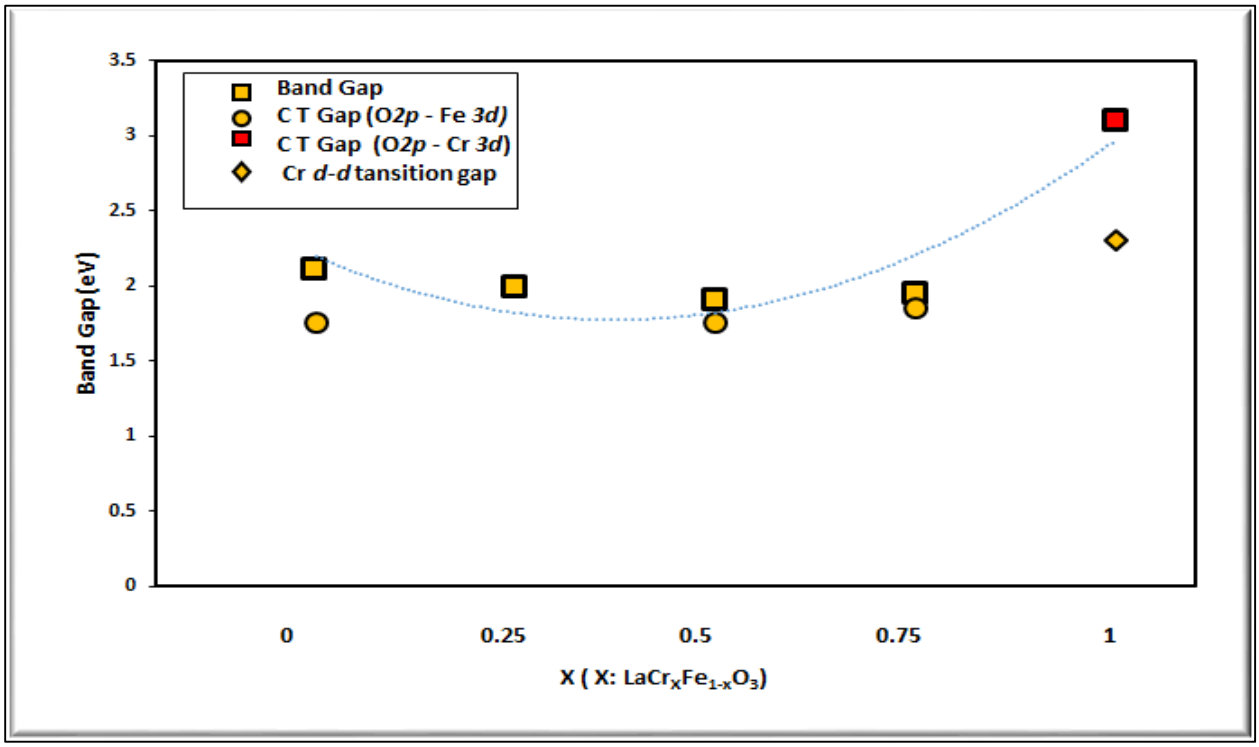

Figure 2.36 Band gap trend in $LaCr_xFe_{1-x}O_3$

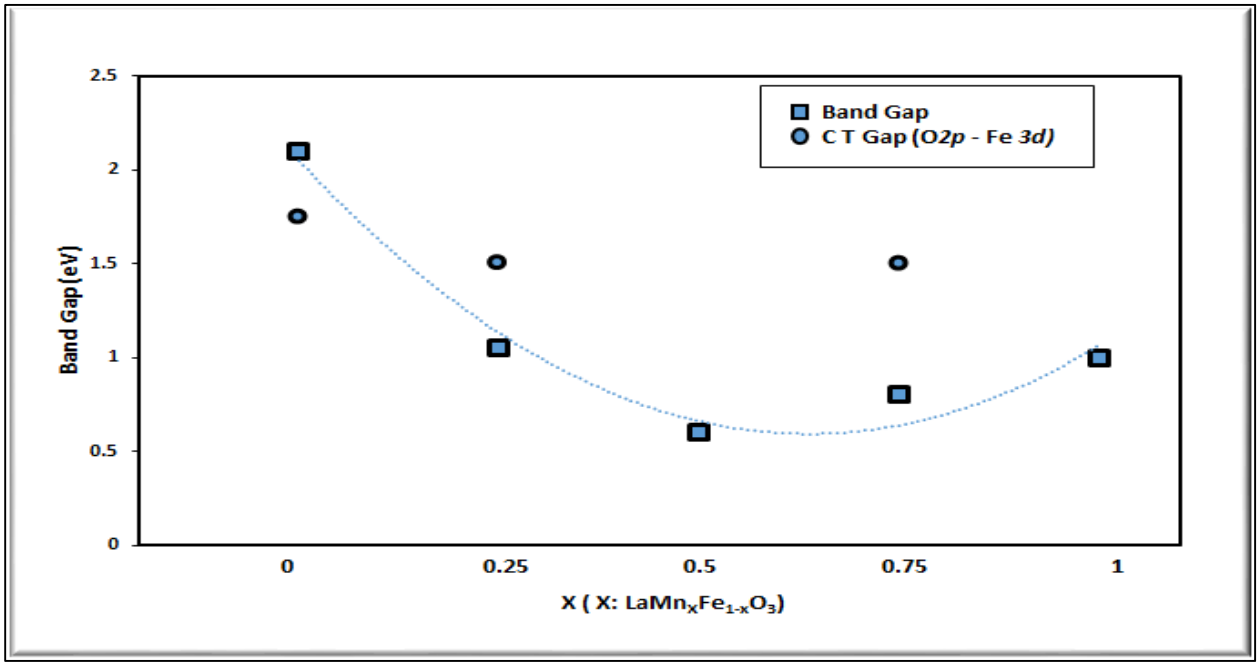

Figure 2.37 Band gap trend in $LaMn_xFe_{1-x}O_3$

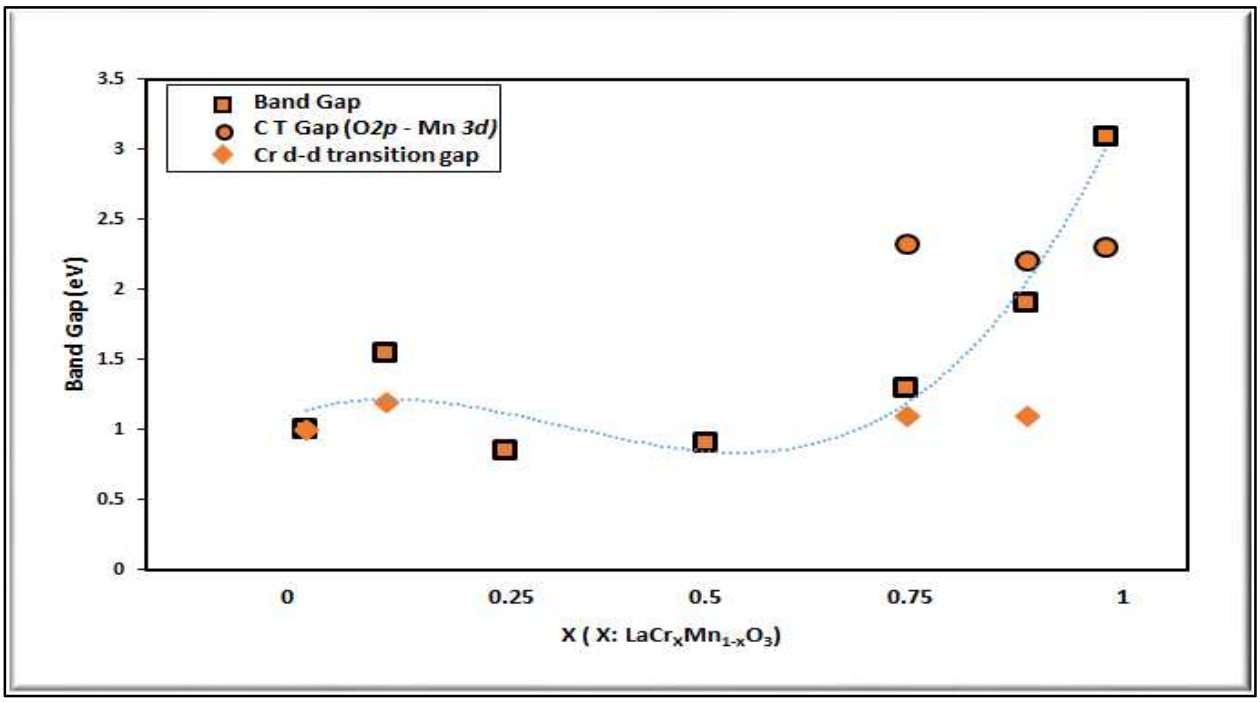

Figure 2.38 Band gap trend in $LaCr_xMn_{1-x}O_3$

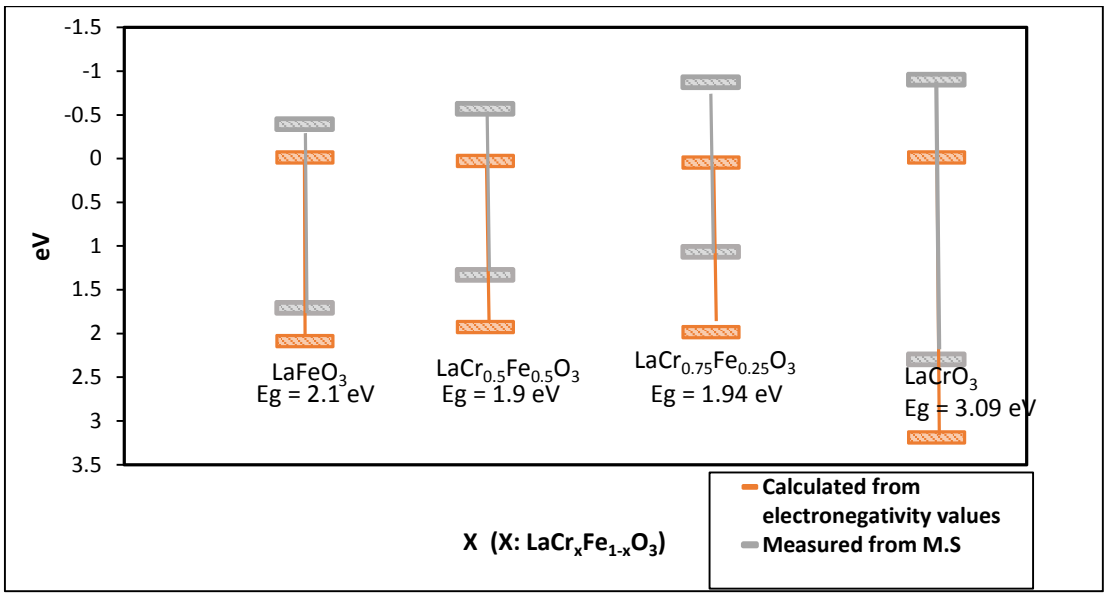

Figure 2.39 Band edge trend of $LaCr_xFe_{1-x}O_3$

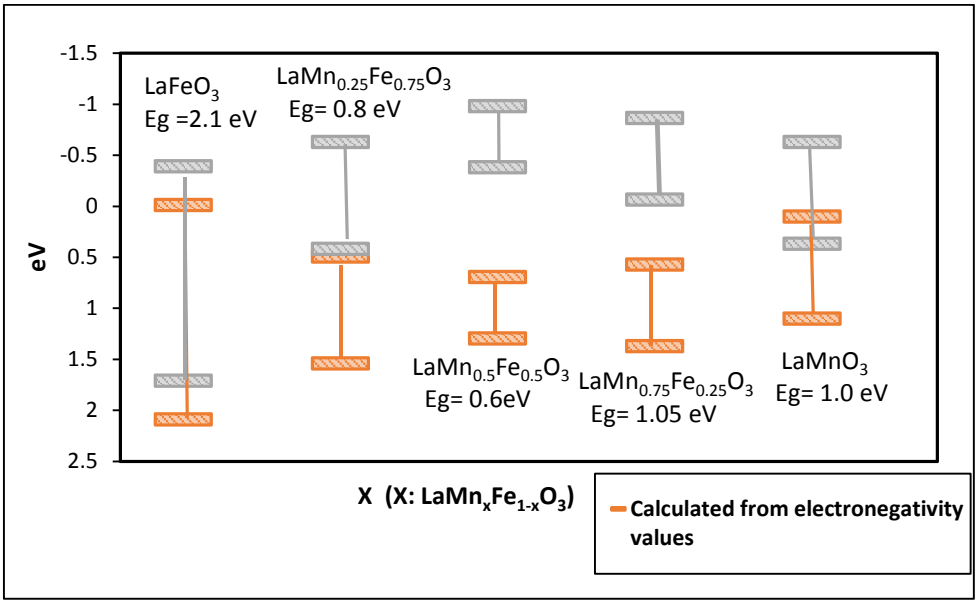

Figure 2.40 Band edge trend of $LaMn_xFe_{1-x}O_3$

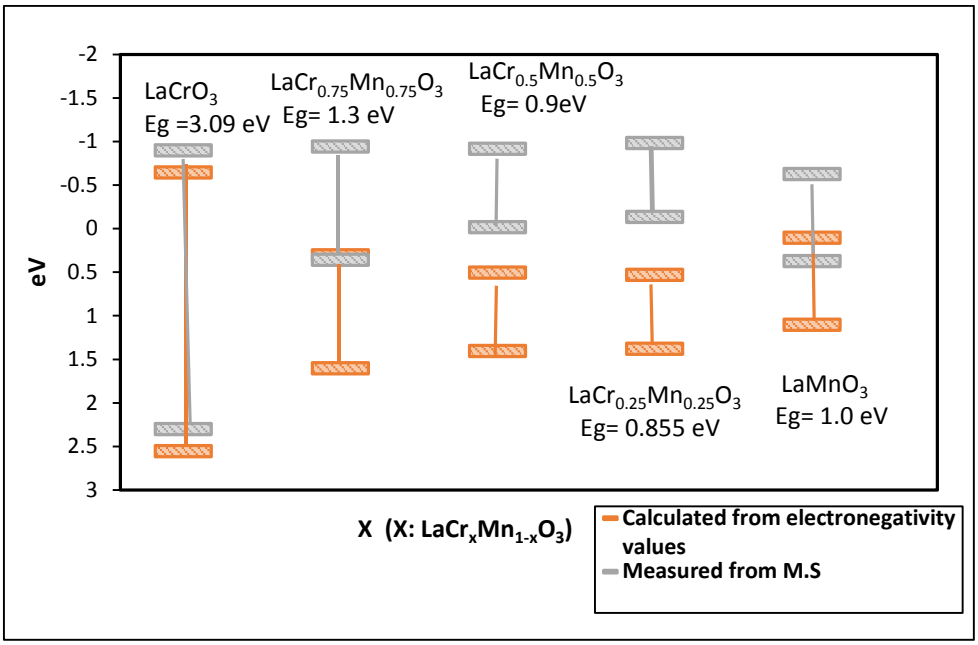

Figure 2.41 Band edge trend of $LaCr_xMn_{1-x}O_3$

CHAPTER 3 - FUTURE WORK

3.1 Photocatalytic Dye Degradation

3.1.1 Introduction

Photo-degradation of organic contaminants has been a keen interest due to current water shortage and pollution. Approximately 40% of the world's population experience water scarcity. Recycling stagnant water bodies polluted with organic and industrial solvents will offer significant relief from our current water crisis. Principle water contaminants are cyclic organic compounds, industrial dyes and bio organic species. A large number of these organic products possess high toxicity and are not fully degraded by the recycling plants. Hence stringent oxidizing agents are required to fully mineralize these compounds into less harmful by-products.

Advanced oxidative technique (AOT) involves the oxidation of organics through photolysis of oxygen or water molecules. AOT relies on the formation of hydroxyl radicals which are considered responsible for the mineralization of the pollutant. The mechanism of hydroxyl radical formation depends on numerous material and environmental properties. Upon illumination by radiation of suitable photon energy, excitation of valence electrons to the conduction energy level results in the electron-hole pair generation. The other possibility is oxidation of contaminant under suitable irradiant source, yielding electrons to the conduction energy level (refer to Fig 3.1). Interaction of these species with the adsorbed water molecule or dissolved oxygen on the surface of

the semiconductor results in the formation of hydroxyl radical which mineralizes the organic into CO_2, H_2O and maybe other simpler carbonaceous compounds.

3.1.2 Experiment

The photocatalytic oxidation reactions were carried out on a slurry type batch reactor (refer to Fig 3.2). The reaction conditions were closely monitored. The experiment set up consists of a magnetic stirrer to allow for even distribution of light on the reactants. The light fixtures were General Electric F8T5/D florescent bulbs with daylight spectrum and a color rendering index of 75. Each bulb contributed a power of 8 W. Initially experiments were conducted under 48 W illumination and later increased to 88 W. Leakage was prevented by conducting the experiments in the enclosed reactor. The duration of the experiment was 90 minutes. Degradation rates were determined by measuring the absorbance of the pollutant in 1 ml aliquot taken every 15 minutes. Care was taken not to expose these intermittent samples measurements to light. The absorbance measurements were carried out in Perkin Elmer Lambda 35 UV- Vis spectrophotometer with a scan speed of 1 nm/s in the range of 450 to 600 nm.

3.1.3 Preliminary Results and Discussions

4,5,6,7-tetrachloro-2',4',5',7'-tetraiodofluorescein, commonly known as Rose Bengal is chosen as the model contaminant for the photo degradation experiments. The reaction volume consists of 5% Rose Bengal and 95% deionized water. The catalyst loading was varied from 2.6×10^{-4} g/ml to 10^{-3}g/ml of $LaFe_{0.5}Cr_{0.5}O_3$. The pH of the initial reaction solution was in the order of ~ 6. The initial concentration of R.B 0.0169mM. Other preliminary investigation on the effect of illumination intensity was also carried

out. No significant enhancement in the degradation rate was noticed with changes in experiment parameters.

The reaction rates were influenced by the following factors. Since the photodegradation reaction occurs at the interface of the pollutant and photocatalyst, adsorption of the contaminant on the catalysts will greatly increase the rate of the reaction. Larger surface area of photocatalyst enhances the absorption[65]. The relationship between the pH of the environment and the surface charge governs the type of dye species that will be adsorbed better on the catalyst surface. At pH< point of zero charge the surface is positively charged and cationic dyes are weakly adsorbed at these conditions [66] but as Rose Bengal is an organic dye, surface adsorption plays a more dominant than pH of the reaction. Hence reaction rates can be improved through increase of the catalyst surface area.

Although the band structure of prepared perovskites favor degradation ofRose Bengal (refer to Fig 3.6), the large electron-hole recombination rates maybe a possible reason for slow degradation rates.

Another possible reason for slow degradation rates is because of the oxidation of transition metal species (Fig 3.7).as seen in hole induced photo degradation due to Co^{+3} reduction in $LaCoO_3$ explains the slow degradation rates seen in this species[66]. Further study into extinction factor and electron-hole recombination rates of the prepared perovskites is necessary to explain the results obtained.

3.2 Photocatalytic CO_2 Reduction

CO_2 is a highly stable pollutant and is present in abundance in the Earth's atmosphere. Hydrogenation of carbon dioxide to hydrocarbon fuels will prove most beneficial, but reduction of CO_2 is not favored because a large negative potential(E= -1.97 V vs NHE) required for even an electron reduction of CO_2, also reaction limitations due to structural dissimilarity of CO_2 and CO_2 will raise the energy requirements higher[67]. Lesser energy pathways are possible for CO_2 reduction and they involve multiple electron transfer-proton assisted reduction reactions and result in the formation of hydrocarbon by-products. Thus a method of artificial photosynthesis can be devised for harvesting solar energy through a semiconductor photocatalyst to reduce CO_2.

The process of photocatalytic CO_2 involves generation of electron/holes charge carriers through excitation of valence electrons of appropriate photon energy. On creation these charge carriers travel across energy barriers through the semiconductor and react at the surface with the adsorbed CO_2 molecules. Recombination rates of the charge carriers has to be low to enable reduction reactions to occur [67-69]. Some over potential is needed to for the CO_2 reduction to take place. To satisfy this condition, the excited valence electron must be at a more negative potential than the CO_2 reduction potentials. For water oxidation, the holes have to be at a more positive potential than the reduction potential of H_2O/O_2. The following reactions can take place during photocatalytic CO_2, their reduction potentials are also mentioned at pH=7 conditions[70]

$CO_2/*CO_2 \rightarrow E^O = -1.9$ V vs NHE

$CO_2/*CH_3OH \rightarrow E^O = -0.38$ V vs NHE

$CO_2/HCOOH \rightarrow E^O = -0.61$ V vs NHE

$CO_2/CH_4 \rightarrow E^O = -0.24$ V vs NHE

$CO_2/CO \rightarrow E^O = -0.53$ V vs NHE $\qquad$ $H_2O/O_2 \rightarrow E^O = +0.81$V vs NHE

$CO_2/HCO \rightarrow E^O = -0.48$ V vs NHE $\qquad$ $H^+/H_2 \rightarrow E^O = -0.42$V vs NHE

Based on the above information and data of the conduction and valence band edges of the perovskites obtained from M.S measurements, possible candidates for CO_2 reduction and H_2O oxidation can be determined (refer to Table 3.1). Although these perovskites provide a good over potential, surface properties and charge carrier recombination rates are to be investigated to confirm the reaction's feasibility. Future efforts for CO_2 reduction using the synthesized catalysts are in progress

Table 3.1 Possible candidates for photocatalytic CO_2 and water oxidation

Perovskite	CO_2/CH_4	H^+/H_2	CO_2/CO	$CO_2/HCOOH$	CO_2/CH_3OH	$H_2O/O2$	$CO_2/HCHO$
$LaCrO_3$	✓	✓	✓	✓	✓	✓	✓
$LaCr_{0.75}Mn_{0.25}O_3$	✓	✓	✓	✓	✓	×	✓
$LaCr_{0.5}Mn_{0.5}O_3$	✓	✓	✓	✓	✓	×	✓
$LaCr_{0.25}Mn_{0.75}O_3$	✓	✓	✓	✓	✓	×	✓
$LaMnO_3$	✓	✓	✓	✓	✓	×	✓
$LaCr_{0.75}Fe_{0.25}O_3$	✓	✓	✓	✓	✓	✓	✓
$LaCr_{0.5}Fe_{0.5}O_3$	✓	✓	×	×	✓	✓	✓
$LaFeO_3$	✓	×	×	×	✓	✓	×
$LaMn_{0.75}Fe_{0.25}O_3$	✓	✓	✓	✓	✓	×	✓
$LaMn_{0.5}Fe_{0.5}O_3$	✓	✓	✓	✓	✓	×	✓
$LaMn_{0.25}Fe_{0.75}O_3$	✓	✓	✓	×	✓	✓	✓

✓- feasible, ×-not feasible

.

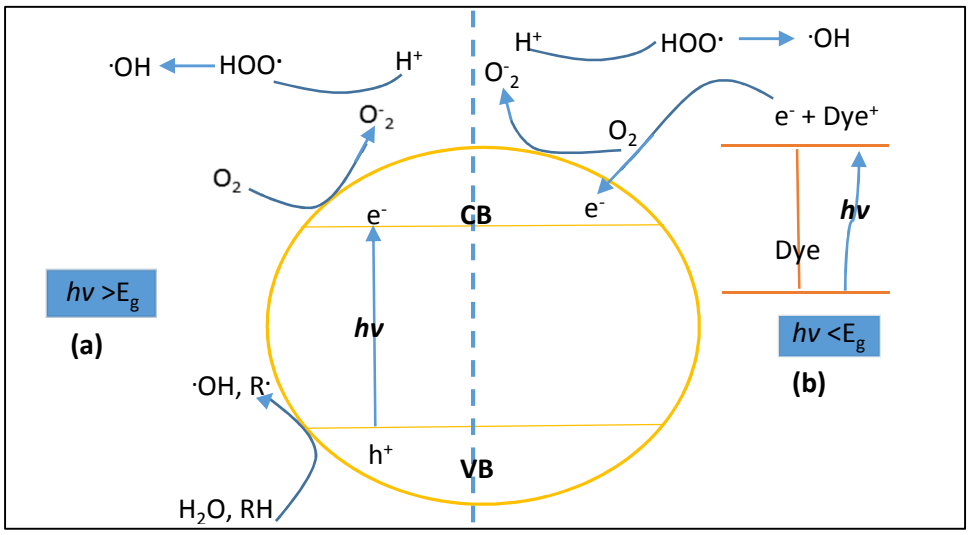

Figure 3.1 Formation of hydroxyl radical when**: (a)** For hv >E_g **(b)** For hv <E_g

Figure 3.2 Batch reactor; outside view (right), inside view (left)

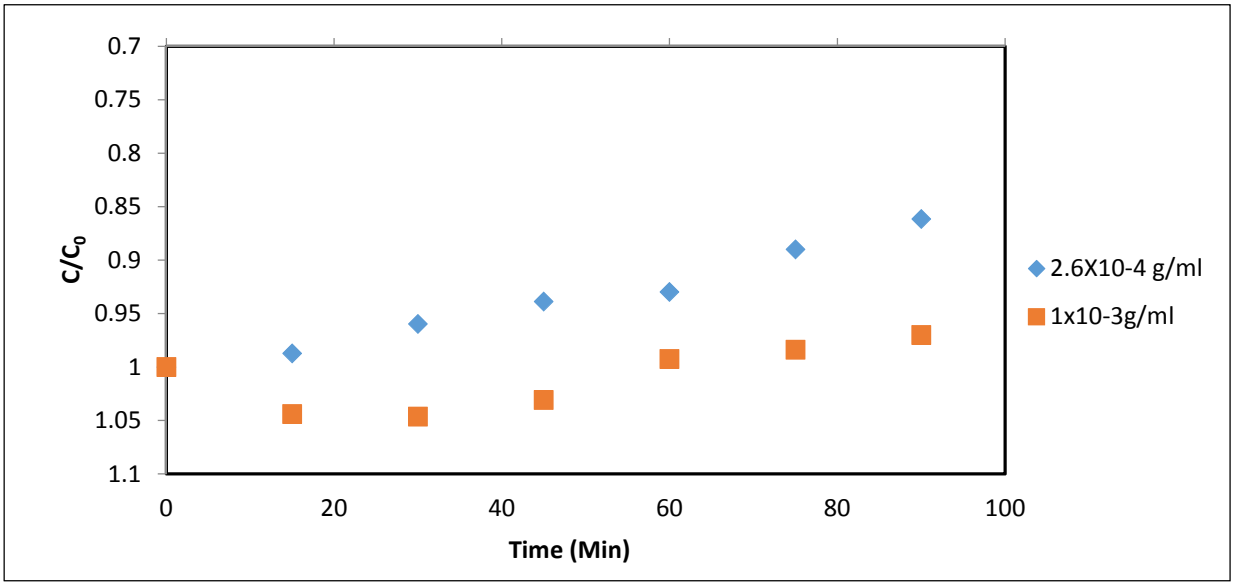

Figure 3.3 Degradation rate for different $LaCr_{0.5}Fe_{0.5}O_3$ loading under illumination 48W

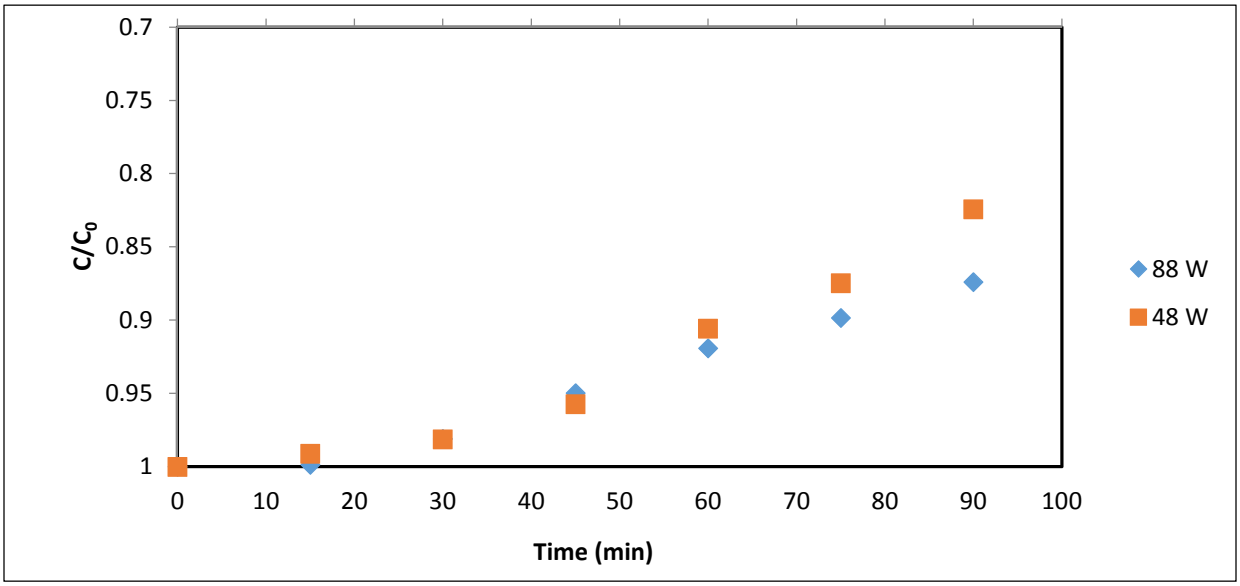

Figure 3.4 Degradation rate for same $LaCr_{0.9}Mn_{0.1}O_3$ loading $1x10^{-3}$g/ml

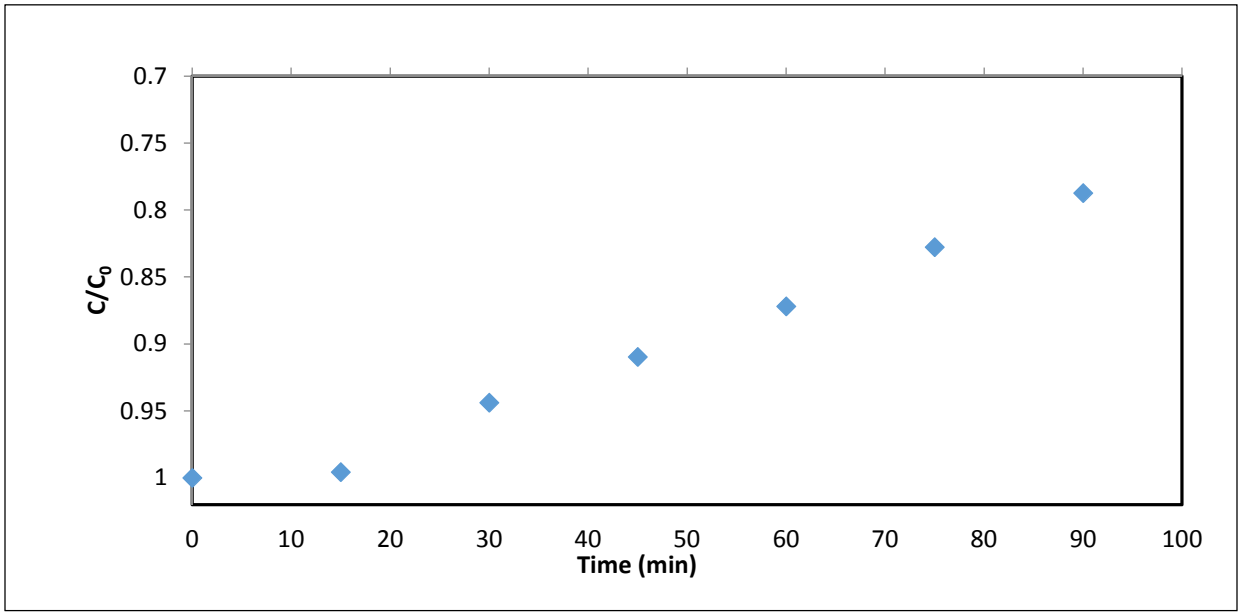

Figure 3.5 Degradation rate for $LaMn_{0.5}Fe_{0.5}O_3$ $1x10^{-3}$g/ml loading under illumination 88W

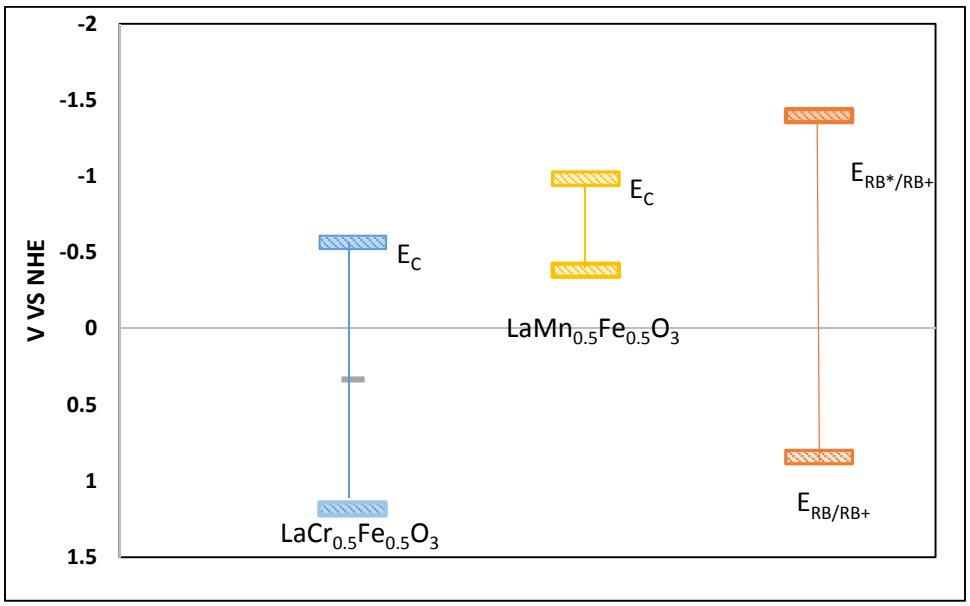

Figure 3.6 Electronic structure of catalysts and dye

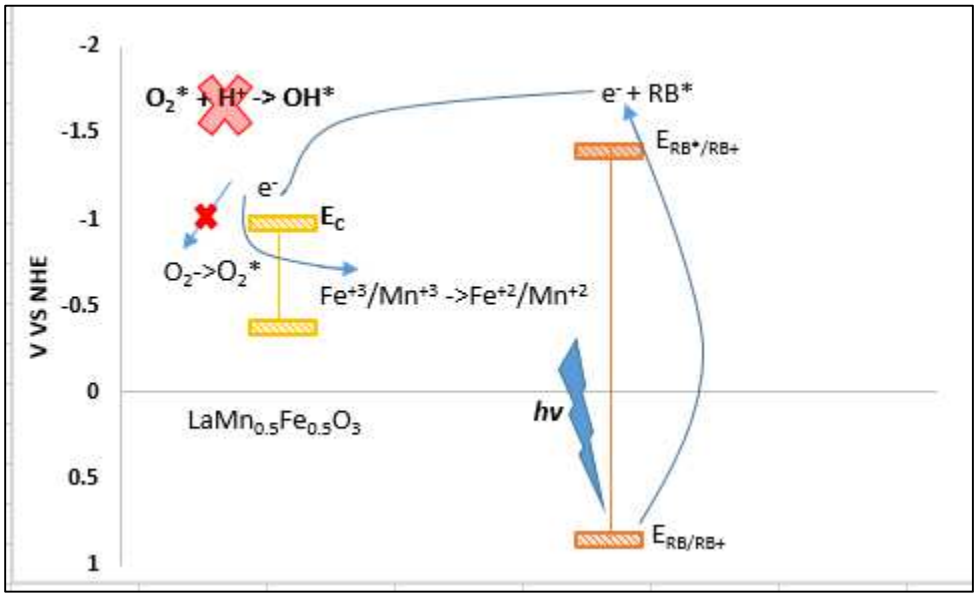

Figure 3.7 Possible mechanism that inhibits photo degradation

REFERENCES

1. Maeda, K., *Photocatalytic water splitting using semiconductor particles: history and recent developments.* Journal of Photochemistry and Photobiology C: Photochemistry Reviews, 2011. **12**(4): p. 237-268.

2. Izumi, Y., *Recent advances in the photocatalytic conversion of carbon dioxide to fuels with water and/or hydrogen using solar energy and beyond.* Coordination Chemistry Reviews, 2013. **257**(1): p. 171-186.

3. Tahir, B., M. Tahir, and N.S. Amin, *Performance analysis of monolith photoreactor for CO 2 reduction with H 2.* Energy Conversion and Management, 2015. **90**: p. 272-281.

4. Osterloh, F.E., *Inorganic nanostructures for photoelectrochemical and photocatalytic water splitting.* Chemical Society Reviews, 2013. **42**(6): p. 2294-2320.

5. Dalrymple, Omatoyo K., Elias Stefanakos, Maya A. Trotz, and D. Yogi Goswami., *A review of the mechanisms and modeling of photocatalytic disinfection.* Applied Catalysis B: Environmental, 2010. **98**(1): p. 27-38.

6. Lasek, J., Y.-H. Yu, and J.C. Wu, *Removal of NO x by photocatalytic processes.* Journal of Photochemistry and Photobiology C: Photochemistry Reviews, 2013. **14**: p. 29-52.

7. Wang, H, Zhongbiao Wu, Weirong Zhao, and Baohong Guan., *Photocatalytic oxidation of nitrogen oxides using TiO 2 loading on woven glass fabric.* Chemosphere, 2007. **66**(1): p. 185-190.

8. Fujishima, A. and K. Honda, *Electrochemical evidence for the mechanism of the primary stage of photosynthesis.* Bulletin of the chemical society of Japan, 1971. **44**(4): p. 1148-1150.

9. Stine, W.B. and M. Geyer, *Power from the Sun*. 2001, Power from the sun. net.

10. Moore, C.E., M.G.J. Minnaert, and J. Houtgast, *The solar spectrum 2935 A to 8770 A.* National Bureau of Standards Monograph, Washington: US Government Printing Office (USGPO), 1966, 1966. **1**.

11. Hulstrom, R., R. Bird, and C. Riordan, *Spectral solar irradiance data sets for selected terrestrial conditions.* Solar Cells, 1985. **15**(4): p. 365-391.

12. Pena, M. and J. Fierro, *Chemical structures and performance of perovskite oxides.* Chemical Reviews, 2001. **101**(7): p. 1981-2018.

13. de Boer, J.H. and E.J. Verwey, *Semi-conductors with partially and with completely filled 3d-lattice bands.* Proceedings of the Physical Society, 1937. **49**(4S): p. 59.

14. Brandow, B.H., *Theory of mott insulators.* International Journal of Quantum Chemistry, 1976. **10**(S10): p. 417-434.

15. Mott, N. and R. Peierls, *Discussion of the paper by de Boer and Verwey.* Proceedings of the Physical Society, 1937. **49**(4S): p. 72.

16. Hubbard, J. *PROC R SOC LONDON*. in *Proc. R. Soc. London*. 1964.

17. Duan, F. and J. Guojun, *Introduction to condensed matter physics*. Vol. 109. 2005: World Scientific.

18. Fujimori, A., F. Minami, and S. Sugano, *Multielectron satellites and spin polarization in photoemission from Ni compounds.* Physical Review B, 1984. **29**(9): p. 5225.

19. Zaanen, J., G. Sawatzky, and J. Allen, *Band gaps and electronic structure of transition-metal compounds.* Physical Review Letters, 1985. **55**(4): p. 418.

20. Greiner, M.T. and Z.-H. Lu, *Thin-film metal oxides in organic semiconductor devices: their electronic structures, work functions and interfaces.* NPG Asia Materials, 2013. **5**(7): p. e55.

21. Gaki, A., O. Anagnostaki, D. Kioupis, T. Perraki, D. Gakis, and G. Kakali., *Optimization of LaMO 3 (M: Mn, Co, Fe) synthesis through the polymeric precursor route.* Journal of Alloys and Compounds, 2008. **451**(1): p. 305-308.

22. Liqiang, Jing, Sun Xiaojun, Xin Baifu, Wang Baiqi, Cai Weimin, and Fu Honggang, *The preparation and characterization of La doped TiO 2 nanoparticles and their photocatalytic activity.* Journal of Solid State Chemistry, 2004. **177**(10): p. 3375-3382.

23. Kojima, Toshikatsu, Katsuhiro Nomura, Yoshinori Miyazaki, and Kazumi Tanimoto, *Synthesis of various LaMO3 perovskites in molten carbonates.* Journal of the American Ceramic Society, 2006. **89**(12): p. 3610-3616.

24. Prado-Gonjal, J., A. Arevalo-Lopez, and E. Morán, *Microwave-assisted synthesis: a fast and efficient route to produce LaMO 3 (M= Al, Cr, Mn, Fe, Co) perovskite materials.* Materials Research Bulletin, 2011. **46**(2): p. 222-230.

25. Reichenbach, H.M. and P.J. McGinn, *Combinatorial solution synthesis and characterization of complex oxide catalyst powders based on the LaMO 3 system.* Applied Catalysis A: General, 2003. **244**(1): p. 101-114.

26. Skaribas, S.P., P.J. Pomonis, and A.T. Sdoukos, *Low-temperature synthesis of perovskite solids LaMO 3 (M= Ni, Co, Mn) via binuclear complexes of compartmental ligand N, N'-bis (3-carboxysalicylidene) ethylenediamine.* Journal of Materials Chemistry, 1991. **1**(5): p. 781-784.

27. Goldschmidt, V., *Skrifter Norske Videnskaps-Akad.* Oslo I, Mat-Naturvidensk Kl, 1926. **8**(2).

28. Murphy, A., *Band-gap determination from diffuse reflectance measurements of semiconductor films, and application to photoelectrochemical water-splitting.* Solar Energy Materials and Solar Cells, 2007. **91**(14): p. 1326-1337.

29. Wendlandt, W.W. and H.G. Hecht, *Reflectance spectroscopy*. Vol. 80. 1966: Interscience New York.

30. Tauc, J., *Optical properties and electronic structure of amorphous Ge and Si.* Materials Research Bulletin, 1968. **3**(1): p. 37-46.

31. Stenzel, O., *The physics of thin film optical spectra: an introduction*. Vol. 44. 2005: Springer Science & Business Media.

32. Rosencher, E. and B. Vinter, *Optoelectronics*. 2002: Cambridge University Press.

33. Davis, E. and N. Mott, *Conduction in non-crystalline systems V. Conductivity, optical absorption and photoconductivity in amorphous semiconductors.* Philosophical Magazine, 1970. **22**(179): p. 0903-0922.

34. Wasim, S. M., G. Marın, C. Rincón, P. Bocaranda, and G. Sánchez Pérez, *Urbach's tail in the absorption spectra of the ordered vacancy compound CuGa 3 Se 5.* Journal of Physics and Chemistry of Solids, 2000. **61**(5): p. 669-673.

35. Cody, G. D., T. Tiedje, B. Abeles, B. Brooks, and Y. Goldstein., *Disorder and the optical-absorption edge of hydrogenated amorphous silicon.* Physical Review Letters, 1981. **47**(20): p. 1480.

36. Sumi, H. and Y. Toyozawa, *Urbach-Martienssen rule and exciton trapped momentarily by lattice vibrations.* Journal of the Physical Society of Japan, 1971. **31**(2): p. 342-358.

37. Schreiber, M. and Y. Toyozawa, *Numerical Experiments on the Absorption Lineshape of the Exciton under Lattice Vibrations. I. The Overall Lineshape.* Journal of the Physical Society of Japan, 1982. **51**(5): p. 1528-1536.

38. Schreiber, M. and Y. Toyozawa, *Numerical experiments on the absorption lineshape of the exciton under lattice vibrations. III. The Urbach rule.* Journal of the Physical Society of Japan, 1982. **51**(5): p. 1544-1550.

39. Thouless, D.J., *Electrons in disordered systems and the theory of localization.* Physics Reports, 1974. **13**(3): p. 93-142.

40. Kubelka, P. and F. Munk, *A contribution to the optics of pigments.* Z. Tech. Phys, 1931. **12**: p. 593-599.

41. Simmons, E.L., *Diffuse reflectance spectroscopy: a comparison of the theories.* Applied Optics, 1975. **14**(6): p. 1380-1386.

42. Bott, A.W., *Electrochemistry of semiconductors.* Current Separations, 1998. **17**: p. 87-92.

43. Gomes, W. and F. Cardon, *Electron energy levels in semiconductor electrochemistry.* Progress in Surface Science, 1982. **12**(2): p. 155-215.

44. Martinez, A. M., L. G. Arriaga, A. M. Fernandez, and U. Cano, *Band edges determination of CuInS2 thin films prepared by electrodeposition.* Materials Chemistry and Physics, 2004. **88**(2-3): p. 417-420.

45. Cardon, F. and W. Gomes, *On the determination of the flat-band potential of a semiconductor in contact with a metal or an electrolyte from the Mott-Schottky plot.* Journal of Physics D: Applied Physics, 1978. **11**(4): p. L63.

46. Berzelius, J.J., *Essai sur la théorie des proportions chimiques et sur l'influence chimique de l'électricité*. 1819: Méquignon-Marvis.

47. Jensen, W.B., *Electronegativity from Avogadro to Pauling: Part 1: Origins of the Electronegativity Concept.* Journal of chemical education, 1996. **73**(1): p. 11.

48. Pauling, L. and D.M. Yost, *The additivity of the energies of normal covalent bonds.* Proceedings of the National Academy of Sciences of the United States of America, 1932. **18**(6): p. 414.

49. Pauling, L., *The Nature of the Chemical Bond*. Vol. 3. 1960: Cornell university press Ithaca, NY.

50. Masia, M., M. Probst, and R. Rey, *On the performance of molecular polarization methods. I. Water and carbon tetrachloride close to a point charge.* The Journal of chemical physics, 2004. **121**(15): p. 7362-7378.

51. Mulliken, R.S., *A new electroaffinity scale; together with data on valence states and on valence ionization potentials and electron affinities.* The Journal of Chemical Physics, 1934. **2**(11): p. 782-793.

52. Parr, Robert G., Robert A. Donnelly, Mel Levy, and William E. Palke, *Electronegativity: the density functional viewpoint.* The Journal of Chemical Physics, 1978. **68**(8): p. 3801-3807.

53. Manne, R. and T. Åberg, *Koopmans' theorem for inner-shell ionization.* Chemical Physics Letters, 1970. **7**(2): p. 282-284.

54. Nethercot Jr, A.H., *Prediction of Fermi energies and photoelectric thresholds based on electronegativity concepts.* Physical Review Letters, 1974. **33**(18): p. 1088.

55. Arima, T.-h. and Y. Tokura, *Optical Study of Electronic Structure in Perovskite-Type RM O3 (R= La, Y; M= Sc, Ti, V, Cr, Mn, Fe, Co, Ni, Cu).* Journal of the Physical Society of Japan, 1995. **64**(7): p. 2488-2501.

56. Arima, T., Y. Tokura, and J. Torrance, *Variation of optical gaps in perovskite-type 3d transition-metal oxides.* Physical Review B, 1993. **48**(23): p. 17006.

57. Park, Jaehoon, Seungoh Ryu, Moon-sup Han, and S-J. Oh, *Charge-transfer satellites in the 2p core-level photoelectron spectra of heavy-transition-metal dihalides.* Physical Review B, 1988. **37**(18): p. 10867.

58. De Haart, L., A. De Vries, and G. Blasse, *On the photoluminescence of semiconducting titanates applied in photoelectrochemical cells.* Journal of Solid State Chemistry, 1985. **59**(3): p. 291-300.

59. Tang, H., F. Levy, H. Berger, and P. E. Schmid., *Urbach tail of anatase TiO 2.* Physical Review B, 1995. **52**(11): p. 7771.

60. Dean, M.H. and U. Stimming, *The electronic properties of disordered passive films.* Corrosion Science, 1989. **29**(2): p. 199-211.

61. Dewald, J., *The charge and potential distributions at the zinc oxide electrode.* Bell System Technical Journal, 1960. **39**(3): p. 615-639.

62. De Gryse, R., W. P. Gomes, F Cardon, and J. Vennik, *On the Interpretation of Mott-Schottky Plots Determined at Semiconductor/Electrolyte Systems.* Journal of the Electrochemical Society, 1975. **122**(5): p. 711-712.

63. Mulliken, R.S., *Electronic structures of molecules XI. Electroaffinity, molecular orbitals and dipole moments.* The Journal of Chemical Physics, 1935. **3**(9): p. 573-585.

64. Bader, R.F., *Atoms in molecules*. 1990: Wiley Online Library.

65. Zhao, Jincai, Taixing Wu, Kaiqun Wu, Kyoko Oikawa, Hisao Hidaka, and Nick Serpone, *Photoassisted degradation of dye pollutants. 3. Degradation of the cationic dye rhodamine B in aqueous anionic surfactant/TiO2 dispersions under visible light irradiation: evidence for the need of substrate adsorption on TiO2 particles.* Environmental science & technology, 1998. **32**(16): p. 2394-2400.

66. Sun, Mengmeng, Yinshan Jiang, Fangfei Li, Maosheng Xia, Bing Xue, and Darui Liu, *Dye Degradation Activity and Stability of Perovskite-Type LaCoO3-x (x= 0-0.075).* Materials transactions, 2010. **51**(12): p. 2208-2214.

67. Morris, A.J., G.J. Meyer, and E. Fujita, *Molecular approaches to the photocatalytic reduction of carbon dioxide for solar fuels.* Accounts of Chemical Research, 2009. **42**(12): p. 1983-1994.

68. Xie, Shunji, Yu Wang, Qinghong Zhang, Wenqing Fan, Weiping Deng, and Ye Wang, *Photocatalytic reduction of CO 2 with H2O: significant enhancement of the activity of Pt–TiO 2 in CH 4 formation by addition of MgO.* Chemical Communications, 2013. **49**(24): p. 2451-2453.

69. Kamat, P.V., *Manipulation of charge transfer across semiconductor interface. A criterion that cannot be ignored in photocatalyst design.* The Journal of Physical Chemistry Letters, 2012. **3**(5): p. 663-672.

70. Li, K., Kimfung, Xiaoqiang An, Kyeong Hyeon Park, Majeda Khraisheh, and Junwang Tang, *A critical review of CO 2 photoconversion: catalysts and reactors.* Catalysis Today, 2014. **224**: p. 3-12.

71. Al-Ani, S. and A.A. Higazy, *Study of optical absorption edges in MgO-P2O5 glasses.* Journal of materials science, 1991. **26**(13): p. 3670-3674.

72. Al-Ani, S., C. Hogarth, and M. Ilyas, *The optical absorption edge in thin amorphous oxide films based on germania.* Journal of materials science letters, 1984. **3**(5): p. 391-394.

APPENDIX A: GENERAL INFORMATION

A.1 Absorption Coefficient Calculation

The absorption coefficient can be calculated from reflectance, transmittance and or absorbance data. Due to the dense non transparent nature of the perovskite powders, absorption coefficient was estimated from absorbance data. The baseline measurements were carried out with Spectralon SRM 99. The absorbance of glass due to the fashion of sample setup was essential so as to avoid misleading data. The absorbance spectrum of glass in shown below

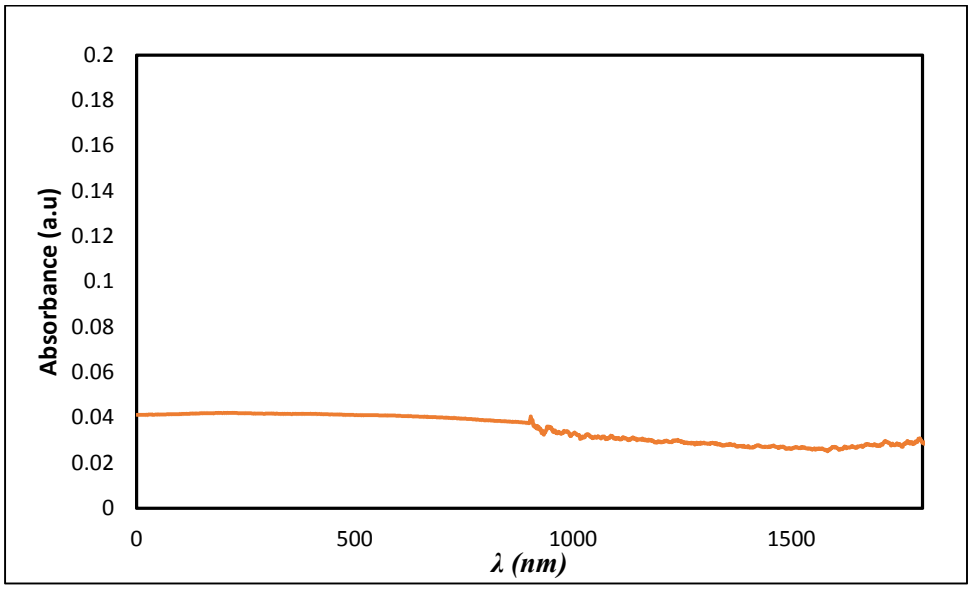

Figure A.1 Absorbance spectrum of glass microscope slide

The absorbance data is converted to the absorption coefficient of the material by using the following formula[71, 72].

$$\alpha(\lambda) = \frac{2.303\ A(\lambda)}{D} \qquad \text{(A 1.1)}$$

where α is the absorption coefficient, A is the absorbance and D is the thickness of the absorbing material.

A.2 Mott Schottky: Reference Electrode Calibration

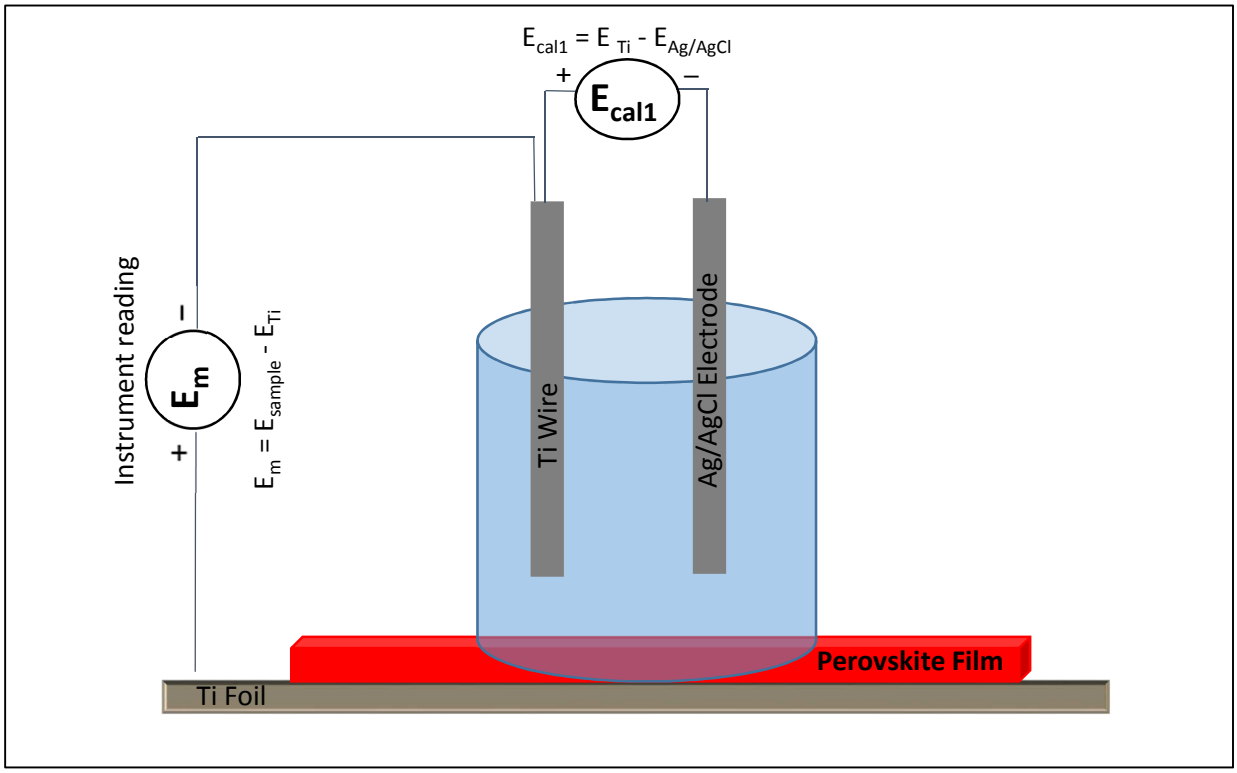

Figure A.2 Calibration of measured voltage against Sat. Calomel electrode

$$E_m = E_{sample} - E_{Ti} \qquad \text{(A 1.2)}$$

where E_m is the instrument reading, E_{sample} and E_{Ti} are the potentials of the semiconductor surface and Ti reference electrode.

$$E_{cal1} = E_{Ti} - E_{Ag/AgCl} \quad \text{(A 1.3)}$$

where $E_{Ag/AgCl}$ is the standard Silver/ Silver Chloride electrode

$$E_{cal2} = E_{Ti} - E_{SCE} \quad \text{(A 1.4)}$$

where E_{SCE} is the standard sat. Calomel electrode. Then,

$$E = E_{Ti} - E_{SCE}$$

$$= E_{sample} + E_{Ti} - E_{Ti} - E_{SCE} \text{ (Adding and subtracting } E_{Ti})$$

$$= E_{sample} + E_{Ti} - E_{Ag/AgCl} + E_{Ag/AgCl} - E_{SCE} \text{ (Adding and subtracting } E_{Ag/AgCl})$$

$$= \boldsymbol{E_m + E_{cal1} + E_{cal2}}$$

A.3 Electronegativity Calculation

Table A.1 Mulliken's electronegativity

Element	I.P (e.V)	E.A (e.V)	Mulliken's electronegativity
La	5.58	0.47	3.02
O	13.62	1.46	7.54
Fe	7.90	0.15	4.03
Mn	7.43	-1.00	3.22
Cr	6.77	0.68	3.72

Electronegativity values were calculated using the first ionization potential and first electron affinity values of the participating atoms.

Table A.2 Comparison of calculated and measured band edges for $LaCr_xFe_{1-x}O_3$

Perovskite	C.B		V.B	
	Calculated V vs NHE	**M.S** V vs NHE	**Calculated** V vs NHE	**M.S** V vs NHE
$LaFeO_3$	-0.01	-0.39	2.09	1.71
$LaCr_{0.5}Fe_{0.5}O_3$	0.05	-0.565	1.95	1.33
$LaCr_{0.75}Fe_{0.75}O_3$	-0.02	-0.87	1.92	1.07
$LaCrO_3$	-0.65	-0.90	2.55	2.30

Table A.3 Comparison of calculated and measured band edges for $LaMn_xFe_{1-x}O_3$

Perovskite	C.B		V.B	
	Calculated V vs NHE	**M.S** V vs NHE	**Calculated** V vs NHE	**M.S** V vs NHE
$LaMnO_3$	-0.05	-0.63	0.95	0.37
$LaMn_{0.75}Fe_{0.25}O_3$	0.46	-0.86	1.26	0.63
$LaMn_{0.5}Fe_{0.5}O_3$	0.62	-0.98	1.22	-0.38
$LaMn_{0.25}Fe_{0.75}O_3$	0.45	-0.63	1.50	0.42
$LaFeO_3$	-0.01	-0.39	2.09	1.71

Table A.4 Comparison of calculated and measured band edges for $LaCr_xMn_{1-x}O_3$

Perovskite	C.B		V.B	
	Calculated V vs NHE	**M.S** V vs NHE	**Calculated** V vs NHE	**M.S** V vs NHE
$LaMnO_3$	-0.05	-0.63	0.95	0.37
$LaCr_{0.25}Mn_{0.75}O_3$	0.41	-0.76	1.26	0.08
$LaCr_{0.5}Mn_{0.5}O_3$	0.42	-0.90	1.32	-0.003
$LaCr_{0.75}Mn_{0.25}O_3$	0.26	-0.94	1.46	1.25
$LaCrO_3$	-0.65	-0.90	2.55	2.30